Development of a Simulation Model of a Backhoe Excavator

A Thesis Submitted to the
College of Graduate Studies and Research
in Partial Fulfillment of the Requirements
for the Degree of Master of Science
in the Department of Mechanical Engineering

University of Saskatchewan
Saskatoon

By
Tyrell Preiss
August 2011

Permission to Use

In presenting this thesis in partial fulfillment of the requirements for a Postgraduate degree from the University of Saskatchewan, I agree that the Libraries of this University may make it freely available for inspection. I further agree that permission for copying of this thesis/dissertation in any manner, in whole or in part, for scholarly purposes may be granted by the professor or professors who supervised my thesis/dissertation work or, in their absence, by the Head of the Department or the Dean of the College in which my thesis work was done. It is understood that any copying or publication or use of this thesis/dissertation or parts thereof for financial gain shall not be allowed without my written permission. It is also understood that due recognition shall be given to me and to the University of Saskatchewan in any scholarly use which may be made of any material in my thesis/dissertation.

Requests for permission to copy or to make other uses of materials in this thesis/dissertation in whole or part should be addressed to:

Head of the Department of Mechanical Engineering
University of Saskatchewan
57 Campus Drive
Saskatoon, Saskatchewan, S7N 5A9
Canada

Abstract

The recent pattern of record-high fuel prices has motivated a trend towards reducing the fuel consumption of today's equipment, while still maintaining the capability and performance offered in previous models. One opportunity to improve fuel economy that has been relatively unexplored in the literature is to understand the effect an operator has on a machine's efficiency for a given task. Understanding the relationship between an operator's skill level and the machine's response poses new opportunities to improve the fuel consumption of a given piece of equipment.

The focus of this thesis is to lay the framework for future studies to investigate the operator's effect on a machine. As a first step in this project, a simulation model of a John Deere 410G backhoe is developed to be used as a future tool in incorporating and reproducing the effects of various operator skill levels and techniques on a machine. The simulation model contains three main sub-models, namely: the *kinematics* to recreate the motion of the system, the *kinetics* to predict the loads experienced by the system, and the *hydraulics* to drive the motion of the system. The simulation model was developed in the *MATLAB Simulink* environment, and allowed for both computer coding and object-oriented modeling to be used in a single package.

The results from the simulation model were examined and compared to data collected from the John Deere 410G backhoe. The comparison shows that the simulation and experimental data correlate very well during steady-state actuator extensions, but future work is required to improve the simulation dynamics, and steady-state results predicted as the hydraulic actuators travel in the retraction direction.

Acknowledgements

The author wishes to express his gratitude to his supervisors, Dr. Richard Burton, Dr. Jeff Dobchuk, and Dr. Greg Schoenau for their guidance, support, and encouragement during the preparation of this thesis. The technical assistance provided by Dr. Allan Dolovich and Mr. Doug Bitner is also gratefully acknowledged and appreciated.

The author acknowledges the financial assistance received from the Department of Mechanical Engineering at the University of Saskatchewan in the form of a departmental scholarship, as well as additional assistance provided by Dr. Richard Burton.

Finally, the author wishes to extend a heartfelt thank you to his friends and family, for their encouragement, support, and understanding during the preparation of this thesis.

Table of Contents

List of Tables

List of Figures

Nomenclature

$\overrightarrow{AB}$	Vector between *A* and *B*	
$\left\|\overrightarrow{AB}\right\|$	Magnitude of vector $\overrightarrow{AB}$	
AB_n	The projection of $\overrightarrow{AB}$ onto axis *n*	
$A_{B,R}$	Cross-sectional area of a hydraulic cylinder	[m^2]
A_n	Force acting at point *A* along axis *n*	[N]
$\vec{A}_x$	Acceleration of point *x*	[m/s^2]
c_x	Hydraulic capacitance	[MPa/ m^3]
$\frac{d^2 r_{B/A}}{dt^2}$	Sliding acceleration of linkage between *A* and *B*	[m/s^2]
$\frac{dr_{B/A}}{dt}$	Sliding velocity of a linkage	[m/s]
D_x	Diameter of line *x*	[m]
F_x	Force at location *x*	[N]
f_x	Net position change around a position loop	[m]
I_G	Mass moment of inertia taken about point *G*	[kg·m^2]
$\hat{\imath}$	Unit vector along the *x* axis	
$\hat{\jmath}$	Unit vector along the *y* axis	
$\hat{k}$	Unit vector along the *z* axis	
L_{AB}	Magnitude of the position vector between *A* and *B*	[m]
$\vec{M}_G$	Moment about point *G*	[N·m]
m_x	Mass of body *x*	[kg]
P_x	Pressure at point *x*	[MPa]
ΔP_x	Pressure differential between two points at *x*	[MPa]
Q_x	Hydraulic fluid flow rate at location *x*	[m^3/s]
ΔQ_x	Flow differential at location *x*	[m^3/s]
$\vec{r}_{B/A}$	Position vector from *A* to *B*	[m]
RA_x	Lumped hydraulic resistance of an orifice	[(m^3/s)/$(MPa)^{1/2}$]
R_{CV}	Check valve hydraulic resistance	[(m^3/s)/$(MPa)^{1/2}$]
t	Thickness	[m]

$\hat{u}_{B/A}$	Unit vector in the direction from *A* to *B*	
$\vec{V}_x$	Velocity of point *x*	[m/s]
v_x	Volume at location *x*	[m^3]
$\ddot{x}$	Actuator sliding acceleration	[m/s^2]
$\dot{x}$	Actuator sliding velocity	[m/s]
x_{spool}	Control valve spool displacement	[m]
$\vec{\alpha}_{AB}$	Angular acceleration of the linkage between *A* and *B*	[rad/s^2]
α_x	Fixed geometry angles on the backhoe workgroup	[^{o}]
β	Bulk modulus of hydraulic fluid	[MPa]
$\frac{d\theta_x}{dt}$	Rate change of angle θ_x	[rad/s]
θ_x	Angle measured between a linkage and the ground plane	[^{o}]
μ	Viscosity of hydraulic fluid	[m^2/s]
ρ	Material density	[kg/m^3]
ϕ	Swing angle of the backhoe workgroup	[^{o}]
$\vec{\omega}_{AB}$	Rotational velocity of the linkage between *A* and *B*	[rad/s]

Abbreviations

FBD	Free body diagram
JD	John Deere
LS	Load-sensing
PBG	Power bond graph

Chapter 1: Introduction and Objectives

1.1 Project Background and Motivation

The worldwide trend of reducing emissions and fuel consumption, coupled with rising oil prices is leading to new equipment that not only offers increased capabilities and more features than previous models, but does so more efficiently. Mobile hydraulic systems are selected for their reliability, controllability, and high power density. These advantages often come at the expense of relatively low efficiencies under certain circumstances.

The fluid power community is aware that in order to maintain the demand and application of mobile hydraulic equipment, these systems must be more efficient. There exists an established and expanding body of research aimed at improving the energy efficiency of hydraulic systems. This encompasses many different directions, including improving or redesigning individual components, designing circuits to minimize losses, using computer simulations to test and improve systems, or introducing new innovations to the fluid power community, allowing designers to apply new components to existing designs. The result is more efficient hydraulic systems that do not compromise performance or capability.

Prior to beginning this project, an extensive literature review was completed to examine the state of research with respect to energy efficiency of hydraulic systems. This initial literature review is included in Appendix A, and a project-relevant literature review will be included in the following section.

While there is no question that hydraulic systems are becoming more efficient, there are still further improvements that can be made. When improving the efficiency of hydraulic systems, the focus has been primarily on the systems themselves; however, little or no consideration has been given to the manner in which the equipment is used. It is expected that no matter how efficient a circuit is or its components may be, the operator will affect how much fuel is consumed in completing a certain task.

As an example, consider the John Deere (JD) 410G backhoe-loader shown in Figure 1.1. Focusing on the backhoe portion of the machine, which is located behind the cab, the operator is responsible for controlling the inputs to each of the four hydraulically actuated functions by means of control levers. Each lever is directly coupled to a directional control valve, which is used to control the hydraulic fluid delivered to each of the four functions. Movement of the four hydraulic functions allows the operator to control the location and orientation of the bucket, which is the objective for a given task. The operator controls the bucket location primarily through visual feedback.

Figure 1.1 John Deere 410G Backhoe-loader

It is expected that various operators of different skill and experience levels will exhibit different methods of control lever inputs, and will react differently to visual feedback. These differences in inputs between operators will affect the fuel consumption of the machine in completing a certain task. It is feasible to hypothesize that a relatively inexperienced operator will require more time and fuel to complete the same task as a more skilled operator. If there is a relationship between operator and machine behavior, then understanding the *operator effect* will prove beneficial in improving the way hydraulic systems are operated in the future, further improving overall efficiencies and productivity.

The continual increase in computing power and improvements in available software has led to a relative ease and willingness of researchers to use computer simulations in modeling hydraulic

systems. Simulations are advantageous when used in the design process, as they can be used to reduce the need for early prototypes, and can provide designers with insight towards machine performance. Simulations also allow a wide variety of conditions to be modeled for a given machine, which in some cases cannot be easily accomplished by means of physical testing. Accurate simulations can also provide details of the phenomena occurring in components that often cannot be easily measured, and are well suited to determining the energy inputs and outputs for a system, which can be used to determine efficiencies.

1.2 Literature Review

Prior to development of the project objectives, an initial literature review was conducted to understand the state of research focusing on the energy efficiency of hydraulic systems, and the findings of the extensive review are included in Appendix A. To follow is a review of the literature dealing with quantifying the operator, and simulation and modeling of mobile hydraulic equipment; namely backhoes and excavators. The sources consist of a subset of relevant papers selected from the reference list in Appendix A, along with a number of additional sources.

For the most part, the literature obtained that focuses on simulating either a backhoe-loader or excavator was presented in a general format, often leaving out many details that would not allow a reader to recreate the presented work. Zimmerman has developed a simulation model of a compact excavator for the purpose of investigating where the supplied power from the engine is consumed [1]. The dynamics of the system are modeled using SimMechanics and manufacturer-supplied CAD drawings; unfortunately, details pertaining to this method are not provided. Little discussion is provided about the hydraulic model as well. Zimmerman has divided the energy consumption of the compact excavator into three main areas, namely: actuator work, control valve losses, and pump losses. The energy losses across the control valves are found to compose 35% of the machine's total energy consumption, and it is concluded that reducing these losses is a simple and straightforward approach to saving fuel costs.

Andruch and Lumkes have presented a solution to the problem of energy losses due to control valve losses, as presented by Zimmerman [2]. They have suggested replacing the existing system's hydraulics with a network of lines and on/off valves that can be used to configure flow paths in a way to minimize throttling. Simulation results suggest system energy savings can be as high as 33% over existing designs. The cost implications of adding multiple on/off valves, and complexity of controlling multiple possible flow paths are not discussed in detail.

Engja and Pederson define a simulation as, "being an 'experiment performed on a model' for the purpose either of understanding the behavior of a system, or of evaluating various strategies for the operation of a system" [3]. They go on to discuss the shortcomings of current modeling packages, in that they often do not allow the user to see what assumptions or mathematics were used in creation of the model and its components. Instead, they favor the graphical method of Power Bond Graphs (PBG) to understand the power flows in a physical system. Herman et al. describes PBG's as, "a structured language, which describes simultaneously the energetic exchanges between basic elements of the system as well as the origin of these exchanges by means of causality of relations" [4]. If done correctly, describing a system using PBG's allows the causality of the describing equations to be quickly and systematically understood.

Novak and Larson have modeled a backhoe excavator with a prescribed motion cycle [5]. The goal is to determine the engine power requirements. In this model, the actuator positions, velocities, and accelerations are used to determine the resulting force on the three actuator rods. From this, the required pressure is determined, assuming that the tank side of the actuator is at zero pressure. No discussion is offered on why this assumption is made. They also assume the linear accelerations to be negligible, allowing them to use more simple static force equations.

Koivo has set out to automate excavators, and has provided a kinematic model for an excavator in his work [6]. He has placed coordinate axes on each point of revolution in the system, with each point being related back to a global coordinate axis. Koivo's model has included both forward and backward (inverse) kinematic equations, which allows the model to use either the lengths and rotation of the actuators to be used to find the bucket location (using the forward equations), or to input the desired location of the bucket and let the simulation determine how to

get the system oriented (using the backward equations). It appears that similar to Novak and Larson, Koivo has not directly used the linear accelerations of the modeled points, although no mention is made of this.

Lance and Prescott provide an in-depth discussion on the role of simulations and computer modeling in the design process, in light of the increased capability of computer processing [7]. They have developed a simple model of a backhoe linkage, powered by a fixed-displacement pump, and having a fixed swing angle. Lance and Prescott discuss that the, "masses and inertias of the dump and guide bodies are so small compared to the other bodies that their effect on the system is negligible." In this work, they have created a simple model and shown its functionality. Mention is made that the next step is to model a real system and do a comparison of the two. They also make mention of using realistic human inputs, but only go so far as to say that the more realistic the inputs are, the better the simulation results should be.

1.3 Project Objectives

Identifying the operator as a potential energy saver for mobile hydraulic equipment, and considering the lack of research performed on this subject leads to the *global* project objective: To quantify the effect operators have on overall machine productivity, and to create a simulation tool capable of comparing this effect across different control and hydraulic system architectures. This objective can be further divided into two components: (1) Architecture simulation, and (2) Operator quantification and implementation.

The objective of this thesis will focus on the first component of the *global* project objective, focusing on the simulation and modeling of a mobile hydraulic system. The objective of this research can then be defined as follows: To develop a computer model capable of simulating the backhoe section of the JD 410G, to be used to realize the global project objective. The JD 410G backhoe-loader has been selected as the focus of this study as it is readily available to be used, and is a common piece of mobile hydraulic equipment found on many construction sites.

1.4 Outline and Structure of Thesis

Chapter 2 will introduce the JD 410G in detail, discussing the functionality of the hydraulics, and how the system operates. In addition, a simplified schematic will be introduced, and a simulation approach will be presented and discussed.

Chapter 3 will focus on the kinematic modeling of the backhoe; a coordinate system will be defined, and the equations needed to represent the position, velocity, and accelerations of the system will be presented. The kinematic model is then verified using experimental measurements taken from the physical system.

Chapter 4 will discuss the kinetic model of the system. The process of taking the results from Chapter 3 and using them to determine the forces acting on each of the hydraulic cylinders is discussed. A qualitative verification is presented, as the instrumentation needed to do a dynamic quantitative verification was not available.

Chapter 5 uses the results from the previous two chapters in conjunction with a Power Bond Graph approach to develop a hydraulic model to drive the motion of the system, given control valve inputs.

Chapter 6 provides a comparison and discussion between data collected from the JD 410G backhoe-loader and the outputs of the simulation model.

The final chapter, Chapter 7, will be used to summarize the results, provide conclusions, and recommend future work for the project.

Chapter 2: System Description and Simulation Outline

2.1 The John Deere 410G Backhoe-Loader

Backhoe-loaders are versatile machines that are popular among construction sites. They consist of three main parts: the tractor, loader, and backhoe, shown in Figure 2.1. The tractor contains the power plant, transportation means, and operator cab. It houses the internal combustion engine that not only drives the wheels, but also powers the electronics and hydraulic pump that is used for the backhoe and front-end loader functions. The front-end loader consists of two lift arms and a bucket that are each manipulated by hydraulic actuators. One set of boom actuators are used to control the height of the loader, and the other(s) is used to adjust the bucket angle. The rear-mounted backhoe workgroup (the system of interest in this study) consists of three main parts: the boom, stick, and bucket (see Figure 2.2). Hydraulic actuators control each of these parts, and the operator of the machine must manipulate all three functions together in order to achieve a desired bucket location and orientation. The backhoe can also swing about the cab of the tractor, allowing a wide range of possible bucket positions from a fixed tractor location.

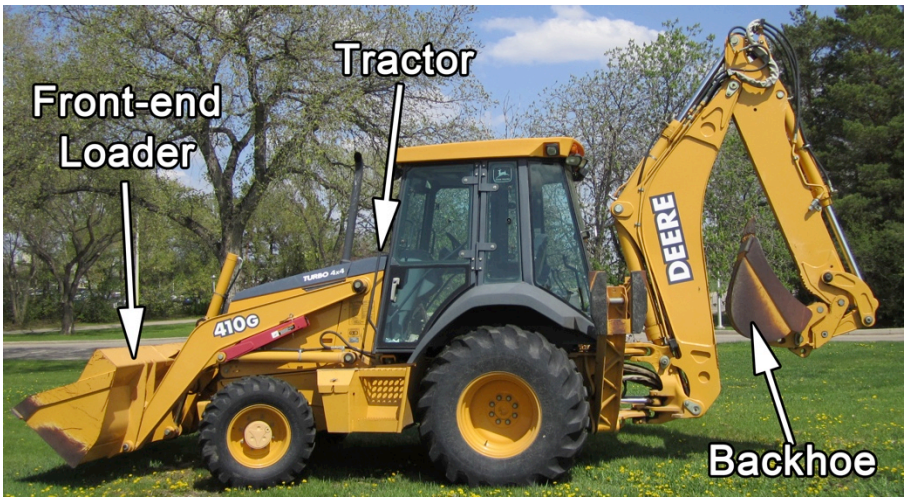

Figure 2.1 The John Deere 410G Backhoe Loader

As mentioned, this chapter will focus on the modeling of the backhoe workgroup of the JD 410G, as this particular machine was available for testing. The following section contains a

description of the backhoe and the hydraulics that control the system. Figure 2.2 depicts the backhoe section of the JD 410G, and the main components have been labeled.

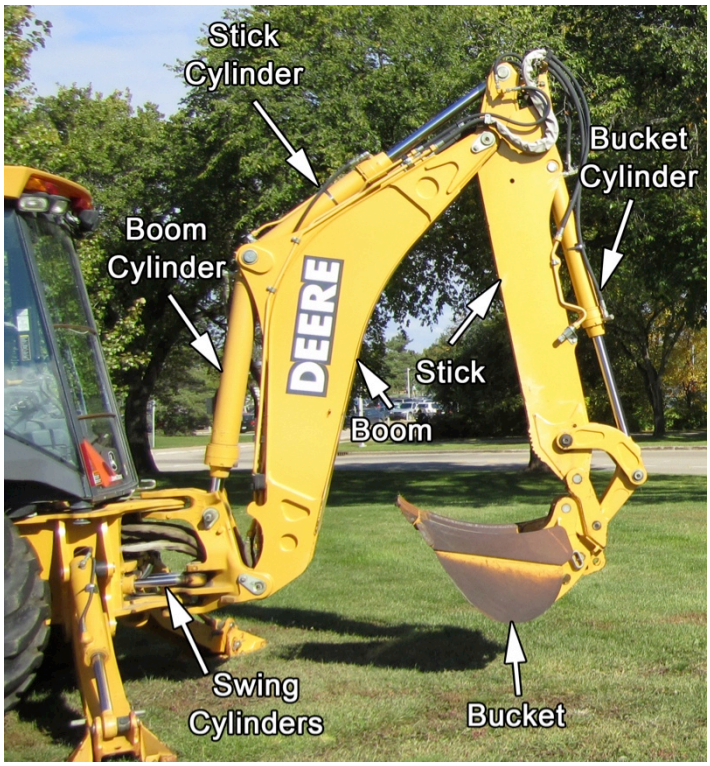

Figure 2.2 John Deere 410G Backhoe Workgroup

The largest component of the workgroup is the boom, which links the backhoe to the chassis of the tractor. The boom cylinder is used to lower and raise the entire workgroup. The stick is connected to the boom, and is controlled by the stick cylinder, which moves both the stick and bucket. There is also a hydraulic cylinder contained within the stick that allows the operator to extend the length of the stick. This feature is not considered in the modeling of this system, and thus the stick can be treated as having a fixed length. Finally, the bucket is connected to the stick by means of the bucket cylinder and two guide pieces. There are two swing cylinders that work together to rotate the workgroup about a vertical axis, allowing the operator a wide range of reaches. The bucket is the object of control by the operator; all motions with the boom, stick, swing, and bucket cylinders are to achieve the desired bucket location and orientation for a given task.

Two levers located within the cab of the tractor control the four hydraulic cylinders. The levers are coupled directly to the spools of the directional control valves by a mechanical linkage. Figure 2.3 shows the control levers for the backhoe. As there are two levers controlling four functions, each lever controls two functions. The lever on the operator's left controls the swing circuit by movement left and right, and the boom is actuated by a forward and backward motion. The lever on the operator's right controls the bucket cylinder by moving left and right, and moving the lever in a forward and backward motion controls the stick cylinder.

Figure 2.3 Operator Controls for the JD 410G Backhoe

2.2 Backhoe Hydraulics

To follow is a brief discussion of the four hydraulic circuits to be modeled for each of the main functions of the JD 410G backhoe (although, as will be discussed in Chapter 4, the swing function will not be included in the simulation model). The four functions, corresponding to the actuator/linkage combination shown in Figure 2.2 are the boom, stick, bucket, and swing. It will be observed that the hydraulics of the four functions each appear to be very similar in design, although there are subtle differences in each circuit that will be discussed.

The following hydraulic diagrams have been oriented to provide the reader with a clear image of each function; the load sensing components and pump are not pictured, but will be discussed. In

addition, several relief valves etc. have been excluded because they are used only in the extreme pressure conditions.

2.2.1 Load Sensing Hydraulics

The JD 410G uses a pressure compensated load-sensing (LS) hydraulic system. LS systems are popular in designs that use multiple functions driven by a single pump. The basic principle is that the highest load encountered within the circuit controls the operating pressure of the variable displacement pressure compensated pump. This ensures the pump is able to supply fluid at a higher pressure than is required by all loads operating within the system.

This is realized by each control valve function on the JD 410G having a port that is used to sense the pressure of the circuit load. Shuttle valves are used to compare two sensed pressures to each other, with the highest pressure being passed through the valve to be compared to the remaining sensed pressures in the system. After all the load pressures have been compared, the highest pressure is fed to both the pump (to set its displacement), and to each function's compensator (pressure compensated flow control valve) to control the flow being delivered to the loads. The end result is a system that sets the pump operating point to match the highest load encountered, while still allowing the lower-pressure loads to function independently of the pump setting. In most cases, load-sensing systems are relatively efficient when compared to other methods of circuit design.

2.2.2 The Swing Function

The swing function allows the operator to move the backhoe linkage left and right about a vertical kingpin joining the backhoe to the tractor chassis. This allows the operator of the machine access to a wide range of locations for the backhoe workgroup, which is useful for various tasks. Figure 2.4 shows a simplified hydraulic circuit for the swing function.

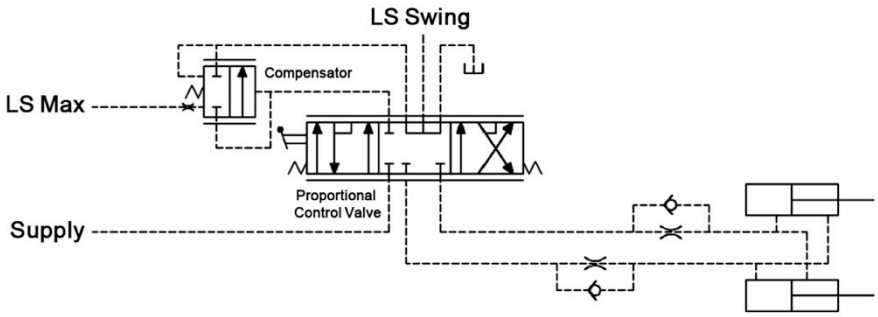

Figure 2.4 Simplified Swing Function Hydraulic Circuit

The operator controls the position of the control valve to create either a clockwise or counterclockwise rotation of the workgroup about the kingpin. With reference to Figure 2.4, when the control valve (labeled as the proportional control valve) is moved away from its center position, fluid enters the circuit from the 'Supply' line and passes through the compensator. The compensator ensures that flow entering the circuit is not affected by changes in the supply pressure. After passing through the compensator, the fluid is then routed back through the control valve, and the pressurized fluid is delivered to the desired location, which results in rotation of the workgroup by means of two coupled actuators that operate in such a way that one actuator extends at the same speed that the other retracts, as the two cylinders are coupled together by a rigid linkage. The fluid that exits the actuators then passes through the control valve again and is routed to the reservoir. When the valve is moved away from the center position, the pressure sensed by the line labeled 'LS Swing' is the highest supplied working pressure for the swing function, which is then compared to the sensed pressures from any other functions and used to set the pump displacement.

2.2.3 The Boom Function

The boom is the largest linkage in the backhoe workgroup, and fittingly contains the largest hydraulic cylinder. The boom function is used to raise and lower the entire workgroup, pivoting about a horizontal pin joining the boom to the tractor. Figure 2.5 shows a simplified schematic of the boom circuit hydraulics.

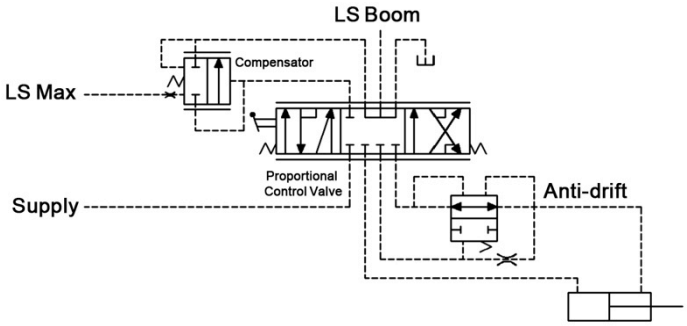

Figure 2.5 Simplified Boom Function Hydraulics

The operator controls the position of the control valve to either extend or retract the boom cylinder, raising or lowering the workgroup. When the control valve is moved away from its center position, fluid enters the circuit from the 'Supply' line and passes through the compensator. The compensator ensures that flow entering the circuit is not affected by changes in the supply pressure. After passing through the compensator, the fluid is then routed back through the control valve, and the pressurized fluid is delivered to the desired location, which is either to the blank side of the boom cylinder causing an extension, or to the rod side of the cylinder causing it to retract. The fluid that exits the actuator then passes back through the control valve and is sent to the reservoir. When the valve is moved away from the center position, the pressure sensed by the line labeled 'LS Boom' is the highest supplied working pressure for the swing function, which is then compared to the sensed pressures from any other functions and used to set the pump displacement. When the valve is in the center position, the 'Anti-drift' feature ensures that the boom cylinder does not have any unwanted movement.

2.2.4 The Stick Function

Moving along the workgroup from the boom, the next linkage is the stick, also referred to as the crowd or dipper. The stick pivots about its connection point at the end of the boom, and is used to control the reach and height of the bucket when being used in conjunction with the boom. Figure 2.6 shows a simplified schematic of the stick function. Since its operation is identical to the boom function, a detailed description is not presented here.

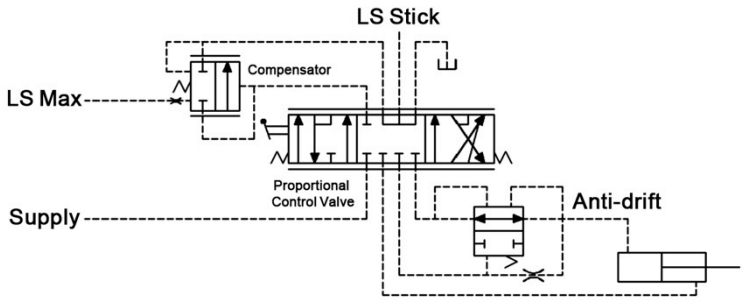

Figure 2.6 Simplified Stick Function Hydraulics

2.2.5 The Bucket Function

The final function in the workgroup controls the location of the bucket. The bucket is the focus of the operator's control inputs; all motions are made with the intent of orienting the bucket to a certain location to perform a given task. The bucket cylinder allows the bucket to travel through a large range of angular orientations, which is necessary when performing a dig/dump task as an example – the bucket must be able to transport material and dump it within the confines of its cylinder's stroke. Figure 2.7 shows a simplified hydraulic circuit of the bucket function.

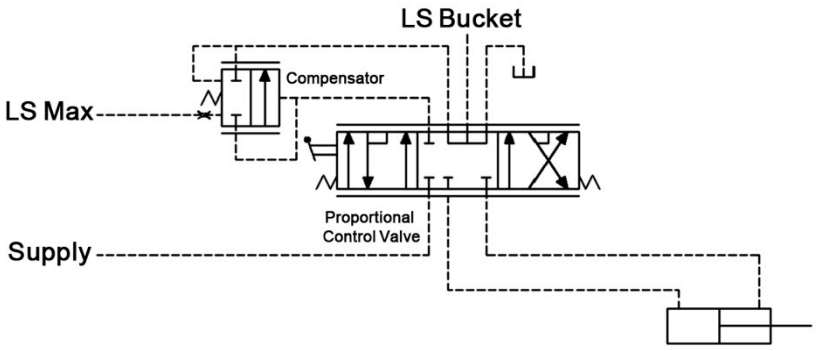

Figure 2.7 Simplified Bucket Function Hydraulics

The operator controls the position of the control valve to either extend or retract the bucket cylinder, causing the bucket to pivot about the end of the stick, with its motion being controlled by the guide linkages that can be seen in Figure 2.2. Since the operation is similar to the other functions, a detailed description is not presented.

2.2.6 Simulation Outline

The objective of this thesis is to develop a simulation capable of recreating the behavior of the JD 410G backhoe loader. An accurate and complete model of the system requires a number of smaller models to be integrated to function together. Figure 2.8 depicts a basic block diagram to be used as a basis in modeling the system.

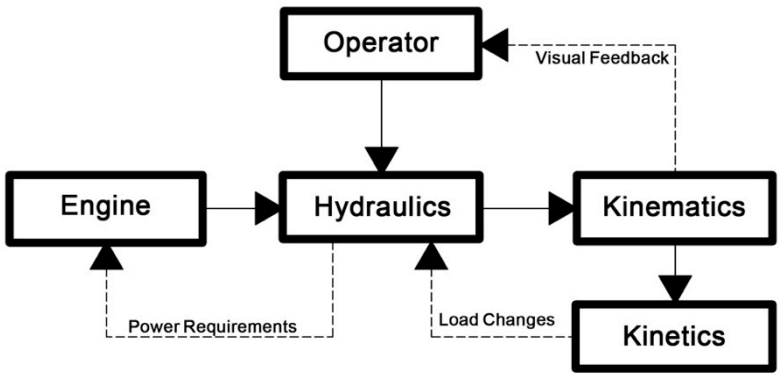

Figure 2.8 Block Diagram of the Backhoe

From the cab of the tractor, the operator directly controls the input signals to the hydraulic system by means of the two control levers, shown in Figure 2.3. The movement of the control levers causes the control valves of the four circuits to allow hydraulic fluid to pass through, causing the hydraulic cylinders to extend or retract. The movement of the hydraulic cylinders will cause the workgroup to move, and the kinematic sub model relates the motion of the hydraulic cylinders to the motion and orientation of all points of the backhoe system. The motion of the linkages, and orientation of the workgroup will cause the load on each hydraulic cylinder to change. These changes in load will affect the operating pressures of the hydraulic circuits, and this can been seen as the feedback from the kinetics into the hydraulics. These load requirements on the hydraulics must be satisfied by the engine, which must supply power to the variable displacement pump. Lastly, the operator directly observes the motion of the workgroup, and adjustments to the control inputs are made based on these observations (this feedback line could also include sound and feel as potential feedbacks to the operator).

This general explanation of how the backhoe is operated is the basis of the modeling of the system. The three sub-models to be focused on in this thesis will be the kinematics, kinetics and hydraulics. They will be discussed in Chapters 3, 4, and 5, respectively.

Chapter 3: Kinematic Modeling

3.1 Modeling Objectives

The kinematics is the first part of the JD 410G backhoe to be modeled. The objective of this modeling is to develop a set of equations to fully describe the motion of the backhoe workgroup. The inputs to the kinematic model are the motion of the four input functions, namely: the boom, stick, bucket, and swing. Each actuator will provide three inputs to be used in the simulation, in the form of position, velocity, and acceleration. As an example, consider Figure 3.1. The simple system consists of a single actuator being used to move a boom linkage. Both the actuator and body are connected to the ground and each other by pinned connections. Figure 3.1 shows two orientations of the system, controlled by the length of the boom cylinder, represented by the linkage joining points B and C. In order to move the system from *Position 1* to *Position 2*, the operator of the system uses control levers to adjust the length and speed of the boom cylinder. The length and speed of the boom cylinder are determined by the hydraulic system, and are treated as an input to the kinematic model.

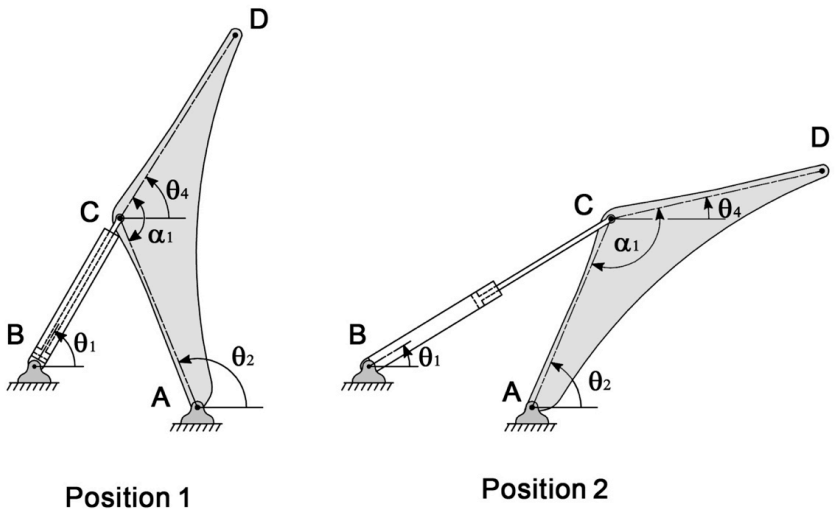

Figure 3.1 Simplified Boom Function

Consider the system in Figure 3.1 as it travels from *Position 1* to *Position 2*. Due to the pinned connections, the boom cylinder will have a rotation about point B, while the boom linkage will

rotate about point A, and both will experience different rates of rotation; θ_1 and θ_2 will not have the same rotational velocities and accelerations. As the system is moved, points C and D will experience different velocities and accelerations, as they are increasingly further from the pivot point A, which remains stationary; however, angles θ_2 and θ_4 will have the same angular velocity and acceleration, as they are contained on the same body. The kinematic model output will be the location, velocity, and acceleration of all modeling points, as well as the magnitude, velocity, and acceleration of all angles used to represent the system.

For a given input of the four main cylinder lengths, velocities, and accelerations (as determined from the hydraulic model), the goal of the kinematic modeling is to determine the location, orientation, velocity, and acceleration of all points and angles used to represent the system. To follow is a description of the development of the general equations used to model the motion of the backhoe workgroup.

3.2 System Coordinates and Layout

3.2.1 Coordinate Description

The coordinate system used in modeling the kinematics of the JD 410G backhoe is shown in Figure 3.2. The Cartesian coordinate system uses two angles, θ and ϕ, and the distance between two points (labeled 'A' and 'B' in Figure 3.2) to represent the magnitude and orientation of any vector in space.

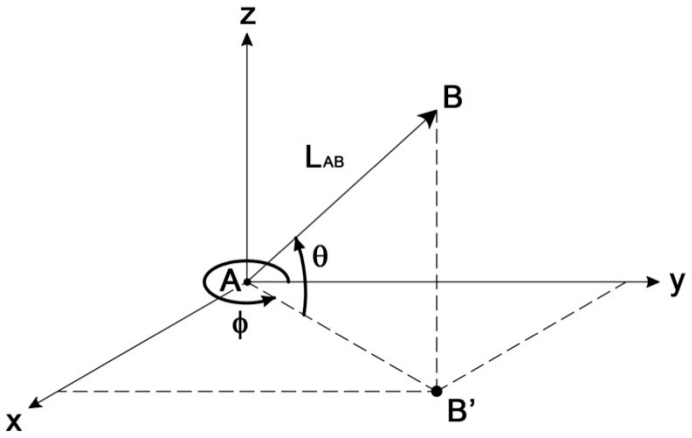

Figure 3.2 Cartesian Coordinate System Selected for Modeling

The angle, ϕ, is used to describe the swing angle of the vector, measured in the counterclockwise direction from the positive y-axis (in the x-y plane). As all the components of the backhoe workgroup are contained in a single plane (i.e., the ABB' plane) that is rotated by the swing function, the swing angle, ϕ, will be the same for all vectors modeled in the system. The angle θ is measured counterclockwise from the projection AB' of the link, to the link itself. For a given linkage joining two points, for example, points A and B, the magnitude of the vector is defined as L_{AB}, where the first subscript denotes the starting point of the vector, and the second denotes the end point.

Knowing the magnitude and orientation of a given linkage allows this information to be written into components projected onto each axis. The vector is then represented using Cartesian vector notation, such that

$$\overrightarrow{AB} = ABx\,\hat{\imath} + ABy\,\hat{\jmath} + ABz\,\hat{k}, \qquad [3.1]$$

where:

$\overrightarrow{AB}$ = the vector joining points A and B,

ABn = the projection of $\overrightarrow{AB}$ along the n-axis, and

$\hat{\imath}, \hat{\jmath}, and\ \hat{k}$ = the unit vectors along the x, y, and z axes, respectively.

Using the vector $\overrightarrow{AB}$ from Figure 3.2 as a generalized example, the Cartesian vector notation is written as

$$\overrightarrow{AB} = -L_{AB}cos\theta sin\phi\,\hat{\imath} + L_{AB}cos\theta cos\phi\,\hat{\jmath} + L_{AB}sin\theta\,\hat{k}. \qquad [3.2]$$

The Cartesian vector notation can be simplified by separating the magnitude and direction components. The magnitude of $\overrightarrow{AB}$ is defined as

$$|\overrightarrow{AB}| = L_{AB}, \qquad [3.3]$$

while the direction component is represented using a unit vector notation, which has a magnitude of unity by definition. The unit vector from A to B is represented as

$$\hat{u}_{B/A} = -cos\theta sin\phi\,\hat{\imath} + cos\theta cos\phi\,\hat{\jmath} + sin\theta\,\hat{k}. \qquad [3.4]$$

The convention of using the unit vector and magnitude representation of a vector will be used in the development of the kinematic relationships for the backhoe workgroup.

3.2.2 Backhoe Kinematic Modeling Points and Angles

The JD 410G backhoe consists of 11 pinned connections that have been selected as the modeling points for the system. The points are labeled using an alphabetic notation, and are shown in Figure 3.3. Based on these points, the linkages that will be used to model the kinematics can be described by representation of a vector between two points, as defined in the previous section.

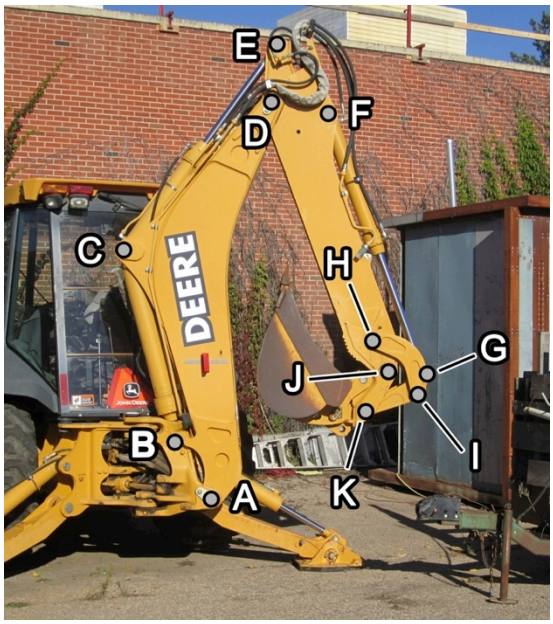

Figure 3.3 Backhoe Modeling Points

It should also be mentioned that the orientation of the backhoe linkages shown in Figure 3.3 will be referred to throughout this thesis as the *home position* (with the exception of the swing angle, which will be oriented at $\phi = 270°$). The *home position* will serve as the starting point for all simulations. While the simulation can be started from any orientation, doing so will require additional initialization calculations of angles, lengths, forces, and pressures that will not be considered in this thesis. In the home position, the boom cylinder is fully retracted, while the stick and bucket cylinders are fully extended. This position is easy to recreate on the backhoe, and is also the transport position, and has been selected for these reasons.

To determine the angular orientation of the workgroup in the home position, the distance between each of the points in Figure 3.3 was measured and used to create a scale CAD representation of the workgroup. The only fixed angle present in the system is the angle made

between $\overrightarrow{AB}$ and its projection on to the ground plane, which will be defined as θ_1. In order to draw the system properly, this angle was measured to be $\theta_1 = 121°$.

Figure 3.4 shows the CAD drawing of the model to be used to determine the initial angular orientation of the system. Using the same modeling points as shown in Figure 3.3, the lines connecting all of these points represent the linkages that will be used in the kinematic model. The fixed-length linkages are joined using a solid line, while the variable-length actuators are connected using a dashed line. The angles measured between the ground-plane and the linkages (θ) are also defined, and it can be observed there are 16 of these angles. There are also eight α-angles shown in Figure 3.4. These are fixed angles measured from the CAD drawing that are used in determining relationships between a number of θ angles in the system. The measured lengths from the JD 410G and the corresponding angles measured from the CAD drawing are included in Table 3.1. Figure 3.4 is viewed in a plane perpendicular to the swing angle, ϕ, of the system.

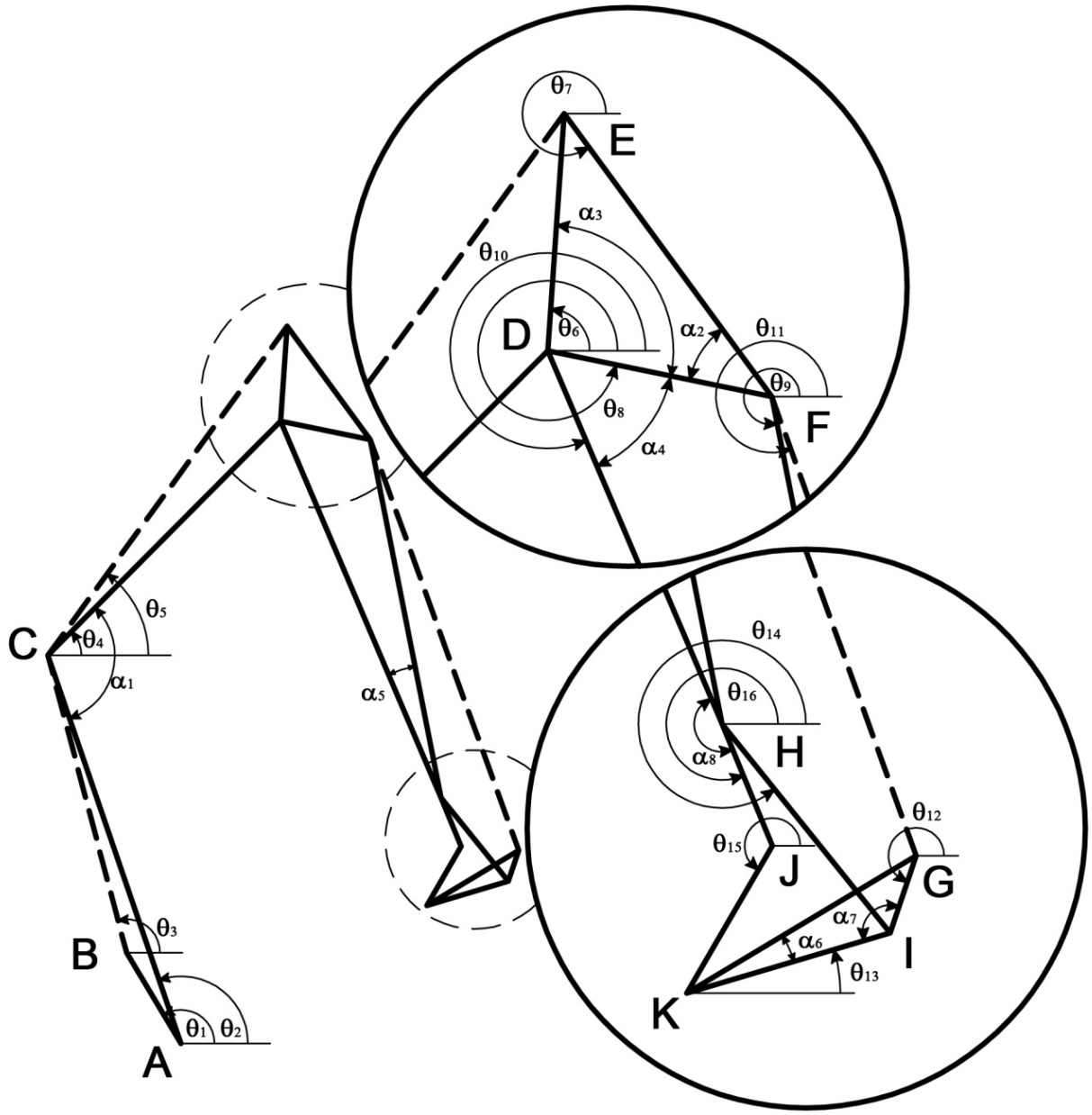

Figure 3.4 CAD Representation of the Backhoe Workgroup

Table 3.1 Lengths and Angles used to Model the JD 410G Backhoe

Linkage	Measured Length
	(mm)
L_{AB}	473
L_{AC}	1836
L_{AD}	2820
L_{BC}	1377*
L_{CD}	1478
L_{CE}	1821*
L_{DE}	425
L_{DF}	410
L_{DH}	1832
L_{DJ}	2068
L_{EF}	629
L_{FG}	1955*
L_{FH}	1634
L_{FJ}	1866
L_{GI}	139
L_{GK}	479
L_{HI}	480
L_{HJ}	238
L_{HK}	486
L_{IK}	380
L_{JK}	305
L_{JG}	257
* Denotes actuator length in the home position	

Angle**	Measured Value
	(^{o})
θ_1	121.00
θ_2	108.94
θ_3	104.82
θ_4	45.15
θ_5	53.95
θ_6	86.05
θ_7	306.27
θ_8	348.39
θ_9	281.18
θ_{10}	293.08
θ_{11}	289.88
θ_{12}	210.92
θ_{13}	16.50
θ_{14}	308.87
θ_{15}	239.80
θ_{16}	292.50
*** All above angles have been measured from the home position*	

Fixed Angle	Measured Value
	(^{o})
α_1	116.21
α_2	42.12
α_3	97.66
α_4	55.31
α_5	11.89
α_6	14.41
α_7	125.14
α_8	0.58

3.3 General Kinematic Solutions

The kinematic solution presented in this thesis differs from the traditional methodology and approach presented in many popular dynamics textbooks; rather, the approach used in this thesis is based on a method of relative positions, velocities, and accelerations that is presented to students at the University of Saskatchewan. The author would like to acknowledge Dr. Allan Dolovich from the Department of Mechanical Engineering at the University of Saskatchewan for his contribution to and development of the methods presented in this chapter. The following sections are presented to the reader with the objective of being clear and concise. As such, the completed, detailed solutions used in modeling are presented in Appendix B, and the solutions presented in the body of the thesis will be generalized.

The basic functionality of the kinematic model is summarized in Figure 3.5, showing a flowchart of how the information will travel through the model. The first step in the kinematic modeling is to read in the new variables to be used in future calculations. At the first time step, these values will be the initialized values determined from the CAD drawing discussed previously. The next step is to do a velocity analysis to determine the linear velocities of all points, and the angular velocities of each of the θ-angles. The last step is to do an acceleration analysis based on the velocity results, yielding the linear and angular accelerations of the points and angles. The updated angles initially calculated are then saved and used in the next time step, if necessary.

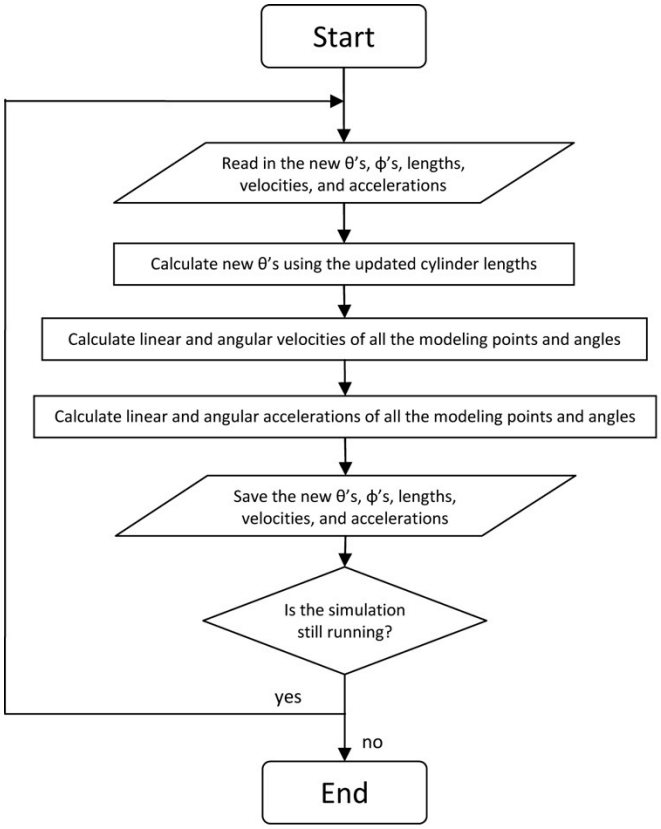

Figure 3.5 Kinematic Model Flowchart

3.3.1 General Position Solution

The starting point for the kinematic simulation is to read in an initialized set of θ angles and cylinder lengths. With the exception of the initial run of this program, the set of θ angles that are read into the program are the exact values from the previous time step. For the purpose of this discussion, it will be assumed that the values of θ used at the beginning of the calculations at

each time step may not exactly describe the correct orientation of the system (as the controlling actuators may have changed in length), and will need to be corrected before completing further kinematic analysis. Observing Figure 3.4, it can be seen that a number of linkages joining the modeling points together form closed shapes; some of these closed shapes will be used to solve for the values of θ, based on the newly updated cylinder lengths supplied from the hydraulic model, which will be presented in Chapter 5.

From Figure 3.4, the three cylinders making up the workgroup are the dashed lines represented by $\overrightarrow{BC}, \overrightarrow{CE}$, and $\overrightarrow{FG}$; representing the boom, stick, and bucket cylinders, respectively. All other lines joining modeling points have a fixed length. It can also be observed that due to the fixed α angles, there exist some θ variables that can be calculated using geometric relationships. One example of this would be for θ_4. The relationship

$$\theta_4 = \theta_2 + \alpha_1 - \pi, \qquad [3.5]$$

allows θ_4 to be determined directly from θ_2. The discussion to follow will focus on the θ angles that cannot be directly determined from other angle values; they are uniquely based on the geometry of the system.

The θ angles that must be calculated at each time step are: θ_2, θ_3, θ_5, θ_6, θ_{11}, θ_{13}, θ_{14}, and θ_{15}. All other values can be determined from geometric relationships using the fixed α angles. The method used to solve for the values of θ is based on a "position-loop" approach. The basic principle, which will be expanded upon in the following section, is that for a given set of actuator lengths, the system will have a unique orientation. To determine this orientation, the system is divided into a number of sections, each of which contains three or four linkages that form a closed triangular or quadrilateral shape, which will be referred to as *loops* from this point forward. For a properly oriented group of linkages, it is expected that a path traced around the loop will start and finish at the same location; however, if the orientation of the linkages is not correct, the starting and ending location will not be at exactly the same place. The objective of the position modeling is to ensure the orientation of the system is correct for a given set of cylinder length inputs. There are four loops used to determine the eight unknown values of θ. Two independent loops of three linkages are used to solve for half of the variables, while two dependent loops of four linkages each are used to solve the remaining variables.

3.3.1.1 Independent Position Loops

The first system to be solved is the closed loop composed of modeling points A, B, and C, shown in Figure 3.6. Given the approximate values of θ_2 and θ_3, the length of the boom cylinder L_{BC} and the known value of θ_1, the exact values of θ_2 and θ_3 can be solved using an iterative process.

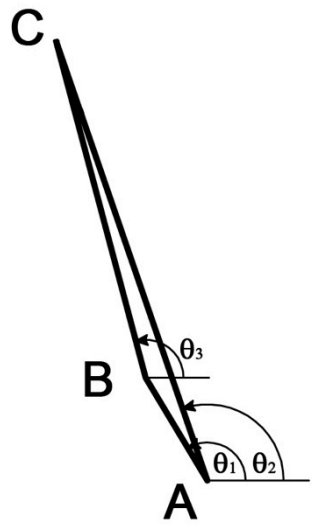

Figure 3.6 Position Loop A-B-C

The path traced around the position loop in Figure 3.6 can be written based on the path from A to B, B to C, and C back to A. It should be mentioned that the swing angle, ϕ, is not included in the position analysis, as it does not affect the orientation of the workgroup with respect to the ground plane. Based on Equations 3.3 and 3.4, the path around position loop A-B-C can be written as components in the $\hat{\imath}$ and $\hat{k}$ directions as

$$\hat{\imath}: f_1 = L_{AB}cos\theta_1 + L_{BC}cos\theta_3 - L_{AC}cos\theta_2 \text{ , and} \quad [3.6]$$

$$\hat{k}: f_2 = L_{AB}sin\theta_1 + L_{BC}sin\theta_3 - L_{AC}sin\theta_2 \text{ ,} \quad [3.7]$$

where:

$f_1, f_2 =$ The net change in position in the $\hat{\imath}$ and $\hat{k}$ directions as a path is traced around loop A-B-C $[m]$.

Noting that the path around the loop should result in no net change in position, Equations 3.6 and 3.7 are satisfied only when

$$F_1 = \begin{bmatrix} f_1 \\ f_2 \end{bmatrix} = \begin{bmatrix} 0 \\ 0 \end{bmatrix}. \quad [3.8]$$

Given that the only variables that are free to change are θ_2 and θ_3, Newton's method for a system of equations is used to find the exact values of θ_2 and θ_3. Defining the initial guess to be

$$\vartheta_{guess} = \begin{bmatrix} \theta_2 \\ \theta_3 \end{bmatrix}, \quad [3.9]$$

And the Jacobian as

$$J_1 = \begin{bmatrix} \partial f_1 / \partial \theta_2 & \partial f_1 / \partial \theta_3 \\ \partial f_2 / \partial \theta_2 & \partial f_2 / \partial \theta_3 \end{bmatrix} = \begin{bmatrix} L_{AC} sin\theta_2 & -L_{BC} sin\theta_3 \\ -L_{AC} cos\theta_2 & L_{BC} cos\theta_3 \end{bmatrix}, \quad [3.10]$$

allows the change in the initial guess to be calculated from

$$\Delta\vartheta = -[J_1]^{-1} F_1. \quad [3.11]$$

The quantity of $\Delta\vartheta$ can be used to adjust the initial guess to provide an improvement to Equation 3.8, forcing F_1 closer to zero, such that

$$\vartheta_{next\ guess} = \vartheta_{guess} + \Delta\vartheta. \quad [3.12]$$

This process is repeated until the magnitude of $\Delta\vartheta$ is such that it no longer has a substantial effect on subsequent approximations of $\vartheta_{next\ guess}$. For this simulation, the value of $\vartheta_{next\ guess}$ is taken to be exact when both elements of $\Delta\vartheta$ are less than 0.00573° (0.0001 radians). This process provides an exact solution for θ_2 and θ_3, and θ_4 can also be determined from Equation 3.5.

The same sequence of steps is used to solve for θ_5 and θ_6 of the position loop formed by the vectors from C to D, D to E, and E to C. Solving for the exact values of θ_5 and θ_6 allows for θ_7, θ_8, θ_9, θ_{10}, and θ_{16} to be solved, similar to θ_4 in Equation 3.5.

3.3.1.2 Dependent Position Loops

Determining the exact values for the angles affected by motion of the bucket cylinder uses the same method discussed in the previous section, but requires that two loops composed of four linkages each be used to solve directly for θ_{11}, θ_{13}, θ_{14}, and θ_{15}. This exact solution allows the last remaining angle, θ_{12}, to be determined indirectly using a geometrical relationship. The linkages used in the two position loops are shown in Figure 3.7. The first loop is formed by the

vectors from H to I, I to K, K to J, and J to H. The vectors from F to G, G to I, I to H, and H to F form the second loop.

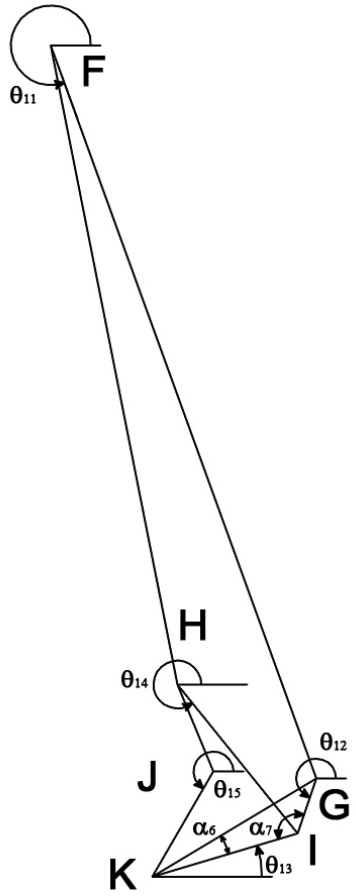

Figure 3.7 Position Loops H-I-K-J and F-G-I-H

The method of solving for the exact values of θ_{11}, θ_{13}, θ_{14}, and θ_{15} is the same as discussed in the previous section; except there are now four equations being solved simultaneously as opposed to two in the previous section. Solving for the remaining angles provides a complete orientation of the backhoe workgroup for a given set of cylinder lengths. The complete sets of equations used in the position analysis are provided in Appendix B.

3.3.2 General Velocity Solution

With the full orientation and location of all modeling points known, there is enough information present to perform a velocity analysis on the backhoe workgroup. The objective of the velocity analysis is to solve for both the linear velocity of all modeling points, and to solve for the angular velocity of each modeled linkage. This will be accomplished using a relative velocity approach:

the velocity of each point, and rotational velocity of each linkage can be found by starting at the pivot point of the workgroup (labeled point A in Figure 3.3), and developing relationships between the remaining modeling points moving away from point A, to point K. The velocities of the points and angles are defined relative to the subsequent points. The general solution and approach will be presented in this section, and Appendix B contains the fully developed equations.

It is known that the motion of the workgroup actuators drives the motion of the system, and the position analysis takes the change in length of these three actuators and determines the orientation of the system. The velocity analysis will focus on how fast each point and angle are changing magnitude. Written in general terms between two points, for example A and B, and given that the velocity of point A is known, the velocity of point B (relative to point A) can be expressed as

$$\overrightarrow{V_B} = \overrightarrow{V_A} + \frac{dr_{B/A}}{dt}\hat{u}_{B/A} + \vec{\omega}_{AB}\times\vec{r}_{B/A}, \qquad [3.13]$$

where:

$\overrightarrow{V_B}, \overrightarrow{V_A}$ = The velocity of the point denoted by the subscript $\left[\frac{m}{s}\right]$,

$\frac{dr_{B/A}}{dt}$ = The rate change in length of the linkage between points A and B $\left[\frac{m}{s}\right]$,

$\hat{u}_{B/A}$ = The unit vector representing the direction traveling from point A to point B,

$\vec{\omega}_{AB}$ = The rotational velocity of the linkage between points A and B $\left[\frac{rad}{s}\right]$, and

$\vec{r}_{B/A}$ = The vector from point A to B; alternatively expressed as

$\vec{r}_{B/A} = L_{AB}\hat{u}_{B/A}[m]$.

The first term in Equation 3.13 states that the velocity of point B will have the same velocity of point A; which would be true if both points were contained on a body with no rotation traveling with translational motion only. The second term accounts for any lengthening or shortening between points A and B. In the case of the backhoe, this sliding motion will apply to the boom, stick, and bucket actuators only. The final term accounts for the rotational motion of the system. The pinned nature of the backhoe joints gives rise to a potential for point B to rotate relative to point A. The rotation of a given linkage on the backhoe can be due to two sources: First, any

changes in the swing angle will create a rotation of the workgroup about the vertical z-axis. The swing rotation is common to the entire workgroup, as all the linkages are connected in the same plane. The second source of rotation is due to changes in the θ angles. This rotation will be about an axis along the horizontally pinned connection of the linkage. These two rotations describe the direction of the $\vec{\omega}_{AB}$ term in Equation 3.13. Figure 3.8 shows the direction vectors of the rotation.

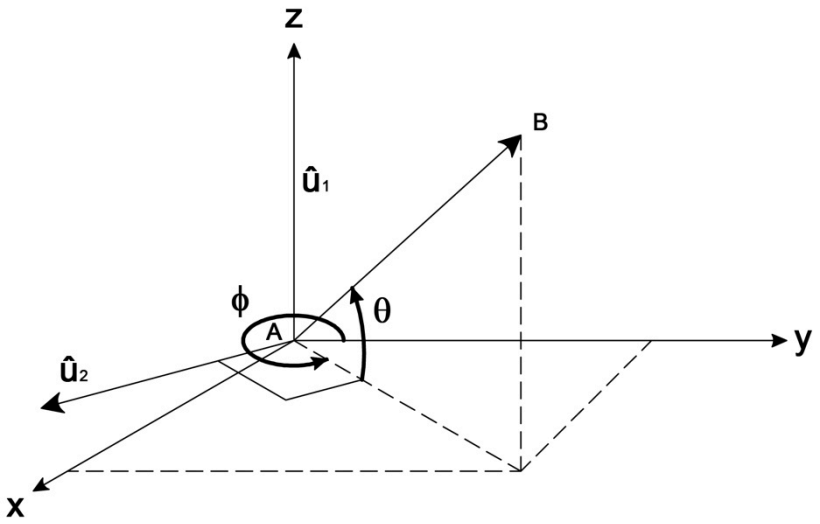

Figure 3.8 Unit Vectors for Rotation

The two unit vectors that compose the rotational vector $\vec{\omega}_{AB}$ can be expressed in terms of θ and ϕ, such that

$$\vec{\omega}_{AB} = \omega_1 \hat{u}_1 + \omega_2 \hat{u}_2, \qquad [3.14]$$

where:

$\omega_1 = \frac{d\phi}{dt}$, is the swing rotation $\left[\frac{rad}{s}\right]$,

$\hat{u}_1 = \hat{k}$, is the direction of the swing rotation,

$\omega_2 = \frac{d\theta}{dt}$, is the rotation of the linkage about the pinned joints $\left[\frac{rad}{s}\right]$, and

$\hat{u}_2 = cos\phi\ \hat{\imath} + sin\phi\ \hat{\jmath}$, is the direction of the rotation caused by the motion of the boom, stick, and bucket motions.

Using Equations 3.13 and 3.14, the velocity of all points and linkages can be expressed relative to at least one other point on the body. Assuming that point A and B on Figure 3.3 are fixed provides the required initial conditions to solve the set of equations produced. The method of solution involves reducing the body shown in Figure 3.4 to a number of loops, similar to the position solution. The relative velocity equations can be written for the points in the loop, and then matrix inversion is used to solve for the unknown linear and rotational velocities. In total, there are 39 velocity equations used to solve for 35 unknown variables. There are eight linkages composing the backhoe workgroup, and 16 θ-angles measured with respect to the ground. There are a number of situations where two or more θ-angles on a single body will have different values, but the same rate of rotation. One example of this is the relationship discussed in Equation 3.5. Both θ_2 and θ_4 have different values, but are members of the boom linkage and thus have the same angular velocities.

The velocity analysis is built upon the results of the position analysis, and provides a full set of linear and rotational velocity data for every point on the backhoe loader in three dimensions, although as it will be discussed in Chapter 4, the swing angle will be fixed, and the workgroup will be considered to have two-dimensional, planar motion only.

3.3.3 General Acceleration Solution

The final step in the kinematic modeling of the JD 410G is to include the mathematical relationships to represent the linear and angular accelerations of all the modeling points and linkages. The acceleration results are used in the kinetic modeling to predict the forces present in the system. A similar approach to the velocity analysis is used in this section, and a general solution will be presented. The starting point for analysis is from the general relative acceleration equation

$$\vec{A}_B = \vec{A}_A + \frac{d^2 r_{B/A}}{dt^2}\hat{u}_{\mathrm{B/A}} + 2\vec{\omega}_{AB}\times\frac{dr_{B/A}}{dt}\hat{u}_{\mathrm{B/A}} + \vec{\alpha}_{AB}\times\vec{r}_{B/A} + \vec{\omega}_{AB}\times\left(\vec{\omega}_{AB}\times\vec{r}_{B/A}\right), \quad [3.15]$$

where:

$\vec{A}_A, \vec{A}_B =$ The linear acceleration of the point denoted by the subscript $\left[\frac{m}{s^2}\right]$,

$\frac{dr_{B/A}}{dt} =$ The rate change in length along the linkage between points A and B $\left[\frac{m}{s}\right]$,

$\vec{\omega}_{AB}$ = The rotational velocity of the linkage between points A and B $\left[\frac{rad}{s}\right]$,

$\frac{d^2 r_{B/A}}{dt^2}$ = The rate change in velocity between points A and B $\left[\frac{m}{s^2}\right]$,

$\vec{\alpha}_{AB}$ = The angular acceleration of the linkage between points A and B $\left[\frac{rad}{s^2}\right]$, and

$\vec{r}_{B/A}$ = The position vector from point A to B$[m]$.

The right side of Equation 3.15 has five terms. While each term is written in a mathematical form, the physical meaning will be discussed to provide a sense of what the equation is describing. The physical meanings are discussed below in Table 3.2.

Table 3.2 Physical Description of the Terms in Equation 3.15

Term from Equation 3.15	Physical Meaning
$\vec{A}_A$	This term states that the acceleration of point B will have a component that is made up of the linear acceleration of point A. If both bodies were on the same rigid body that had only translational motion, the acceleration of point A and B would be the same.
$\frac{d^2 r_{B/A}}{dt^2}\hat{u}_{\mathrm{B/A}}$	This term is a measure of the acceleration of the linkage joining point A and B, in the direction from A to B. This sliding term will only be experienced on the three actuators.
$2\vec{\omega}_{AB}\times\frac{dr_{B/A}}{dt}\hat{u}_{\mathrm{B/A}}$	A component of the acceleration experienced at point B will be due to the combination of the rotational and linear velocities of the linkage. This term will only apply to the three actuators. This term can also be referred to as a Coriolis effect.
$\vec{\alpha}_{AB}\times\vec{r}_{B/A}$	Similar to the velocity equation, some of the acceleration at point B will be due to the rotational acceleration of the linkage acting over the length of the linkage. This is a tangential acceleration.

Term from Equation 3.15	Physical Meaning
$\vec{\omega}_{AB}\times(\vec{\omega}_{AB}\times\vec{r}_{B/A})$	The last term is centripetal acceleration. The part of the term inside the brackets represents a velocity of point B relative to point A due to the rotation and length of the linkage. This velocity also causes a rotational acceleration due to the change in direction of the velocity vector in the brackets.

Using the geometry and variable definitions presented earlier in this chapter, Equation 3.15 can be simplified into two general solutions. One solution is presented for a linkage that is an actuator having the ability to change length; the remaining solution is suitable for all other rigid linkages in the system. For simplicity, the following solutions are presented in their directional components along each axis.

For an actuator

$\hat{\imath}$: $A_{Bx} =$

$$A_{Ax} - \frac{d^2r_{B/A}}{dt^2}cos\theta sin\phi + 2\frac{dr_{B/A}}{dt}\left(\frac{d\theta}{dt}sin\theta sin\phi - \frac{d\phi}{dt}cos\theta cos\phi\right) + L_{AB}\left[\frac{d^2\theta}{dt^2}sin\theta sin\phi + 2\frac{d\theta}{dt}\frac{d\phi}{dt}sin\theta cos\phi - \frac{d^2\phi}{dt^2}cos\theta cos\phi + \left[\left(\frac{d\theta}{dt}\right)^2 + \left(\frac{d\phi}{dt}\right)^2\right]cos\theta sin\phi\right], \quad [3.16]$$

$\hat{\jmath}$: $A_{By} =$

$$A_{Ay} + \frac{d^2r_{B/A}}{dt^2}cos\theta cos\phi + 2\frac{dr_{B/A}}{dt}\left(-\frac{d\theta}{dt}sin\theta cos\phi - \frac{d\phi}{dt}cos\theta sin\phi\right) + L_{AB}\left[-\frac{d^2\theta}{dt^2}sin\theta cos\phi + 2\frac{d\theta}{dt}\frac{d\phi}{dt}sin\theta sin\phi - \frac{d^2\phi}{dt^2}cos\theta sin\phi - \left[\left(\frac{d\theta}{dt}\right)^2 + \left(\frac{d\phi}{dt}\right)^2\right]cos\theta cos\phi\right], \text{ and} \quad [3.17]$$

$\hat{k}$: $$A_{Bz} = A_{Az} + \frac{d^2r_{B/A}}{dt^2}sin\theta + 2\frac{dr_{B/A}}{dt}\frac{d\theta}{dt}cos\theta + L_{AB}\left[\frac{d^2\theta}{dt^2}cos\theta - \frac{d\theta}{dt}sin\theta\right]. \quad [3.18]$$

Equations 3.16-3.18 represent the most complex form of the relative acceleration equation. For the case of a rigid linkage, the time-dependent sliding terms are removed, giving a more simple form of these equations as

$$\hat{\imath}: \quad A_{Bx} = A_{Ax} + L_{AB}\left[\frac{d^2\theta}{dt^2}sin\theta sin\phi + 2\frac{d\theta}{dt}\frac{d\phi}{dt}sin\theta cos\phi - \frac{d^2\phi}{dt^2}cos\theta cos\phi + \left[\left(\frac{d\theta}{dt}\right)^2 + \left(\frac{d\phi}{dt}\right)^2\right]cos\theta sin\phi\right], \quad [3.19]$$

$$\hat{\jmath}: \quad A_{By} = A_{Ay} + \left[-\frac{d^2\theta}{dt^2}sin\theta cos\phi + 2\frac{d\theta}{dt}\frac{d\phi}{dt}sin\theta sin\phi - \frac{d^2\phi}{dt^2}cos\theta sin\phi - \left[\left(\frac{d\theta}{dt}\right)^2 + \left(\frac{d\phi}{dt}\right)^2\right]cos\theta cos\phi\right], \text{ and} \quad [3.20]$$

$$\hat{k}: \quad A_{Bz} = A_{Az} + L_{AB}\left[\frac{d^2\theta}{dt^2}cos\theta - \frac{d\theta}{dt}sin\theta\right]. \quad [3.21]$$

Equations 3.16-3.21 are used in the exact same method of loops used in the velocity analysis, building on the results obtained from the position and velocity analyses. Completion of the acceleration analysis provides a full set of kinematic data for all the modeling points and linkages of the JD 410G backhoe workgroup.

3.4 Kinematic Model Implementation

The position, velocity, and acceleration equations introduced in the previous section and presented in detail in Appendix B were used to create a kinematic model in the MATLAB Simulink software package. Instead of using an object-oriented method to build the kinetic model (as will be done with the hydraulics), the Embedded MATLAB Function is implemented, which allows a coded file to be used within the Simulink modeling environment. The code contained within the block is included in Appendix C.

3.5 Kinematic Model Validation

To ensure the equations presented in the previous section are able to recreate the motion of the actual system, a simple verification was performed for the position and velocity equations. The

measurement equipment available did not allow the acceleration to be verified, but this will be done qualitatively in Chapter 4 (as the linear and angular accelerations are used in the kinematic model). To verify that the kinematic model was performing correctly, the JD 410G backhoe was equipped with as many as four string potentiometers. The string potentiometers were used to measure the length of the boom, stick, or bucket cylinder, as well as up to three other lengths on the system. Table 3.3 lists the parameters measured on the backhoe using the string pots.

Table 3.3 Measured Parameters for the Kinematic Model Validation

Backhoe Function	Measured Parameters
Boom Cylinder	L_{AK}, L_{BD}, L_{BK}
Stick Cylinder	L_{BK}
Bucket Cylinder	L_{AK}, L_{BK}, L_{FK}

Due to the limited number of string pots available and the limited measurement range of each string potentiometer, each backhoe function was measured independently from the others. The parameters L_{AK} and L_{BK} have been selected as the position of point K predicted by the kinematic model is expected to have the largest accumulated error; the location of point K is determined by equations starting from the main pivot point (point A), and following the linkages along the workgroup. Any deviation between the simulation and the real system will accumulate and should be a maximum at point K. For the stick cylinder function, only parameter L_{BK} was measured, as the large span between the points B and K required two string potentiometers, not allowing any additional parameters to be measured. In the case of the boom and bucket functions, the additional parameters were measured. L_{BD} was measured on the boom function to ensure no excessive errors were generated in the boom section. L_{FK} was measured on the bucket function for the same reason.

With the string potentiometers attached to the appropriate points on the backhoe, each function was put through the same process to collect data. The cylinder of interest was extended (or retracted) from the home position, and moved over the entire stroke of the cylinder, and then back to the home position. As the cylinder was moved, it was stopped incrementally over the

stroke and data was collected while the cylinders were not moving. This was done to provide a large number of data points at a variety of stops along the stroke, allowing random noise to be easily filtered from the data. Each cylinder repeated this process five times to ensure repeatable and reliable data.

Each of the measured parameters were then plotted as a function of the controlling backhoe function, and a polynomial curve was fitted to this data, to be used to compare the simulated results directly to the experimental results. The simulation results were generated by moving each cylinder away from the home position to the end of its stoke. Each simulation was run over a 25 second period, using a time step of 0.1 seconds. The velocity inputted to the simulation was the length of the particular cylinder's stroke divided by the simulation time.

The simulated results were then plotted along with the directly measured data (all five sets of data are plotted together), as well as the curve fitted results for comparison. The curve fitted experimental data was directly compared to the simulated data to provide an approximation of the separation between the experimental and simulated data.

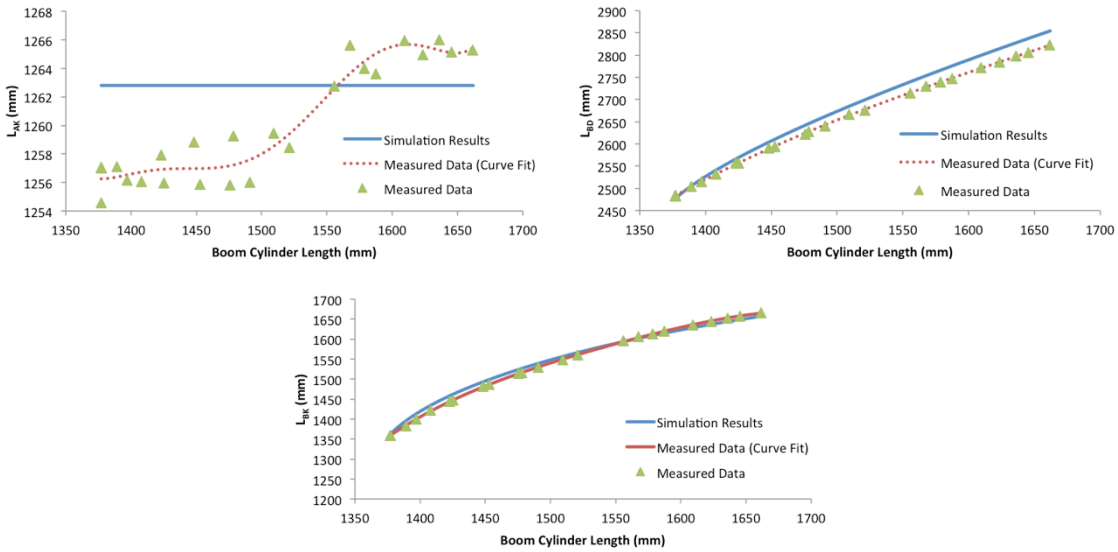

Figure 3.9 Experimental and Simulated Kinematic Results for the Boom Cylinder

The results in Figure 3.9 are for the boom cylinder function, and it should be mentioned that due to spatial limitations, the boom cylinder could only be extended by about 30% of its complete stroke before the workgroup would strike the ground. Note that the scaling of the vertical axis

on the L_{AK} plot is of a different order of magnitude of the other plots. The plot for L_{AK} shows that when the boom cylinder is between 1500-1550 mm, the measured length of L_{AK} experiences a change in length that is not predicted in the simulated results. The reason for this is that the kinematic model does not take into account the tolerances of the pinned joints in the system. Somewhere between a boom cylinder length of 1500-1550 mm, the center of gravity of the workgroup passes over the pin at point A, explaining this change in length of L_{AK}. This phenomenon is not obvious in the other two plots, as the lengths of L_{BK} and L_{BD} are not constant.

The plot for L_{AK} in Figure 3.9 also provides a sense of the experimental error present in the measured data. Observing that for any two points that occur at similar values of boom cylinder stroke, there exists some separation of the measured values. For example, the two points occurring at a boom cylinder length of approximately 1475 mm have measured L_{AK} values of about 1256 mm and 1260 mm over the five sets of collected data. This appears to be the greatest separation between experimentally measured values in the data set; it is expected that all subsequent measured results will fall within this envelope of experimental separation.

Comparison of the simulated results to the experimentally measured values reveals that the maximum encountered separation occurred with L_{AK}, having a separation of 1.12%. This is largely expected to be a result of the *play* in the pinned joints in the system. The other two parameters, L_{FK} and L_{BK} had a maximum separation of 1.02%. The average separation between the simulated and measured data is 0.53%.

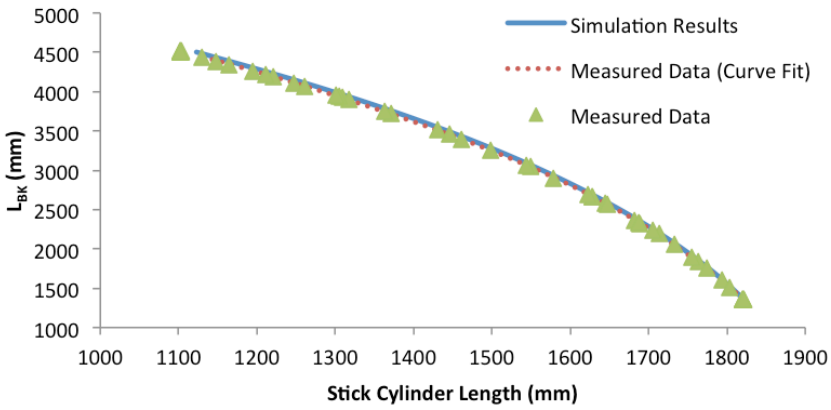

Figure 3.10 Experimental and Simulated Kinematic Results for the Stick Cylinder

As mentioned, due to the large separations between points caused by motion of the stick cylinder and the limited range of the string potentiometers, only L_{BK} was recorded as a function of stick cylinder length, as shown in Figure 3.10. The greatest separation between the experimental and simulated results was 1.47%, with an average difference of 0.99%.

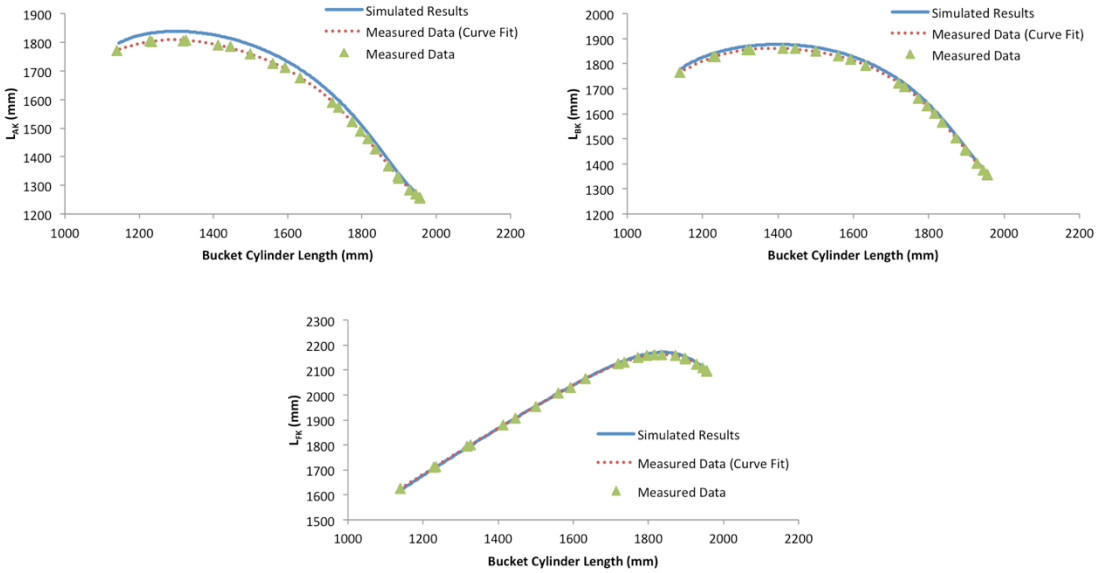

Figure 3.11 Experimental and Simulated Results for the Bucket Cylinder

Figure 3.11 shows the comparison of the simulated and measured results for the bucket cylinder function. The largest separation is encountered between the measured and simulated values of L_{FK}, at 1.87%. The average separation between the three measured lengths was 0.86%.

The largest separation between simulated and experimentally measured lengths occurred when moving the bucket cylinder, and was between the values for L_{FK}, having a value of 1.87%. It is assumed that all other quantities on the system that were not measured should fall into this same amount of error, and that the agreement between simulated and experimental results validates the kinematic model's position and velocity components. The acceleration was not considered in the validation, and will be qualitatively validated in Chapter 4. The main source of discrepancy between the simulated and experimental results that is expected to be responsible for the majority of the error in the results is the *play* in the pinned connections of the system that was not considered in the kinematic model. No validation of the swing function was considered, as the swing will not be used in the final modeling of the system, as will be discussed in Chapter 4.

Chapter 4: Kinetic Modeling

4.1 Kinetic Modeling Objectives

The kinetic modeling of the JD 410G backhoe will focus on the forces acting within the workgroup. The objective of the kinetic modeling is to predict the forces acting at each modeling point within the system as the orientation is changed. While the forces at all modeling points will be determined, it is the forces acting on the boom, stick, and bucket *actuators* that are the main objective from the kinetic analysis. The kinetic analysis will consider the swing angle, ϕ, of the workgroup to be fixed such that the motion of the system is restricted to planar motion in the plane of the workgroup. Fixing the swing angle reduces the kinetic analysis by one degree of freedom, down to two-dimensions.

4.2 Kinetic Modeling Approach and General Equations

The JD 410G backhoe is made up of eight bodies to be modeled, shown in Figure 4.1. There are the three hydraulic cylinders, the boom, stick, and bucket bodies, as well as the two bucket guide pieces.

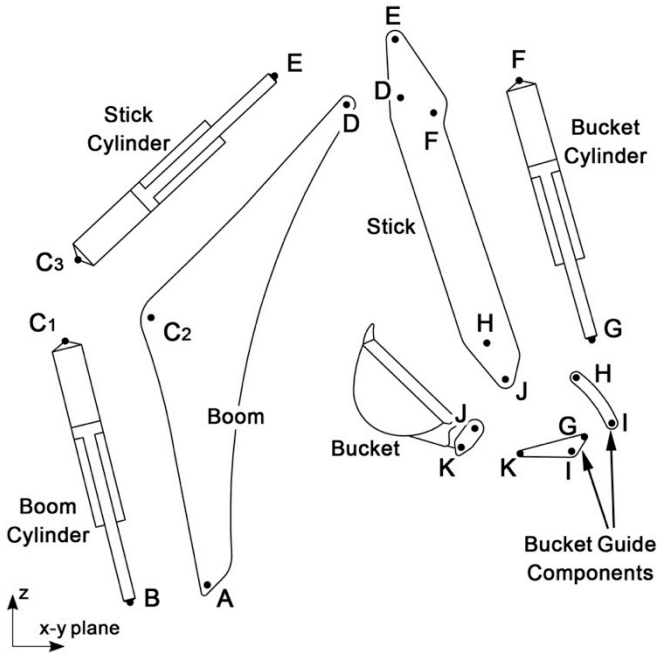

Figure 4.1 Kinetic Modeling Components of the JD 410G Backhoe

The labels assigned to each of the points on the backhoe are the same as in previous chapters, with the exception of point C, where there are now three different points, labeled as C_1, C_2, and C_3. This has been done because point C connects three bodies by means of a single pinned joint; analysis of this point will require an additional relationship that is not used in the other pinned connections. The kinetic analysis will solve for the forces acting at each point labeled in Figure 4.1, and from these forces, the loads acting on the three actuators can be calculated to be used in the hydraulic modeling presented in Chapter 5.

The *general* kinetic equations can be developed by considering the body presented in Figure 4.2. The arbitrarily shaped body has four forces acting upon it, labeled F_1, F_2, F_3, and F_4. The center of gravity of the body acts through point G.

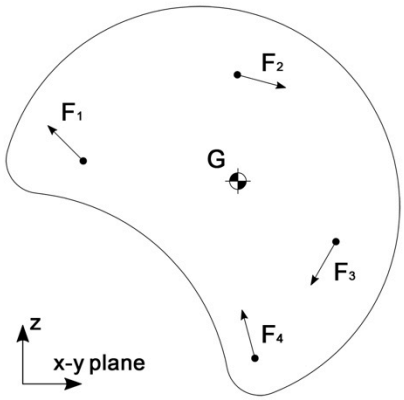

Figure 4.2 Kinetic Modeling Body

If the body in Figure 4.2 is moving with a linear acceleration of A_G and a rotational acceleration of α, then the two kinetic equations can be written as

$$\sum \vec{F} = m\vec{A}_G, \text{ and} \quad [4.1]$$

$$\sum \vec{M}_G = I_G\, \alpha, \quad [4.2]$$

where:

$\vec{A}_G =$ The linear acceleration of the center of gravity, G $\left[\frac{m}{s^2}\right]$,

$m =$ The mass of the body [kg],

$\vec{M}_G =$ Moment caused about point G, with the counterclockwise direction taken as positive $[\mathrm{N} \cdot \mathrm{m}]$,

$I_G =$ The mass moment of inertia of the body taken about the center of gravity, point G $[\mathrm{kg} \cdot \mathrm{m}^2]$, and

$\alpha =$ The rotational acceleration of the body $\left[\frac{\mathrm{rad}}{\mathrm{s}^2}\right]$.

The kinematic modeling of the JD 410G backhoe uses a number of simplifying assumptions, listed as:

1. All eight components are rigid bodies,
2. The hydraulic actuators and two bucket guide pieces have negligible mass; only the boom, stick and bucket are assumed to have mass,
3. Mass distributions are assumed even throughout the boom, stick, and bucket bodies,
4. The hydraulic actuators supply all applied forces,
5. The hydraulic actuators are subject only to viscous friction, which will be lumped into the actuator hydraulic models, and
6. Pin friction is neglected.

The assumption that only the boom, stick, and bucket have mass will simplify Equations 4.1 and 4.2 for the remaining five components, but will require the center of gravity location to be determined for the boom, stick, and bucket.

4.3 Center of Gravity and Mass Moment of Inertia Estimation

Without the availability of manufacturer-supplied CAD drawings, or advanced measurement equipment, the exact location of the center of gravity of the boom, stick, and bucket could be determined; however, the approximate location was determined using digital imaging and CAD software.

First, a digital photograph was taken of the backhoe workgroup, and is shown in Figure 4.3. Special care was given to ensuring the camera was perpendicular to the workgroup, and that the backhoe was centered on the image to avoid lens distortion (Figure 4.3 has been cropped). The

image was then imported into AutoCAD, and each of the boom, stick, and bucket linkages were traced over the image. Using the measured lengths contained in Table 3.1 of Chapter 3, the drawing was then scaled to be the same size as the real system.

Figure 4.3 John Deere 410G Backhoe Workgroup

The scaled outlines of the boom, stick, and bucket portions of the backhoe were then used with AutoCAD's MASSPROP command to determine the center of gravity location (based on the area of the bodies), and the area moment of inertia of each body. Recall that Equation 4.2 requires the mass moment of inertia of the body, while AutoCAD has estimated the area moment of inertia. There exists a relationship between the mass moment of inertia and the area moment of inertia, such that

$$I_{mass} = \rho t \, I_{area}, \qquad [4.3]$$

where:

I_{mass} = The mass moment of inertia $[kg\ m^2]$,

I_{area} = The area moment of inertia $[m^4]$,

ρ = The density of the body material $\left[\frac{kg}{m^3}\right]$, and

t = The thickness of the body material $[\,m]$.

The body thickness is approximated to be t = 0.02 m, and this value represents the thickness of the walls of the body that are the walls of the body that are along the plane of the backhoe workgroup. The density is taken as a typical value for steel, as a typical value for steel, as ρ = 7800 $\frac{kg}{m^3}$. Using these values,

Table 4.1 can be completed, showing the AutoCAD-supplied area moment of inertia, and the adjusted mass moment of inertia for the boom, stick, and bucket.

Table 4.1 Summary of Moment of Inertia Values used in the Kinetic Modeling

Backhoe Component	**Area Moment of Inertia** $(\boldsymbol{m^4})$	**Mass Moment of Inertia** $(\boldsymbol{kg\ m^2})$
Boom	0.6650055	103.741
Stick	0.4380417	68.335
Bucket	0.0568424	8.867

The center of gravity location was also estimated for the boom, stick, and bucket bodies. Figure 4.4 shows the center of gravity locations, labeled as points r, s, and t, on the boom, stick, and bucket, respectively. The bucket is shown as having two center of gravity locations; the point t_1 depicts the location for the unloaded bucket, while point t_2 is an estimation of the center of gravity location of a fully loaded bucket.

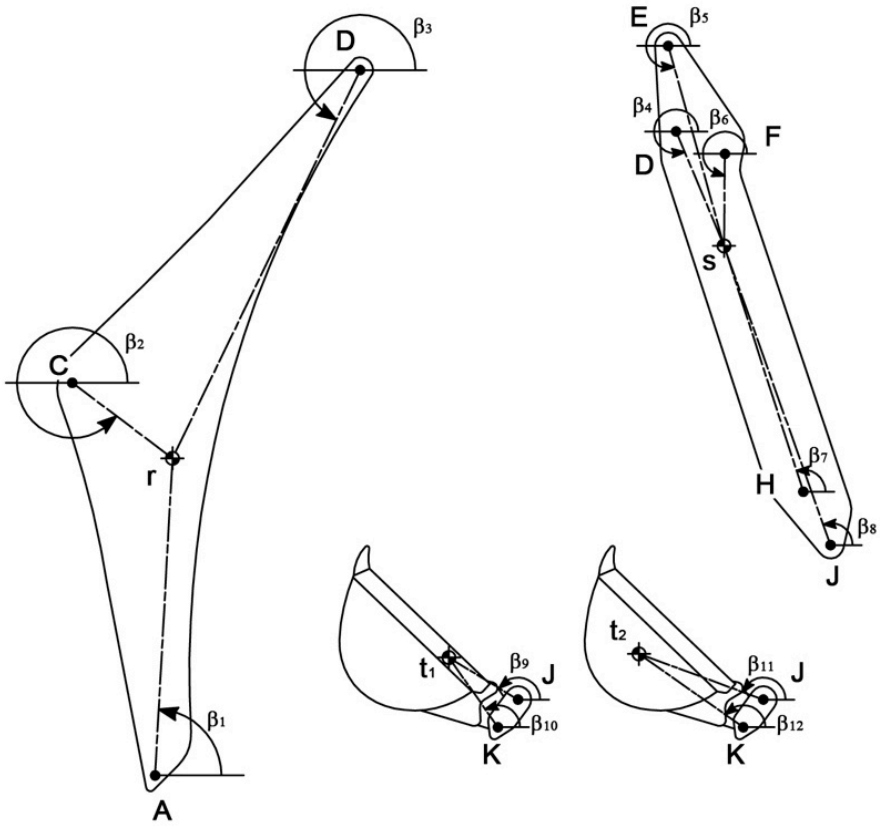

Figure 4.4 Estimated Center of Gravity Locations for the Boom, Stick, and Bucket

The dashed lines in Figure 4.4 depict the linkages connecting the modeling points on each body with the center of gravity location. The orientations of these linkages are defined by the 12 β-labeled angles. The values of the β angles are calculated using the fixed α angles, and solved values of θ from the kinematic analysis. The relationships for these angles are provided in Appendix D. The location of points r, s, t_1, and t_2 are included in Table 4.2.

Table 4.2 Center of Gravity Linkage Lengths

Boom	
Linkage	Measured Length
	(m)
L_{AR}	1.465
L_{CR}	0.622
L_{DR}	1.416

Stick	
Linkage	Measured Length
	(m)
L_{DS}	0.822
L_{ES}	1.176
L_{FS}	0.62
L_{HS}	1.049
L_{JS}	1.285

Bucket	
Linkage	Measured Length
	(m)
L_{JT1}	0.539
L_{KT1}	0.465
L_{JT2}	0.662
L_{KT2}	0.597

In order to determine the acceleration of points r, s, and t, a simple set of kinematic relationships have been developed, based on the analysis and method described in Chapter 3. Given that the kinematic analysis has been used to determine the velocities and accelerations of the modeling points on the backhoe workgroup, determining the accelerations of the center of gravity points requires that the relative velocity and acceleration equations be written from one point on each body to the center of gravity location. These relationships are provided in Appendix D.

4.4 Kinetic Modeling Equation Development

Using the outputs from the kinematic modeling, the solved kinematics of the center of gravity locations of each body, and applicable mass moments of inertia, the detailed kinetic relationships can be developed for each of the eight components making up the backhoe workgroup. The equation development process will be presented for the boom and boom cylinder only, as the process is identical for the remaining six bodies.

4.4.1 Boom Free Body Diagram and Kinetic Equations

Figure 4.5 shows a free body diagram (FBD) of the backhoe boom, labeled with forces at each of the modeling points, and the weight at the center of gravity. The forces are all shown in their components along the z-axis ($\hat{k}$-direction) and in the x-y plane (which, for a fixed value of ϕ = 270°, will simply be along the y-axis, or in the $\hat{\jmath}$-direction).

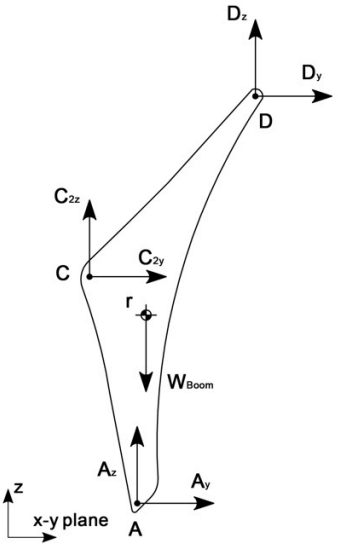

Figure 4.5 Boom Free Body Diagram

Using the free body diagram of Figure 4.5 and the angles defined in Figure 4.4, Equations 4.1 and 4.2 give

$$\hat{j}: A_y + C_{2y} + D_y = m_{Boom}A_{ry}, \quad [4.3]$$

$$\hat{k}: A_z + C_{2z} + D_z - W_{Boom} = m_{Boom}A_{rz}, \text{ and} \quad [4.4]$$

$$A_y L_{Ar}\left(-\sin(\beta_1)\right) + A_z L_{Ar}\left(cos(\beta_1)\right) + C_{2y} L_{Cr}\left(-\sin(\beta_2)\right) + C_{2z} L_{Cr}\left(cos(\beta_2)\right) + D_y L_{Dr}\left(-\sin(\beta_3)\right) + D_z L_{Dr}\left(cos(\beta_3)\right) = I_r \alpha_{Boom}. \quad [4.5]$$

The kinetic relationships for the stick and bucket linkages follow the same procedure as that of the boom.

4.4.2 Boom Cylinder Free Body Diagram and Kinetic Equations

Figure 4.6 shows the boom cylinder FBD. In comparison to the boom shown in Figure 4.5, the boom cylinder mass is assumed to be negligible, which negates the need for the center of gravity kinematics and moment of inertia.

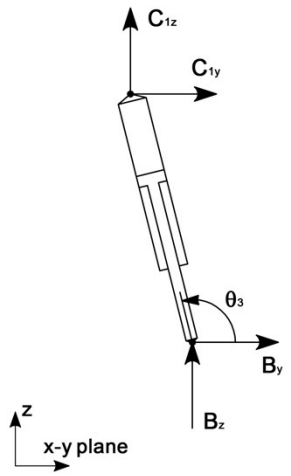

Figure 4.6 Boom Cylinder Free Body Diagram

Using the free body diagram of Figure 4.6, Equations 4.1 and 4.2 give

$$\hat{j}: C_{1y} + B_y = 0, \quad [4.6]$$

$$\hat{k}: C_{1z} + B_z = 0, \text{ and} \quad [4.7]$$

$$B_y sin(\theta_3) - B_z cos(\theta_3) - C_{1y} sin(\theta_3) + C_{1z} cos(\theta_3) = 0. \quad [4.8]$$

The development of Equation 4.8 is taken for a rotation about a point along the boom cylinder that is equidistant from points B and C_1. The kinetic relationships for the remaining cylinders and guides all follow the same procedure as for the boom cylinder.

4.5 Kinetic Model Implementation

Using the center of gravity kinematic results, the estimated mass moments of inertia, and the kinetic relationships developed for the eight components that make up the backhoe workgroup, the kinetic portion of the simulation was developed. Using a method similar to the acceleration analysis of Chapter 3, a total of 26 kinetic relationships were developed and organized into a matrix form. The kinetic equations are developed such that each of the modeling points contains two unknowns (the force in each direction), making for a total of 26 unknowns. The unknown forces are determined using a matrix inversion method at every time step; at the output of the kinetic analysis is the $\hat{\jmath}$ and $\hat{k}$ components of the force acting at every point on the body. The kinetic analysis is added into the *Embedded MATLAB Function* used for the kinematic analysis in such a way that the kinetic modeling is completed immediately after the kinematic modeling, and the code is presented in Appendix C.

The objective of the kinetic modeling was to determine the force acting along each of the three controlling actuators. In order to convert the forces from their components into a resultant quantity acting along the actuator, both the $\hat{\jmath}$ and $\hat{k}$ components of the force and the angle, θ, are used. Using the boom cylinder depicted in Figure 4.6 as an example, the force along the $\hat{\jmath}$ and $\hat{k}$ components can be written as

$$\hat{\jmath}: C_{1y} = F_{\substack{Boom \\ Cyl}} \cos(\theta_3), \text{ and} \qquad [4.9]$$

$$\hat{k}: C_{1z} = F_{\substack{Boom \\ Cyl}} \sin(\theta_3), \qquad [4.10]$$

where:

$F_{\substack{Boom \\ Cyl}}$ = The force along the boom cylinder $[N]$.

Equations 4.9 and 4.10 can be rearranged to both solve for the force along the boom cylinder, such that

$$\hat{j}: F_{\substack{Boom \\ Cyl}} = \frac{C_{1y}}{\cos(\theta_3)}, \text{ and} \quad [4.11]$$

$$\hat{k}: F_{\substack{Boom \\ Cyl}} = \frac{C_{1z}}{\sin(\theta_3)}. \quad [4.12]$$

To avoid division by zero, Equation 4.11 is used when θ_3 falls in the ranges of [45°, 135°] and [225°, 315°]. The value of cos θ is always nonzero in these ranges. For all other values of θ_3, Equation 4.12 is used to find the value of $F_{\substack{Boom \\ Cyl}}$. The same method is used to determine the forces along the stick and bucket cylinders. The signs of the forces in all three cylinders are such that when the actuator is in tension, the sign of the force is positive, and a compressive load has a negative sign.

4.6 Kinetic Model Outputs and Qualitative Validation

This section will present the outputs of the kinetic modeling in the form of the force along each of the three cylinders for a given input. Due to the lack of means to directly determine the center of gravity and moment of inertia of the boom, stick, and bucket linkages, the outputs from the kinetic modeling are not expected to match the real system with the same accuracy encountered in the kinematic modeling; nor was the required instrumentation available to accurately measure the forces along each actuator. In light of these shortcomings (which will also be experienced in the hydraulic modeling), it is not possible to do a direct, quantitative comparison between the real and simulated systems; rather, a logical approach will be applied to ensure the *trends* encountered in the results can be justified.

To perform this qualitative model validation, each of the three controlling actuators was given an input independent of the other two functions. These inputs are sent into the kinematic model developed in Chapter 3. The kinetic model generates the forces present in each of the three controlling actuators of the workgroup. Although it is realized that all three actuators will experience loading during motion, only the actuator driving the system will be considered in the following analysis. Figure 4.7 shows the general input curves used to generate outputs for examination. Each function will be simulated twice, with the two different signals shown in each plot of Figure 4.7. The set of data labeled as 'Sharp Input' will be first presented, and allows for some behaviors of the output force to be more prominent, while the second input,

labeled as 'Smooth Input' is considered to have a more realistic trend to the actual behavior of the system. Both inputs are designed to have the same steady-state velocity. Practical situations would occur somewhere in-between these two scenarios.

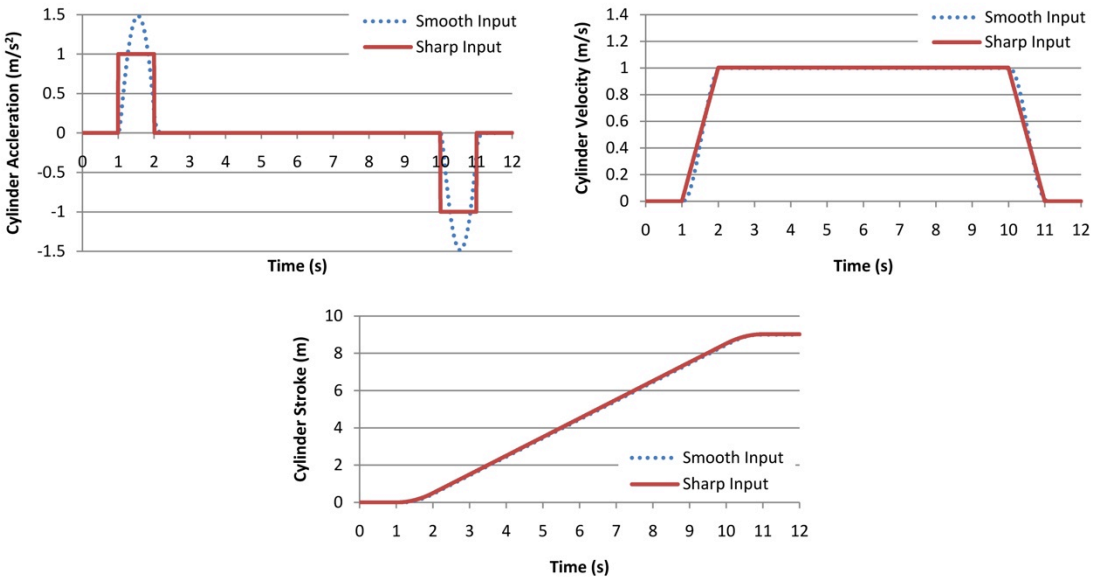

Figure 4.7 Input Signals for the Kinetic Validation

The scale of the plots in Figure 4.7 is arbitrary, such that the input velocity is unity for both sets of signals. The signals inputted to the model are scaled by an appropriate value to ensure each cylinder is allowed to travel through its entire stroke. The scaling value applied to the input signals for each cylinder are shown in Table 4.3. Note that the scaling factors for the stick and bucket functions are negative: this is because these two cylinders are starting from a fully extended stroke (in the home position) and must be retracted.

Table 4.3 Scaling Factors Applied to the Input Signals

Operating Cylinder	Applied Scaling Factor
Boom	0.09018
Stick	-0.06982
Bucket	-0.08100

As shown in Figure 4.7, each simulation is run for 12 seconds, with the system being held motionless for the first and last second of the runs. A fixed time step of 0.01 seconds is used for each of the six simulations.

As a visual aid, Figure 4.8 shows the home position, and the final stopping position for actuation of each of the three input functions. Note that this figure is not to scale, and is intended only to demonstrate the orientation of the system visually.

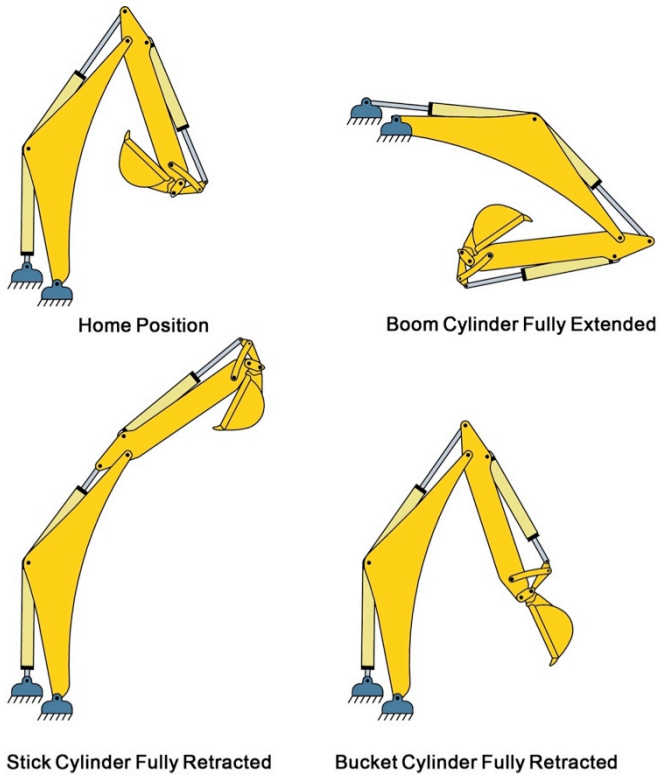

Figure 4.8 Beginning and Ending Positions of the System for each Input Signal

Figure 4.9 shows the output from the kinetic modeling in the form of the force experienced by the *boom* cylinder as it is extended throughout its stroke for the sharp input signals. The initial load on the cylinder indicates a tensile force, due to the orientation of the workgroup and the effect of gravity. Between points *a* and *b*, the actuator experiences a constant acceleration, applied in the form of a square wave shown in Figure 4.7. The edges of the square wave are the cause of the observed discontinuity, and it can be seen during this period the load on the actuator reduces; this is due to the inertial portion of the kinetic equations. As the workgroup is

accelerated, it initially resists motion, causing the load on the actuator to decrease, as the compressive load due to the acceleration will counteract a portion of the existing tensile load. Between *b* and *c,* the cylinder is traveling at a constant velocity, and the variations observed in the load are due to the changing orientation of the workgroup. As the actuator decelerates between *c* and *d*, the opposite effect of the acceleration is observed, as the workgroup's inertia wants to remain in motion. Stopping the load causes an increase in the tension experienced by the boom cylinder.

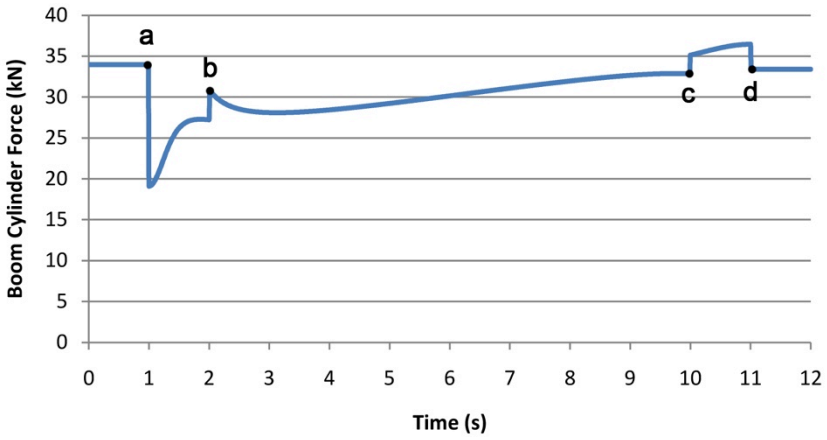

Figure 4.9 Boom Cylinder Loading due to the Sharp Input Signals

Figure 4.10 depicts the results obtained from the smooth input signals, and it can be observed that the same general trends are present; however, the discontinuities caused from the sharp input signals are no longer present. This is because the smooth input signals allow the acceleration and deceleration portions of the motion to be implemented gradually over time. The result is what is expected to be a more realistic behavior of the system (the input signals to the kinetic model will be dictated by the hydraulic modeling).

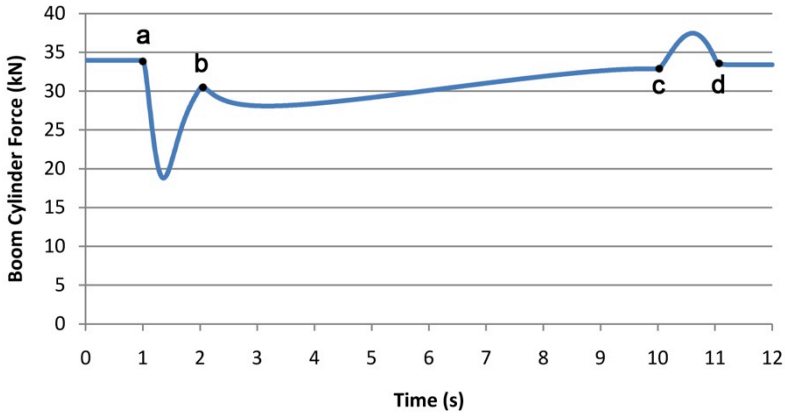

Figure 4.10 Boom Cylinder Loading due to the Smooth Input Signals

The plots shown in Figure 4.11 show the stick cylinder loading results for both input signal types. In contrast to the results for the boom cylinder, it can be seen that the acceleration and deceleration portions of the plots (between *a* and *b*, and *c* and *d*, respectively) have the opposite effect on the cylinder loading. This is due to the direction of the cylinder motion, as the stick cylinder is beginning from the fully extended position and must retract to pull the stick and bucket linkages up to their new orientations.

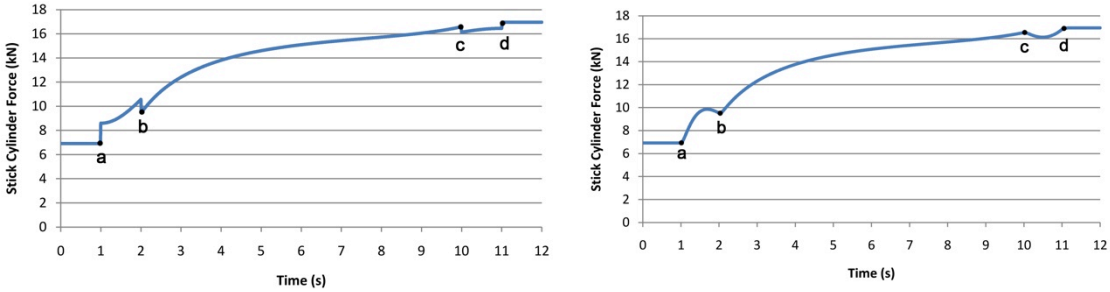

Figure 4.11 Stick Cylinder Loading for the Sharp (left) and Smooth (right) Input Signals

Finally, for the motion of the bucket cylinder, the results due to both input signal types are shown in Figure 4.12. The same trends as in the plots for the stick cylinder are experienced, although the loading due to the acceleration and deceleration sections (between *a* and *b,* and *c* and *d,* respectively) is considerably smaller than in the previous two functions. This is due to the fact that the bucket cylinder is responsible for moving the smallest mass and inertia of the three controlling functions, and as such, the bucket accelerates and decelerates with less effort relative to the other functions. Between *b* and *c* in both plots of Figure 4.12, it can be also be seen that the loading on the bucket cylinder changes from a compressive load to a tensile load at about

five seconds, which is not experienced by the simulations of the other two functions (although, they can also undergo this change depending on the orientation of the workgroup).

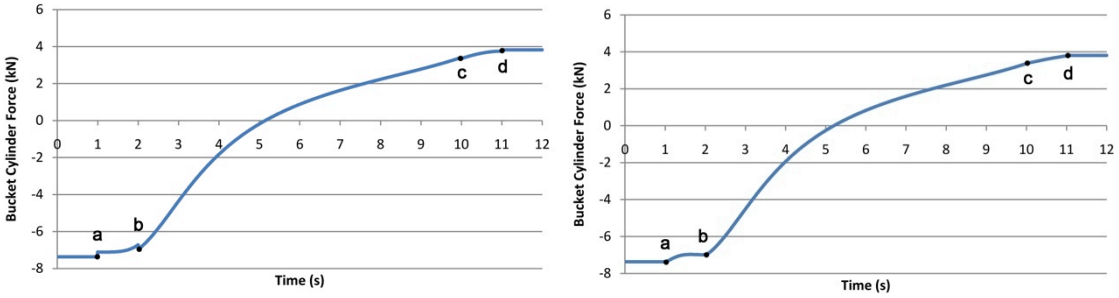

Figure 4.12 Bucket Cylinder Loading for the Sharp (left) and Smooth (right) Input Signals

As previously mentioned, due to the lack of CAD drawings or manufacturer specifications, it is not possible to perform a quantitative comparison between the simulated results and the kinetics of the real system. Rather, a qualitative assessment of the simulated results was performed to ensure the *trends* produced could be explained in a logical manner. This was achieved in this section, and although it is recognized that the magnitudes of the kinetic model outputs may deviate from the actual loads on the real system, it is expected that the process used to estimate the moment of inertia and center of gravity locations should provide an appropriate approximation.

Chapter 5: Hydraulic Modeling

5.1 Modeling Objectives

The final piece to the simulation model presented in this thesis is that of the hydraulic system. The hydraulic system bridges the gap between the operator and the motion of the workgroup. The objective of the hydraulic modeling is to develop a set of relationships to predict the pressures and flows in the system for a given set of control valve spool input positions. Due to the complexity of the load sensing system on the JD 410G and the inability to get access to components, a number of simplifications and assumptions have been made. Because of these constraints, many of the dynamics of components have not been modeled. The system to be modeled will be discussed in the following section.

5.1.1 General Hydraulic Circuit to be Modeled

The basic functionality of the hydraulic system of the JD 410G backhoe was presented in Chapter 2. This information will not be repeated, but will continue the development of the previously discussed system. As the three hydraulic circuits to be developed are all very similar in functionality, the modeling of the hydraulic system will be based on a generalized, single-function hydraulic circuit; the complete system model will then be generated by connecting three altered versions of the general model, with each containing a set of parameters specific to the function it is modeling.

Figure 5.1 and Figure 5.2 show the generalized circuit used in development of the hydraulic model of the backhoe workgroup. The hydraulic circuit has been divided into four flow paths, labeled in the figures. The four flow paths replace the function of the proportional control valve discussed in Chapter 2. The functionality of the circuit is such that flow paths 1 and 3 or 2 and 4 are used exclusively. For example, in Figure 5.1, using flow paths 1 and 3 and blocking paths 2 and 4 will result in an extension motion of the hydraulic cylinder, while Figure 5.2 shows that using flow paths 2 and 4 and blocking paths 1 and 3 will result in the hydraulic cylinder retracting.

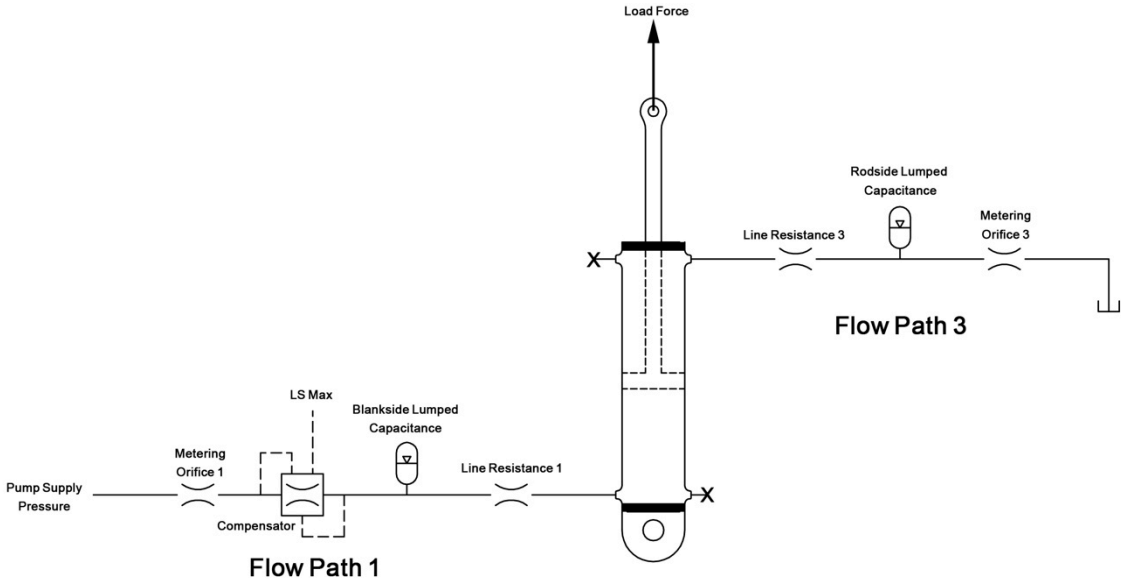

Figure 5.1 Simplified General Hydraulic Circuit for Extension

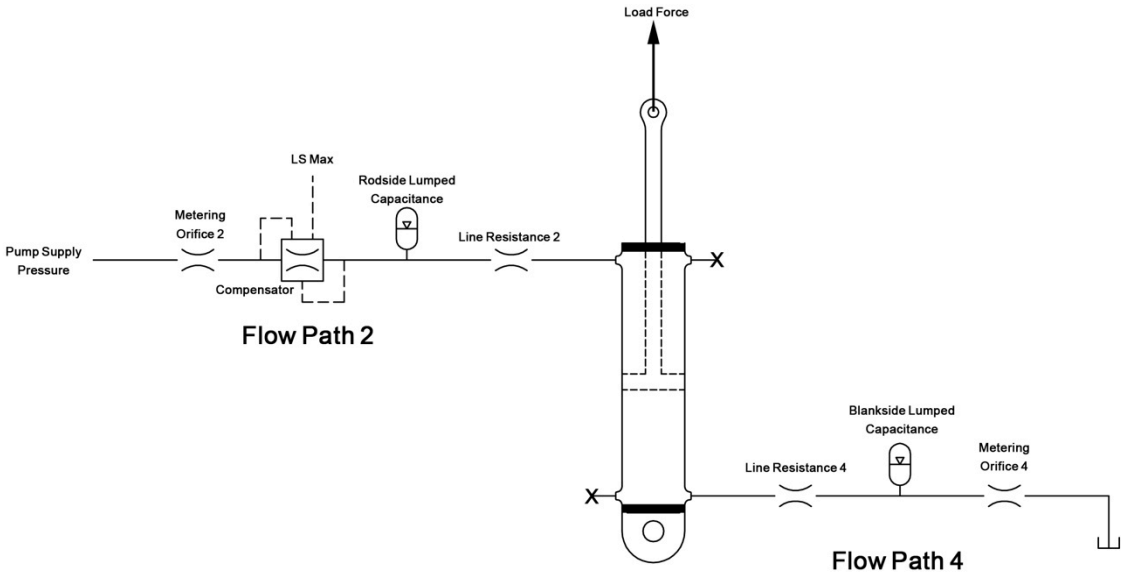

Figure 5.2 Simplified General Hydraulic Circuit for Retraction

This particular flow path approach was selected for the purpose of maintaining continuity in the simulation environment; had two flow paths been used, the resulting simulation would have required a set of integrators to be reset every time the hydraulic actuator's direction of travel changed, creating discontinuities in the output signals. This will be discussed further in following sections.

The load sensing pump portion of the circuit will not be modeled in this thesis, as the limitation in instrumentation and available information did not permit for the development of a useful model; instead, a pump supply pressure source will be used in place of a pump model. For a load sensing system, the supply pressure to each circuit is such that it is always higher than the required load pressure. This will be approximated in the simulation model by ensuring the pump supply pressure is always greater than the load pressure by a certain amount. This omission means that the appropriate dynamics of the pump could not be integrated into the overall boom, stick and bucket circuit system responses.

5.2 Power Bond Graph and Hydraulic Modeling Equations

5.2.1 Power Bond Graph of the Simplified Hydraulic Circuit

Based on the hydraulic circuit presented in Figure 5.1, the power flows through the circuit have been graphically represented using a *power bond graph* (PBG) approach. Herman et al. defines the PBG approach as "a structured language, which describes simultaneously the energetic exchanges between basic elements of the system as well as the origin of these exchanges by means of causality of relations" [4]. In the case of the general hydraulic circuit, the bond graph approach is used as a starting point to develop the basic relationships present in the system, such that the power bonds determine the causality of each equation. After the equations from the power bond graph are defined, further additions to the model will be done in such a way that the original causality is not altered. Further details on the power bond graph can be found in references [3, 4, and 8].

Figure 5.3 shows the PBG based on the model presented in Figure 5.1 and Figure 5.2.

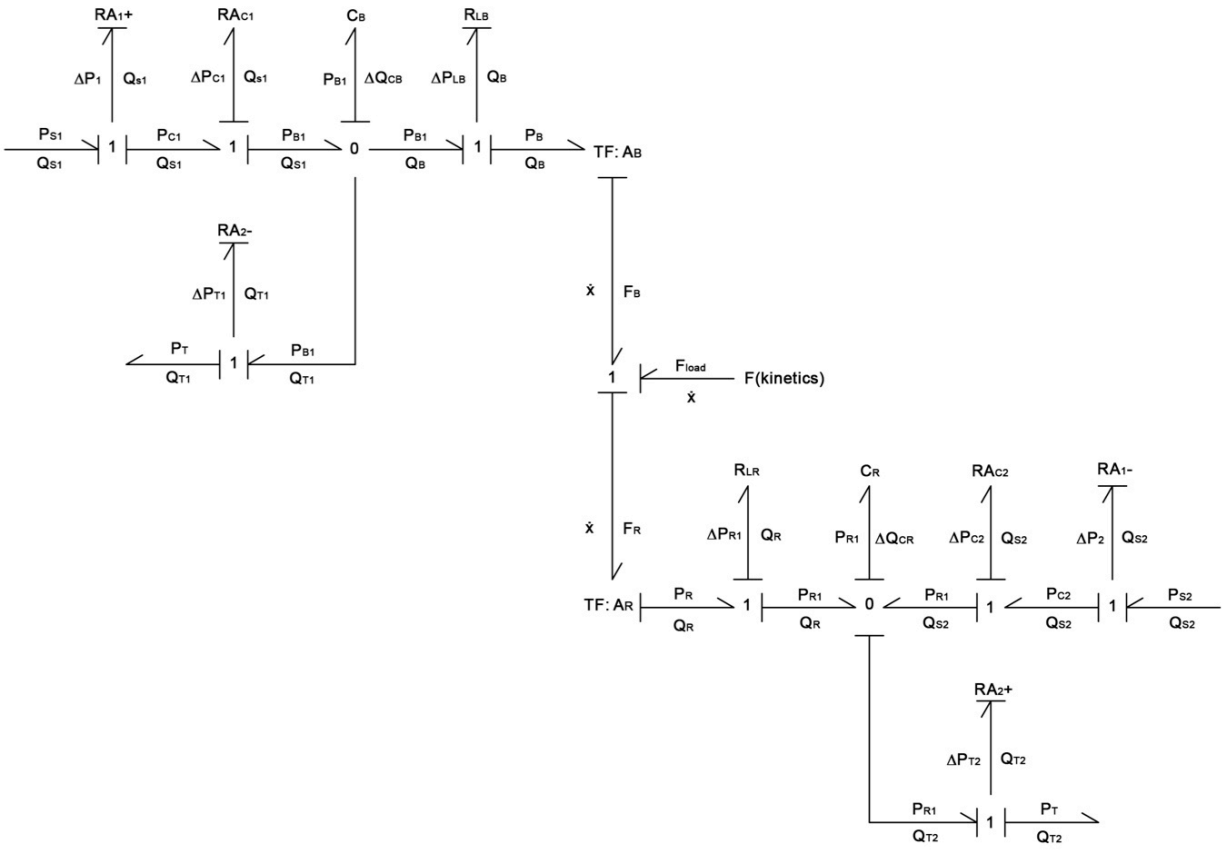

Figure 5.3 Power Bond Graph for the Simplified General Hydraulic Circuit

Using the PBG in Figure 5.3, a set of generalized equations can be developed in a methodical fashion, ensuring that the causality of the equations are appropriate. The following list shows the general equations developed from Figure 5.3 using the nomenclature specified at the beginning of the thesis:

$$\Delta P_1 = P_{S1} - P_{C1}, \quad [5.1]$$

$$Q_{S1} = (RA_{1+})\sqrt{\Delta P_1}, \quad [5.2]$$

$$P_{C1} = P_{B1} - \Delta P_{C1}, \quad [5.3]$$

$$\Delta P_{C1} = \frac{{Q_{S1}}^2}{{RA_{C1}}^2}, \quad [5.4]$$

$$\Delta Q_{CB} = Q_{S1} - Q_B - Q_{T1}, \quad [5.5]$$

$$P_{B1} = C_B \int \Delta Q_{CB} dt + P_{B1o}, \quad [5.6]$$

$$C_B = \frac{\beta}{V_B}, \quad [5.7]$$

$$\Delta P_{T1} = P_{B1} - P_T, \quad [5.8]$$

$$Q_{T1} = (RA_{2-})\sqrt{\Delta P_{T1}}, \quad [5.9]$$

$$\Delta P_{LB} = P_{B1} - P_B, \quad [5.10]$$

$$Q_B = \zeta \Delta P_{LB}, \text{ [9]} \quad [5.11]$$

$$\zeta = \frac{\pi D^4}{128 \mu L}, \quad [5.12]$$

$$P_B = \frac{F_B}{A_B}, \quad [5.13]$$

$$\dot{x} = \frac{Q_B}{A_B}, \quad [5.14]$$

$$F_B = F_R - F_{load}, \quad [5.15]$$

$$F_R = P_R A_R, \quad [5.16]$$

$$Q_R = \dot{x} A_R, \quad [5.17]$$

$$P_R = P_{R1} + \Delta P_{L1}, \quad [5.18]$$

$$\Delta P_{L1} = \frac{Q_R}{\zeta}, \text{ [9]} \quad [5.19]$$

$$\Delta Q_{CR} = Q_R - Q_{S2} - Q_{T2}, \quad [5.20]$$

$$P_{R1} = C_R \int \Delta Q_{CR} dt + P_{R1o}, \quad [5.21]$$

$$C_R = \frac{\beta}{V_R}, \quad [5.22]$$

$$\Delta P_{T2} = P_{R1} - P_T, \quad [5.23]$$

$$Q_{T2} = (RA_{2+})\sqrt{\Delta P_{T2}}, \quad [5.24]$$

$$P_{C2} = \Delta P_{C2} + P_{R1}, \quad [5.25]$$

$$\Delta P_{C2} = \frac{{Q_{S2}}^2}{{RA_{C2}}^2}, \quad [5.26]$$

$$\Delta P_2 = P_{S2} - P_{C2}, \text{ and} \quad [5.27]$$

$$Q_{S2} = (RA_{1-})\sqrt{\Delta P_2}. \quad [5.28]$$

In addition to the equations developed from the PBG, the system contains a number of check valves and pressure relief valves. As these components are contained within the main control valve block and direct measurements with the available instrumentation could not be completed, these components are not included in the hydraulic model of the JD 410G backhoe, with the exception of the bucket circuit, which will include a simple check valve model. The boom and stick circuits will not contain check or relief valve models, and care will be taken to ensure the

physical system is operated in such a way that these components will not be required. The check valve used in the bucket function model is placed on the blank side of the hydraulic actuator, and operates such that when the pressure drops below a certain point, fluid is added to the system to help raise the pressure and avoid cavitation. In general, for a check valve,

$$Q_{CV} = \begin{cases} R_{CV}\sqrt{P_{Line} - P_{Tank}}; when\ P_{Line} < P_{Tank} \\ 0; when\ P_{Line} > P_{Tank} \end{cases}, \quad [5.29]$$

where:

Q_{CV} = The flow rate of hydraulic fluid through the check valve $\left[\frac{m^3}{s}\right]$,

R_{CV} = The hydraulic resistance of the check valve $\left[\left(\frac{m^3}{s}\right)\Big/\sqrt{MPa}\right]$, and

P_{Line}, P_{Tank} = The line and tank pressures $[MPa]$.

As mentioned, the location of the check valve on the JD 410G backhoe and the available instrumentation did not allow for experimental measurements to be used to determine the pressure-flow relationship of the check valve; rather, a simple orifice equation is used to approximate the check valve behavior, as shown in Equation 5.29. The hydraulic resistance of the check valve is selected as $R_{CV} = 2\text{x}10^{-7}\left[\left(\frac{m^3}{s}\right)\Big/\sqrt{MPa}\right]$. Any flow through the check valve is passed through a first order filter having $\tau = 0.02$s, to ensure a continuous and smooth signal.

The pump supply pressure is simulated by adding a margin pressure to the load pressure of each circuit, such that

$$P_s = \begin{cases} P_L + P_{margin}\ ; when\ x_{spool} \neq 0 \\ P_T; when\ x_{spool} = 0 \end{cases}. \quad [5.30]$$

This relationship ensures the fluid being supplied to the circuit will be at a higher pressure than the load. To create a time delay and maintain continuity, the supply pressure, P_s, is passed through a first order filter having $\tau = 0.1$s. This value for τ is selected to approximate the time it

takes for the swash plate of the pump to adjust positions, and essentially provides a crude model of the pump and sensing feedback lines.

5.3 Control Valve Characteristic Curves

The operator of the system uses two control levers to actuate the three functions of the JD 410G backhoe workgroup being modeled in this thesis. When the operator moves the control levers, the lever motion is directly coupled to the linear motion of three spools, each controlling a single hydraulic function. As these spools move away from the center (closed position) they allow hydraulic fluid to pass through a number of ports, allowing supply flow to be routed to the desired location and return flow to pass through the valve to the reservoir. The rate at which the fluid is allowed to flow through the valve is proportional to the amount the spool is displaced from the center position and the pressure differential across the openings. The general equation for flow across an orifice is

$$Q = RA\sqrt{\Delta P}, \qquad [5.31]$$

where:

Q = The volumetric flow rate of hydraulic fluid through the orifice $\left[\frac{m^3}{s}\right]$,

RA = The lumped hydraulic resistance of the orifice $\left[\left(\frac{m^3}{s}\right)\Big/\sqrt{MPa}\right]$, and

ΔP = The pressure drop across the orifice $[MPa]$.

In the case of a proportional control valve, the operator has direct control of the value of the lumped hydraulic resistance; as the spool displacement is increased from the center position, the resistance will decrease, allowing hydraulic fluid to pass through the valve easier than for small displacements. Each of the three spools considered on the JD 410G contains two orifices that are used to meter the flow; namely, the meter-in orifice (controls the flow being delivered from the pump to the load) and the meter-out orifice (controls the flow returning from the load to the reservoir). By dividing the hydraulic circuit into four flow paths, as shown in Figure 5.1 and Figure 5.2, each path will include a lumped hydraulic resistance curve for either a positive or negative spool displacement.

The relationship between the spool displacement and lumped hydraulic resistance was determined using experimental methods. Pressure transducers were used to measure the pressure at both ports on a given actuator, as well as the pump supply pressure and the reservoir pressure. These four pressure signals are used to find the ΔP term of Equation 5.31. The volumetric flow rate through the orifice was indirectly measured by placing a string potentiometer along the hydraulic actuator. The string potentiometer measured the length, L, of the actuator, which can be converted into actuator velocity, V, by

$$V = \frac{\Delta L}{\Delta t}, \quad [5.32]$$

and can further be converted into the volumetric flow rate, Q, by

$$Q = V \cdot A_{B,R}, \quad [5.33]$$

where:

$A_{B,R}$ = The cross-sectional area of the blank (B) or rod (R) side of the actuator $[m^2]$.

For a set of measurements at a fixed spool displacement, the lumped hydraulic resistance is calculated by rearranging Equation 5.31, such that

$$RA = \frac{Q}{\sqrt{\Delta P}}. \quad [5.34]$$

Collection of data over a complete range of spool positions allows the lumped hydraulic resistance to be plotted with the spool position, which can then be used in the hydraulic model to relate the inputted spool position to the matching lumped hydraulic resistance. Figure 5.4-Figure 5.9 show the lumped hydraulic resistance curves for each of the three functions, as well as the polynomial curve fitted to the data to be used in the simulation model.

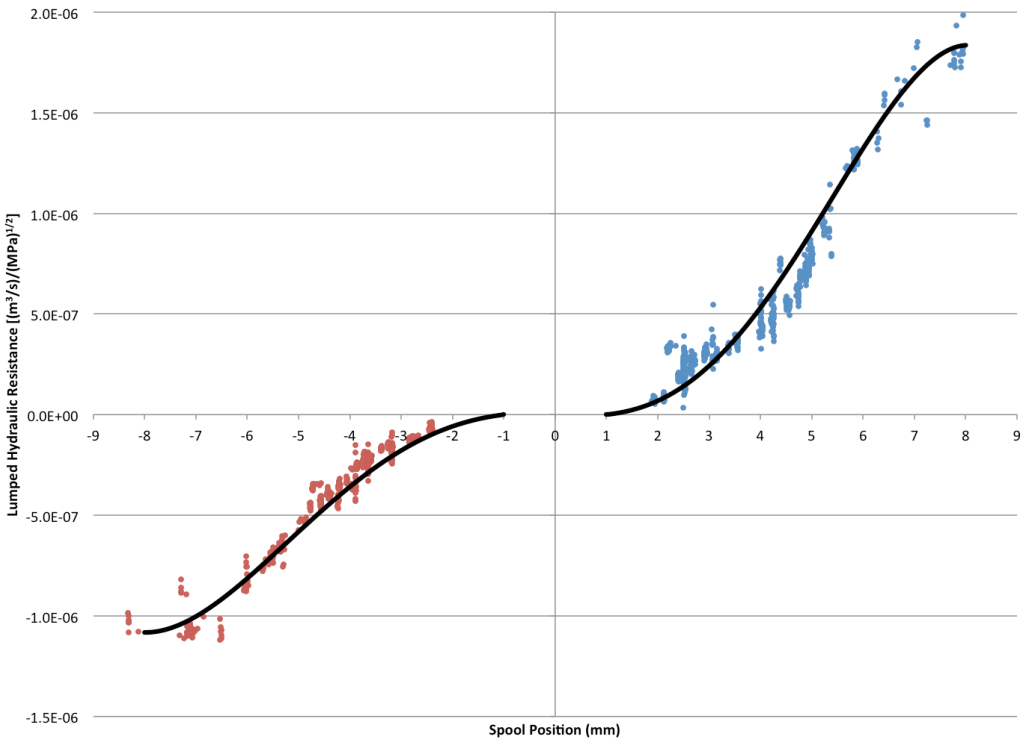

Figure 5.4 Control Valve Characteristic Curve for the Boom Supply Orifice

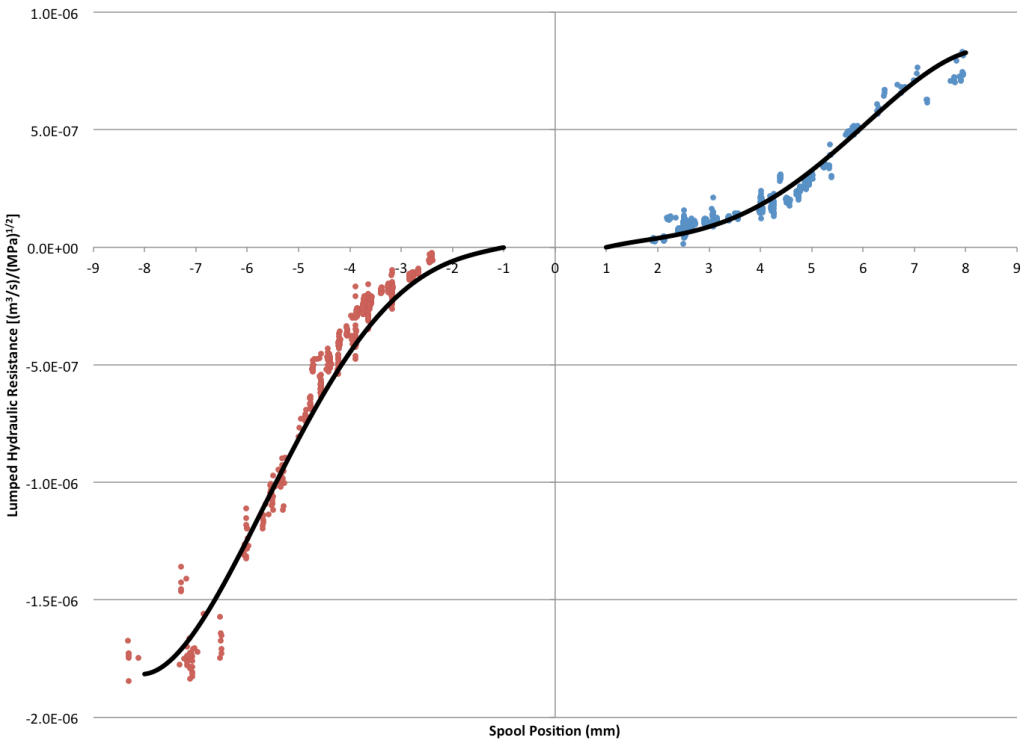

Figure 5.5 Control Valve Characteristic Curve for the Boom Return Orifice

The curves presented in Figure 5.4 and Figure 5.5 apply to the control valve for the boom function of the workgroup. Each plot contains a set of experimentally measured results (shown as individual points), and two polynomial curves fitted to the data. One polynomial curve represents the lumped hydraulic resistance for positive spool positions, while the other is for negative spool positions. Note that the polynomial curves start at a spool displacement of ± 1 mm, and do not contain any data between these values. This area of represents the *overlap region* of the closed center valves [9], and it must be noted that the 1mm of spool overlap is an assumed value, as measurements at very small spool displacements could not be reliably obtained. The actual overlap for the valves could be obtained by manufacturer specifications or CAD drawings of the valve; neither of which was available to the author.

Figure 5.6 and Figure 5.7 have been generated for the stick function of the backhoe loader, and are shown below.

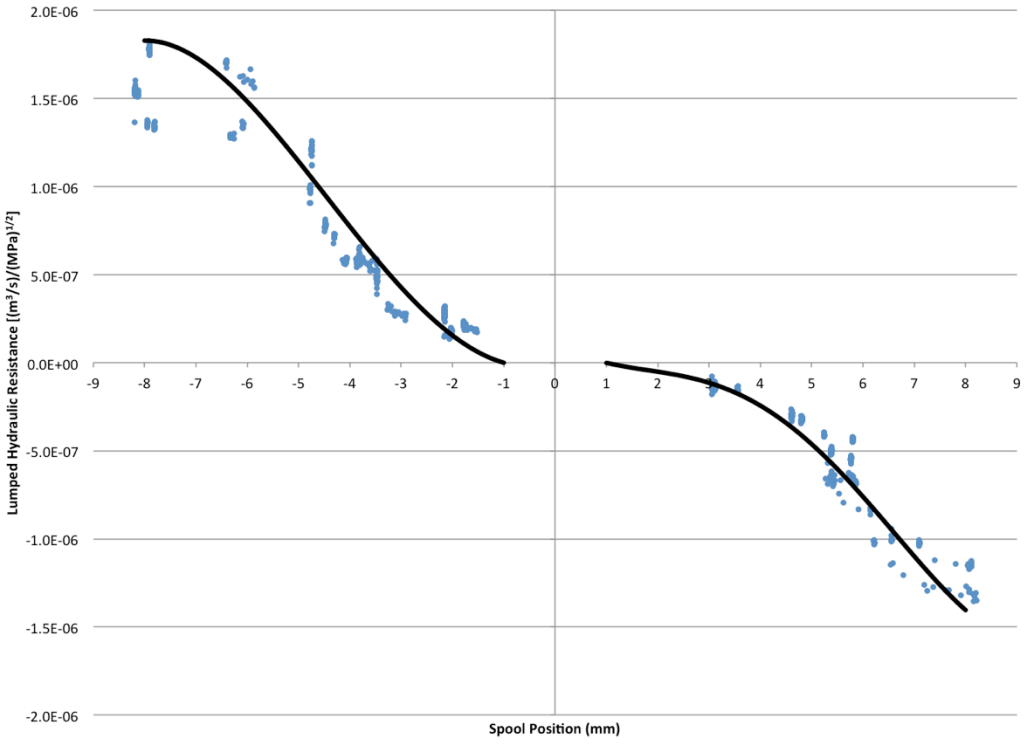

Figure 5.6 Control Valve Characteristic Curve for the Stick Supply Orifice

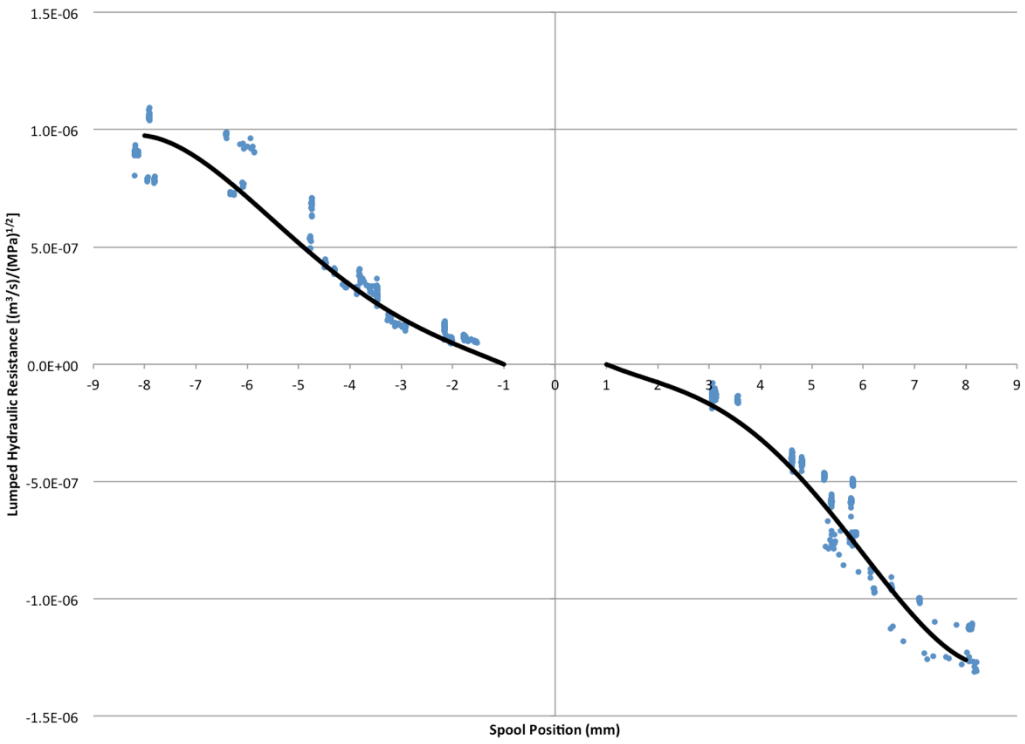

Figure 5.7 Control Valve Characteristic Curve for the Stick Return Orifice

It can be observed that the shape of the curves in Figure 5.6 and Figure 5.7 are not the same as for the boom function, as a positive spool displacement for the stick results in a negative lumped hydraulic resistance. This simply means that for the stick function, a positive spool displacement results in a retraction, or shortening of the stick cylinder, compared to the boom, which extends when subjected to a positive spool displacement.

The final control valve characteristic curves are presented in Figure 5.8 and Figure 5.9, and they apply to the bucket function of the backhoe workgroup. In processing the collected data for the bucket function, it was observed that the pump supply pressure was considerably higher than the measured load pressure when compared to the data collected for the boom and stick functions. This suggests that when the bucket function was operated alone during testing, that it was not the highest sensed pressure in the system. As a consequence, the curves presented for the bucket supply control orifice are not expected to be an accurate representation of the real system behavior. Further discussion will be presented in the next section.

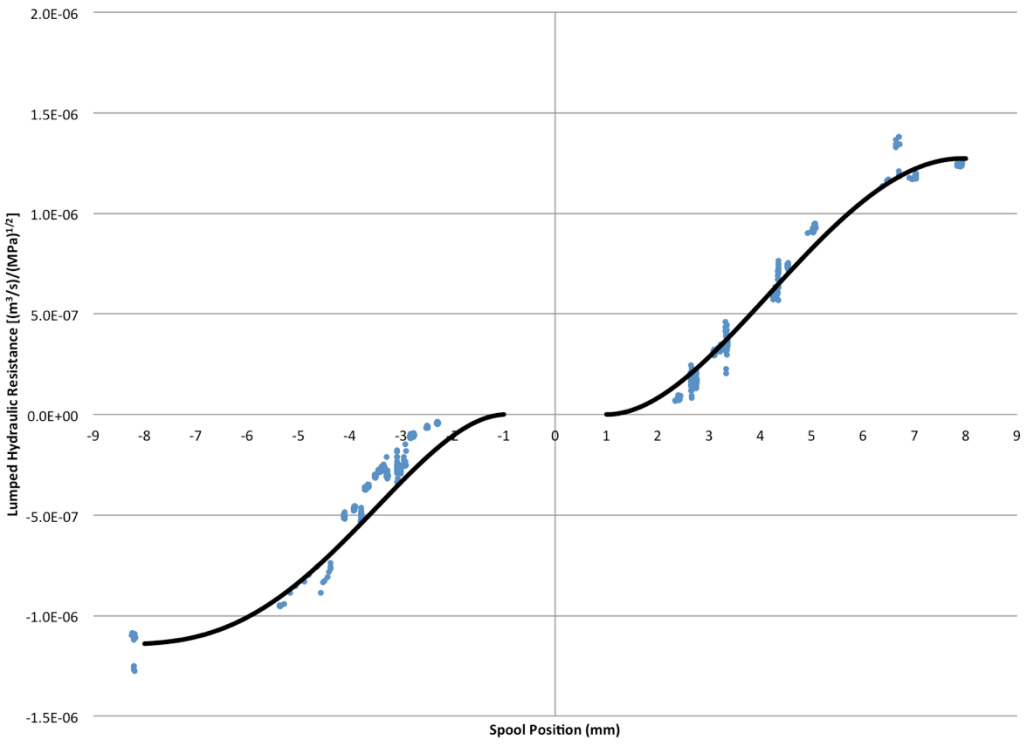

Figure 5.8 Control Valve Characteristic Curve for the Bucket Supply Orifice

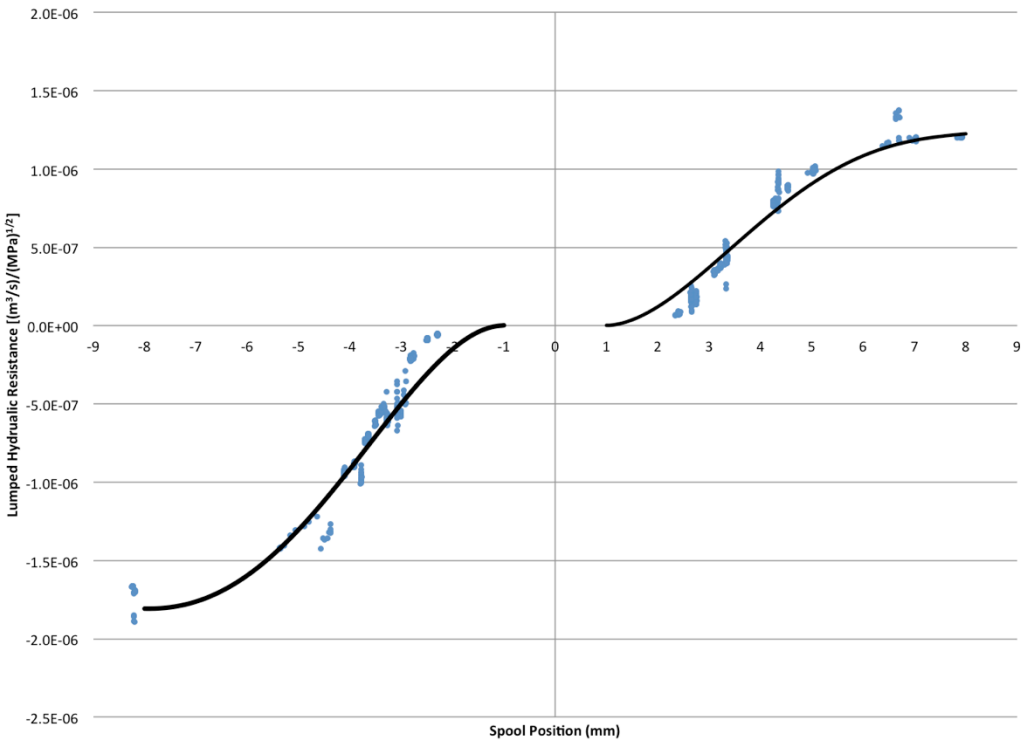

Figure 5.9 Control Valve Characteristic Curve for the Bucket Return Orifice

The polynomial curves fitted to the measured data were of the fourth order, having the form

$$RA = Ax_{spool}^4 + Bx_{spool}^3 + Cx_{spool}^2 + Dx_{spool}. \quad [5.35]$$

Each curve was fitted to spool positions between 1 mm and 8 mm for positive displacements, or between -1 mm and -8 mm for negative spool displacements. It can be observed from the previous figures that there is a wide spread of measured lumped hydraulic resistance values at a given spool displacement and consequently, this will undoubtedly lead to uncertainty in the fitted curve. As an example, consider Figure 5.10, which shows the positive spool displacement subset of Figure 5.4. The envelope of experimentally determined resistance values has been shown, and four locations are selected to demonstrate the potential spread in the data.

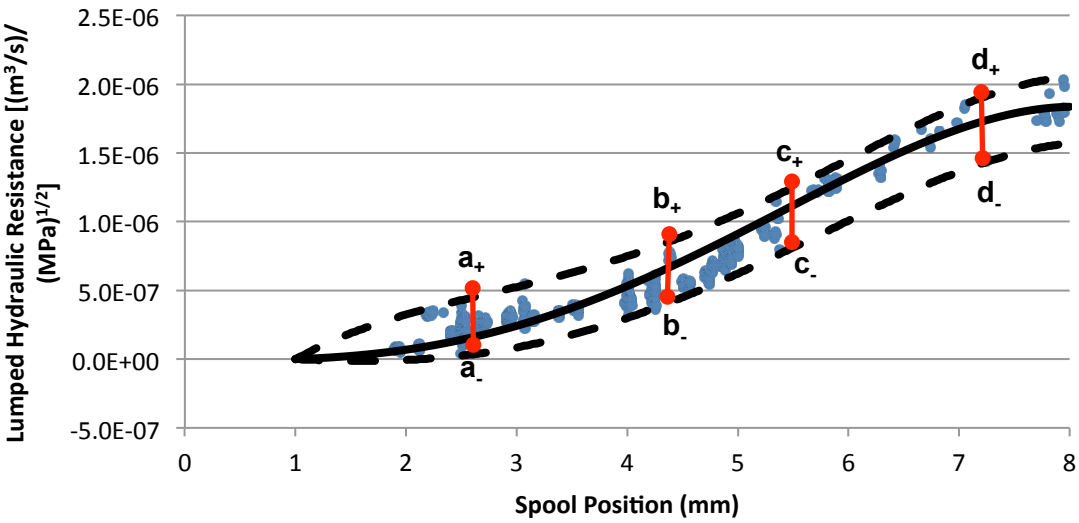

Figure 5.10 Boom Supply Valve Orifice Characteristic Curve for Positive Spool Openings

Table 5.1 shows the values of the lumped hydraulic resistance calculated at both the envelope point locations, and the curve fitted location for a common spool position. The purpose of this table is to show the wide range of possible values the curve fitted to the measured data could encompass.

Table 5.1 Hydraulic Resistances at the Fitted Curve and Data Envelope Locations

Point	Spool Position (mm)	Resistance at Envelope Point [$(m^3/s)/(MPa)^{1/2}$]	Curve Fit Resistance [$(m^3/s)/(MPa)^{1/2}$]	Separation (%)
a_+	2.5	2.672E-07	1.410E-07	**-89.5**
a_-	2.5	2.499E-08	1.410E-07	**82.3**
b_+	4.25	8.125E-07	6.197E-07	**-31.1**
b_-	4.25	3.714E-07	6.197E-07	**40.1**
c_+	5.4	1.204E-06	1.077E-06	**-11.8**
c_-	5.4	7.730E-07	1.077E-06	**28.2**
d_+	7.2	1.890E-06	1.726E-06	**-9.5**
d_-	7.2	1.419E-06	1.726E-06	**17.8**

To compensate for spread in measured lumped hydraulic resistances, the polynomial curves of each of the three functions must be tuned to ensure the simulation model produces acceptable results at a given operating point. The polynomial curves act as a starting place from which the tuning would begin, and the tuning process is such that it is ensured that the adjusted curves are still maintained within the envelope of experimental results.

5.4 Limitations of the Hydraulic Model

Due to a number of factors, some parts of the hydraulic system of the JD 410G backhoe loader could not be modeled at this point. This section will discuss these omissions, and if appropriate, the cause of the omission and their effect on the hydraulic model operation.

5.4.1 Load-Sensing Pump Modeling

As previously mentioned, the load-sensing pump present on the JD 410G was not modeled in this thesis. This was primarily due to a lack of available information and access to measure the pump characteristics. There does exists a large body of research focused on the modeling of

pumps, and with the appropriate specifications of the JD 410G hydraulics, a model could be generated without requiring any original research. This is an area of future study.

The pump in this model has been roughly approximated by the methods discussed in Section 5.2, and it is expected that omission of a proper pump model will result in errors in the dynamics of the hydraulic model developed in this chapter.

5.4.2 Pressure Compensator Modeling

Each of the three hydraulic functions modeled in this thesis contain a pressure compensator within the control valve. For a load-sensing system, the function of these compensators is to maintain a constant pressure drop across the supply orifice of the control valve. To do this, the pressure compensator is exposed to the pump supply pressure, the function load pressure, and the highest-sensed load pressure (shown as LS Max in Figures 5.1 and 5.2). Using these three pressures, the pressure compensator can apply a pressure drop to the supply flow to the circuit in order to maintain a constant flow delivery to the load for a specific spool displacement.

Due to the location of the pressure compensator (internal to the control valve), and the available measurement equipment, the pressure compensator model could not be included in the hydraulic modeling. The equations presented in Section 5.2 allow for a compensator model to be easily added to the hydraulic model if the necessary information becomes available, but this could not be done at this point. The effect of this is that each circuit will not be able to function properly with a single pump supplying fluid at a pressure slightly higher than the highest sensed load in the system. To overcome this in the hydraulic model presented in this chapter, each circuit is treated as having its own hydraulic pump that is set to match the load requirements of that circuit only.

5.4.3 Hydraulic Cylinder End-stops

When a hydraulic cylinder reaches the beginning or end of its stroke, it can come to an abrupt stop when the piston contacts the end caps of the hydraulic cylinder. This stop happens in a very short period of time, causing a large deceleration (a hard stop) of the load. Modeling this

presents some challenges, as a large deceleration acting over a very short period of time can lead to discontinuities within the model signals.

One possibility is to simulate these hard stops by implementing a non-linear spring at the cylinder ends to ensure the load comes to a smooth, but fast stop when reaching the limits of its stroke. Preliminary studies suggested that this would lead to problems with the load pressures of the circuit at these points, and as such the ends have not been included in this model. To account for this, care was taken to ensure the load did not travel past the physical stroke limits. This was achieved by closing the control valve orifices before the piston reached the ends of its stroke.

5.4.4 Causality of the Cylinder Force Equations

The PBG approach to determining the causality of the equations ensures that all equations are in a form that the power flows through the system can be readily determined; it does not ensure the equations are accurately expressing the system to be modeled. In developing the kinematic and kinetic equations, the standard modeling approach dictated that velocity was the input and the required force to achieve that velocity was the output. This differs from hydraulic modeling, where the velocity is a consequence of the applied force. To compensate for this, the causality of the hydraulic model was adjusted to accommodate the cylinder velocity as an input, and as such, the model changed to one of a line capacitance followed by a line resistance configuration (see Figure 5.3) for a cylinder extension, for example. This could be problematic except for the fact that the capacitance of the line is larger than that of the hydraulic cylinder (by a factor between about 2 and 4) due to the reduced effective bulk modulus of the flexible line and fluid. Thus, this configuration was considered to be satisfactory for the simulation study.

5.5 Order of Calculations for Cylinder Extension and Retraction

The PBG in Figure 5.3 was developed using a two-step process. In the first step, the power bonds apply only to a hydraulic cylinder that can move in one direction (in this case, cylinder extension). When the cylinder is moving in the forward direction, the power bond graph dictates that the order of calculations concerning only the motion of the actuator will be as follows:

1. The supply pressure is calculated from Equation 5.30.
2. Blankside line pressure is calculated from Equation 5.6.
3. The cylinder blankside pressure is calculated from Equation 5.13.
4. The flow into the cylinder and its resulting velocity are calculated from Equations 5.11 and 5.14, respectively.
5. The cylinder blankside force is calculated from Equation 5.15.
6. The cylinder rodside force is calculated from Equation 5.16.
7. The cylinder rodside pressure is calculated from Equation 5.21.
8. The tank flow leaving the cylinder is calculated from Equation 5.9.

The order in which the calculations are carried out in the extension direction of the hydraulic actuator are expected to predict pressures and flows that are similar to values that could be measured from the physical system.

The second step in the power bond graph development added in additional power bonds to allow the hydraulic actuator to travel in the opposite direction (cylinder retraction). This was achieved by introducing additional bonds to the existing framework developed for the extension direction. The order of calculations concerning only the actuator motion will be as follows:

1. The supply pressure is calculated from Equation 5.30.
2. The blankside line pressure is calculated from Equation 5.6.
3. The cylinder blankside pressure is calculated from Equation 5.13.
4. The flow out of the cylinder and resulting velocity are calculated from Equations 5.11 and 5.14.
5. The cylinder blankside force is calculated from Equation 5.15.
6. The cylinder rodside force is calculated from Equation 5.16.
7. The cylinder rodside pressure is calculated from Equation 5.21.
8. The supply flow into the cylinder is calculated from Equation 5.28.

The order in which the calculations are carried out for the retraction direction of motion are such that a disconnect exists between the cylinder supply flow and the determination of the cylinder

velocity. The supply flow into the actuator is determined by the pressure difference across the control orifice, which is one of the last calculations carried out by the model. The cylinder velocity is calculated from the flow and pressures exiting the circuit; the pressures and flows of the fluid exiting the cylinder are a function of the pressures and flows entering the cylinder, but in this case they are being calculated first. This disconnect is expected to adversely affect the predicted results from the simulation model when compared to recorded parameters from the physical system, and these effects will be examined in Chapter 6.

Further investigation is required to completely understand this behavior, although an initial step to understanding this problem would be to develop a second simulation model that is based on the retraction direction, and has the equations for extension added in after the initial power bond graph is developed. The results produced from both simulations should be compared to understand fully the consequences of the aforementioned order of equations concerns.

5.6 Model Implementation

The general equations presented in this chapter have been used to develop the hydraulic model for each of the three functions of the JD 410G backhoe workgroup. The three functions have been assembled using the object-oriented environment available in MATLAB's Simulink modeling package. The hydraulic model has been connected to the kinematic and kinetic models developed in previous chapters. In the next chapter, the operation of the model will be investigated and the outputs will be compared to measurements recorded from the JD 410G backhoe. Emphasis will be placed on the steady state conditions since the transient knowledge of the pump and valve was not well established.

Chapter 6: Presentation and Discussion of Results

6.1 Chapter Objectives

Completion and implementation of the hydraulic model is the final step in assembling a computer simulation of the JD 410G backhoe workgroup. The objective of this chapter is to provide a comparison between data collected from the real system and data generated by the computer model. It has already been discussed that the dynamics of the system cannot be modeled without a load-sensing pump, and pressure compensator models, so focus will be directed to the steady-state operation of the system. In this chapter, steady-state conditions are considered to exist when both the control valve spool positions are not changing by a significant amount, and the system operating pressures are not undergoing any significant changes; under these conditions, the dynamics of the system do not dominate the results.

As a result of the limited quantity of instrumentation available, data could only be recorded on a single function operating at any given time; therefore, comparisons have been made by considering the operation of one function at a time. Given that the pressure compensators for each circuit have not been modeled, this approach is appropriate and will avoid the need to consider any flow sharing between circuits. It should be mentioned that the completed model is capable of operating multiple functions at once, but this motion will not be considered in this discussion.

6.2 Experimental Methods

6.2.1 Experimental Procedure

The three functions of the backhoe workgroup were all subjected to the same procedure to collect experimental data to be compared to the simulation-predicted outputs. Starting from the *home position*, the following procedure was followed:

1. Start logging data using the computer.
2. Move the control lever from the center position, and hold at a fixed position as the actuator retracts or extends.

3. As the actuator approaches the end of its stroke, move the control lever back to the center position, stopping the motion.
4. Allow any oscillatory motion experienced to damp out.
5. Move the control lever from the center position in the opposite direction, and hold at a fixed position as the actuator returns towards the *home position*.
6. When the actuator approaches the initial *home position*, move the control lever back to the center position before contact with the end cap of the cylinder is made.
7. Stop logging data after the system has come to rest.

Figure 6.1 shows the home position (step 2 and 6) and stopping position (step 3) for the motion of each of the three actuators.

Figure 6.1 Stopping Positions for the Experimental Procedure

6.2.2 Method of Data Collection

Each of the three modeled functions of the JD 410G backhoe workgroup were instrumented in such a way as to record the following parameters: control valve spool displacement (using a linear potentiometer), actuator position (using a string potentiometer), and the pressures on both sides of the hydraulic actuator (using two pressure transducers). All transducers were calibrated using standard calibration methods. The procedures and calibration curves are summarized in Appendix E. All of the instrumentation was connected to a computer by means of a DAQ device, and LABView software was used to log the data.

Using the measured parameters, plots showing spool position, actuator position, actuator velocity, blankside actuator pressure, and rodside actuator pressure as a function of time were created. These five plots for each set of measured data will be used as a basis of comparison between the real system and the simulation results.

6.2.3 Generation of Simulation Results

The simulation results were obtained by using the experimentally obtained spool positions as inputs to the model. For each of the three functions, the pump margin pressure and tank pressures were set to a fixed value, which were constant for all three functions. Due to the previously discussed scatter of data used to generate the control valve lumped hydraulic resistance curves, and any differences between the real system's tank and margin pressures and those of the simulation, it was necessary to *tune* the system by means of scaling the magnitudes of the lumped hydraulic resistance curves. The scaling factors applied to the curves were determined through a process of incremental improvements. Starting with the fitted curves presented in the previous chapter, small adjustments were made until the output signals (under steady-state conditions) began to converge to the experimental results.

The polynomial curve for each control orifice presented in Chapter 5 consists of two curves: one for positive spool displacements and one for negative displacements. Each of these curves was scaled independently of the other. As such, for a given function control valve, there are four possible scaling factors available to *tune* the simulation results (two scaling factors for the supply orifice, and two for the return orifice). In total, 12 scaling factors were used to tune the complete backhoe model.

6.2.4 Kinetic Correction Factor

Early indications during simulations runs for the purpose of *tuning* the model suggested that the forces being calculated by the kinetic relationships developed in Chapter 4 contained a significant separation from the real system. This was observed in the cylinder pressures while the system was operating as an overrunning (assistive) load; the pressure differential across the hydraulic actuator did not appear to be correct. To investigate this, a series of static measurements were taken from the real system to indirectly measure the forces acting on each actuator throughout their stroke.

An analog pressure gage was installed on the high-pressure side of each of the three actuators one function at a time. Each actuator was oriented in such a way that gravity was the only driving force in the system. Each cylinder was moved incrementally throughout its stroke, and the pressure (due only to gravity) and cylinder length were recorded. Using the actuator area and the measured pressure, the force contained along the actuator linkage could be calculated and directly compared to the output from the kinetic sub-model.

Figure 6.2 shows the measured force on the boom cylinder and the kinetic sub-model predicted force. It can be seen that the measured load force is higher than the simulated load force by a constant amount. The separation is due to the assumption that the hydraulic cylinders have negligible mass; in reality, the mass of these parts is significant, as can be seen in Figure 6.2. The dashed line in Figure 6.2 is a linearly scaled set of simulated results; multiplying the original simulation results by exactly 5/3 results in a near-perfect match. The high agreement between the shape of the curves suggest that the estimated location of the center of gravity is very close as well.

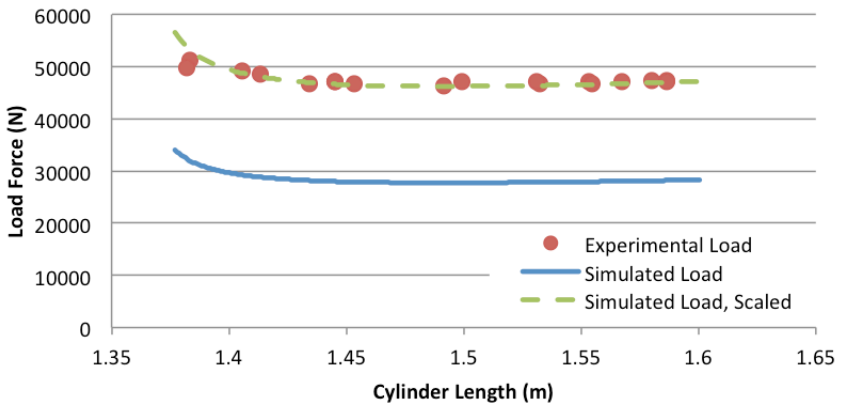

Figure 6.2 Experimental and Simulated Boom Cylinder Loading

A similar trend is observed in the stick cylinder, shown in Figure 6.3. By scaling the simulated forces by 3/2, the simulated load and measured loads come very close to each other. In the case of the stick cylinder, it can be seen that the trend of the simulated data is not as close as it was for the boom cylinder, suggesting that the center of gravity location could still be an issue.

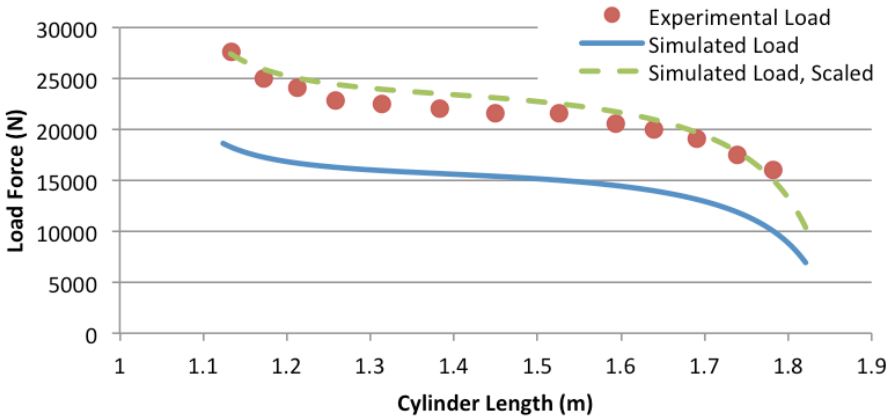

Figure 6.3 Experimental and Simulated Stick Cylinder Loading

Lastly, the results from the bucket cylinder loading are shown in Figure 6.4. The bucket force curves do not require any scaling to get a match between the experimental and simulated data, as the mass of the bucket is not affected by the negligible cylinder mass assumption as much as the other two functions; however, it can be observed that the shapes of the two curves do not exactly match for negative load forces. This again suggests that the location of the estimated center of gravity needs to be addressed in future studies.

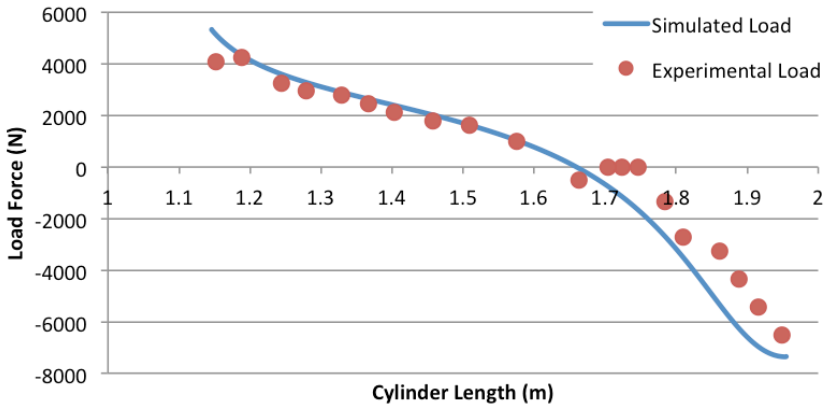

Figure 6.4 Experimental and Simulated Bucket Cylinder Loading

Using the two mentioned correction factors for the boom and stick kinetic sub-modeling, the forces predicted by the simulation model were adjusted to more accurately represent the real system, and the *tuning* process was continued.

6.2.5 Simulation Model *Tuning* Factors

Table 6.1 contains the twelve *tuning factors* determined from the iterative process for the complete simulation model. The tuning factors not only account for any uncertainty in the process used to develop the polynomial curves that represent the lumped hydraulic resistance of the control orifices for each circuit, but also compensate for any differences between the supply and return pressures of both systems. A complete valve and pump model should address this issue, and is an issue that should be considered in future work.

The scaling factors presented in Table 6.1 are specific to the operating points selected as the control valve inputs to the model, and are expected to be valid for small deviations from these operating points. It should also be mentioned that the tuning factors presented in Table 6.1 are selected to ensure that the polynomial curves presented in Chapter 5 for the control valves still fall within the envelope of experimental results.

Table 6.1 Scaling Factors used to Tune the Backhoe Model

Boom Control Valve		**Scaling Factor**
Supply	$x_{spool} > 0$	0.9
Supply	$x_{spool} < 0$	0.75
Return	$x_{spool} > 0$	0.85
Return	$x_{spool} < 0$	1.5
Stick Control Valve		
Supply	$x_{spool} > 0$	1
Supply	$x_{spool} < 0$	0.9
Return	$x_{spool} > 0$	0.9
Return	$x_{spool} < 0$	1.2
Bucket Control Valve		
Supply	$x_{spool} > 0$	0.7
Supply	$x_{spool} < 0$	0.5
Return	$x_{spool} > 0$	1.5
Return	$x_{spool} < 0$	1.7

6.2.6 Experimental Data to be used in the Comparison

This section will present a complete set of data used to compare the simulation results to the physical system. A set of data recorded from the bucket function has been selected as an example. Figure 6.5-Figure 6.9 show a complete set of data recorded from the bucket function of the JD 410G backhoe. Each plot has been labeled with four points in alphabetical order, from A-D. These points are used to define the region of steady-state operation of the system. In Figure 6.5-Figure 6.9, the region between points 'A' and 'B' is the steady state operation of the system moving away from the *home position*, retracting the bucket cylinder (see Figure 6.1, moving from left to right). Similarly, the region between points 'C' and 'D' is the steady state operation of the system in the opposite direction.

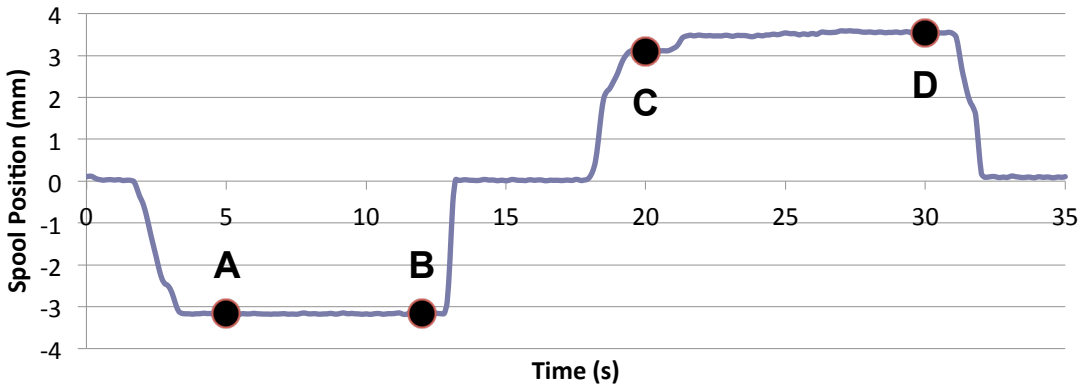

Figure 6.5 Sample Measured Bucket Control Valve Spool Displacement

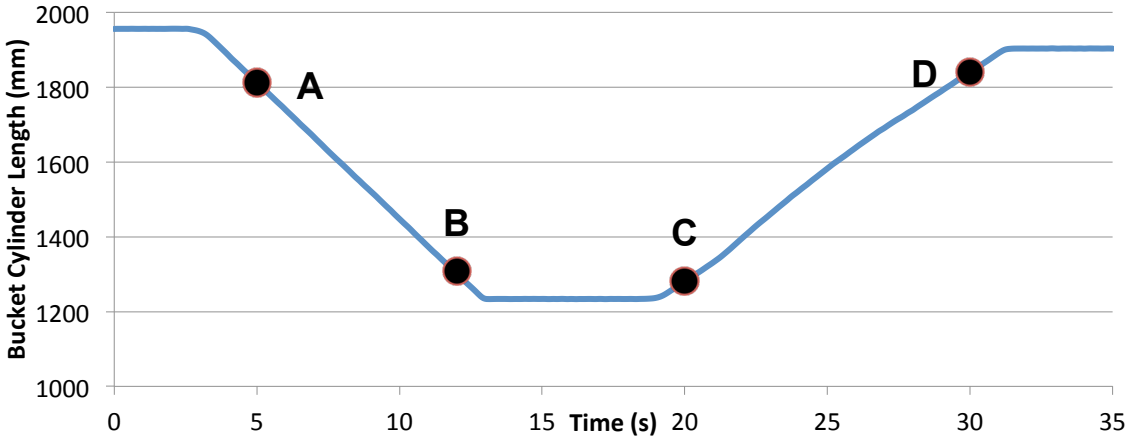

Figure 6.6 Sample Measured Bucket Cylinder Length

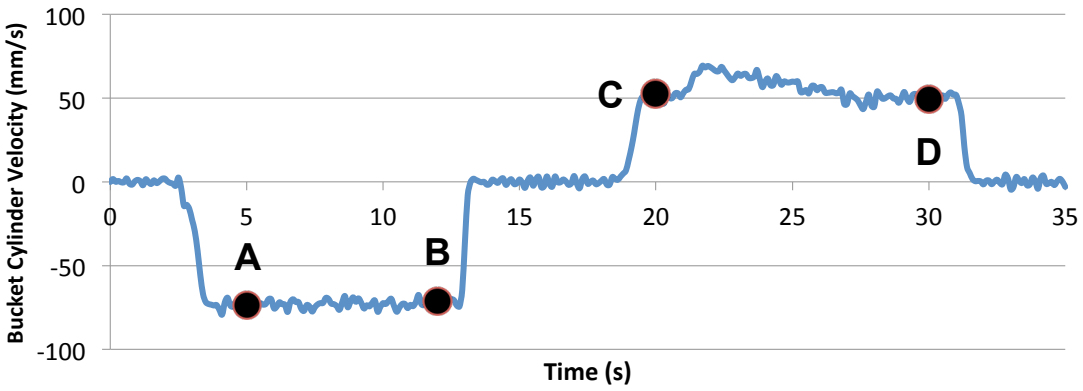

Figure 6.7 Sample Measured Bucket Cylinder Velocity

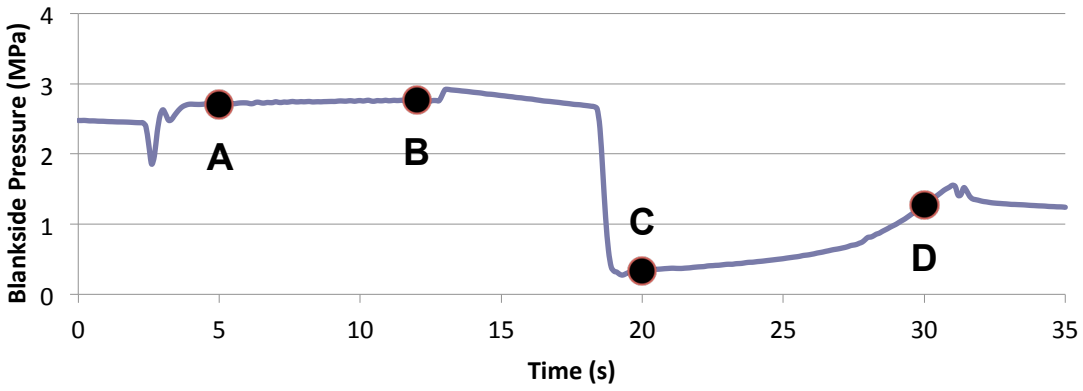

Figure 6.8 Sample Measured Pressure on the Blankside of the Bucket Actuator

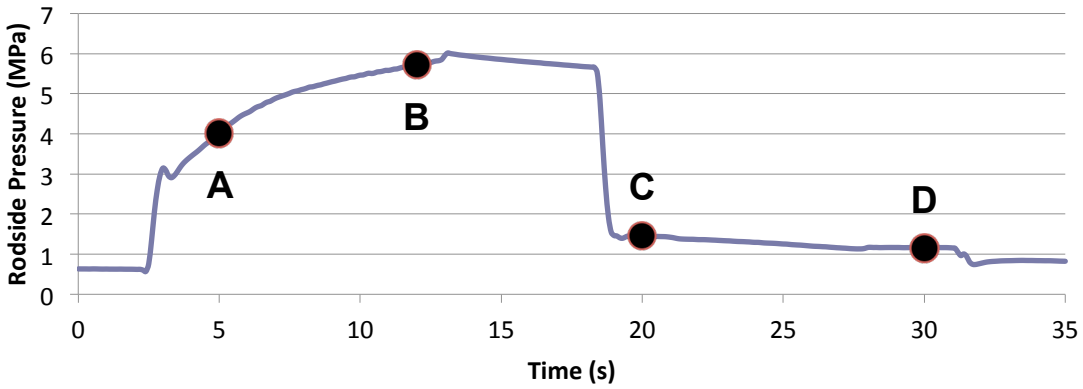

Figure 6.9 Sample Measured Pressure on the Rodside of the Bucket Actuator

The data presented in Figure 6.5-Figure 6.9 demonstrates a typical set of data measured from the JD 410G backhoe loader. As discussed, simulated results presented will focus mainly on the steady state operation of the system. The results for the spool position, cylinder length, and cylinder velocity will be presented for the entire set of experimental data; the results for the rodside and blankside pressures will be presented only for the steady state operation of the system.

6.3 Presentation and Discussion of Results

The results presented in this section will be in graphical format, facilitating a simple visual comparison between the measured and simulated results. In all of the following plots, the measured data will be shown as a solid line, while the simulated results will be represented using a dotted line. For the testing of the boom and stick functions, two sets of data will be presented;

the first set of data will be that which was used to determine the *tuning factors* for the model, while the second set of data uses these tuning factors at a different operating point to investigate the validity of the model at a different operating point from the *tuning factors*. Only a single set of data will be shown for the bucket function, as the valve characteristic curves require further work to achieve an accurate representation of the real system.

6.3.1 Boom Function Results

The following set of results are for the motion of the boom cylinder, as was illustrated in the top of Figure 6.1. Figure 6.10 shows the measured and simulated control valve spool displacements used to control the boom cylinder for this set of measurements.

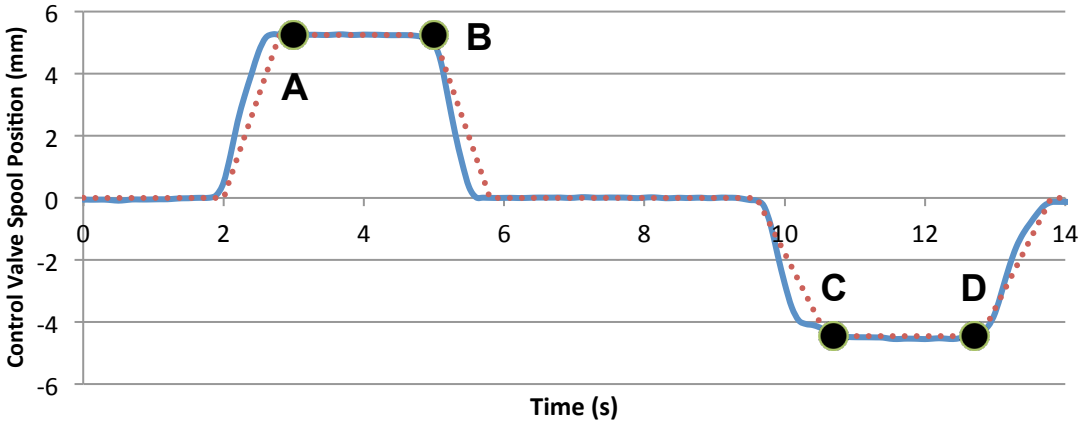

Figure 6.10 Boom Function Control Valve Spool Displacement Inputs for Data Set 1 (Solid line: experimental, dotted line: simulation)

Figure 6.11 shows the position of the boom cylinder, and it must be noted that for the boom cylinder function, due to spatial constraints, the boom cylinder was only allowed to travel through about 30% of its complete stroke before the workgroup would contact the ground.

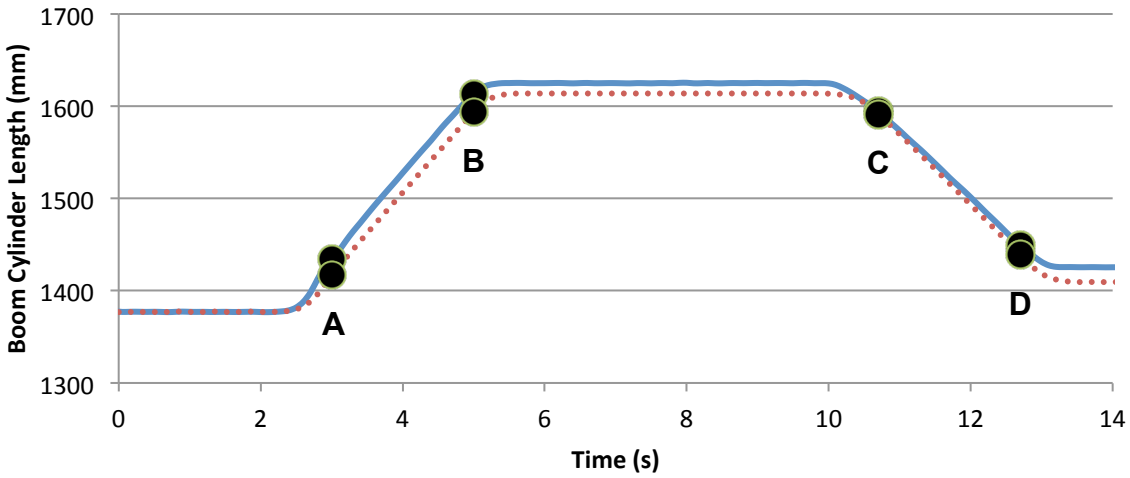

Figure 6.11 Boom Cylinder Length for Data Set 1
(Solid line: experimental, dotted line: simulation)

The boom cylinder velocity is determined by taking the first derivative of measured data from Figure 6.11, and is shown below in Figure 6.12. It can be seen that the velocity of the simulated system appears to be smoother than the real system, although the apparent oscillations between 6 and 10 seconds suggest that the measured signal may have some noise present, as during data collection, it was observed that the system would typically damp out all oscillatory motion within two seconds of closing the control valve.

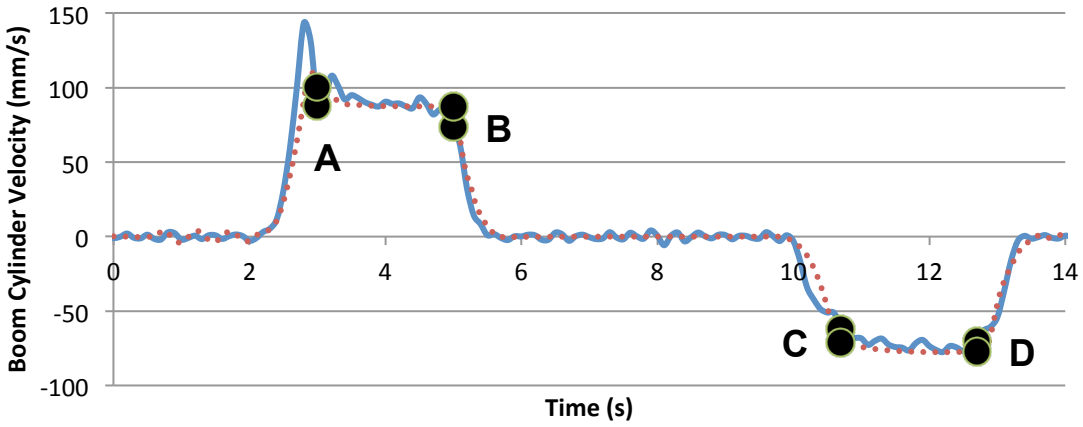

Figure 6.12 Boom Cylinder Velocity for Data Set 1
(Solid line: experimental, dotted line: simulation)

For the steady-state operation during extension of the system, the blankside and rodside pressures are presented in Figure 6.13 and Figure 6.14. As the boom cylinder is extending, the

simulated and measured data for both figures agree in both magnitude and trend of the curve. The blankside pressure is slightly lower than the actual measured pressure; this could be remedied by further adjustment of the *tuning factors* applied to the control valve characteristic curves. The key observation from the figures below is that the trend of the data is the same; that is, both curves follow the same pattern during steady-state operation between 'A' and 'B.'

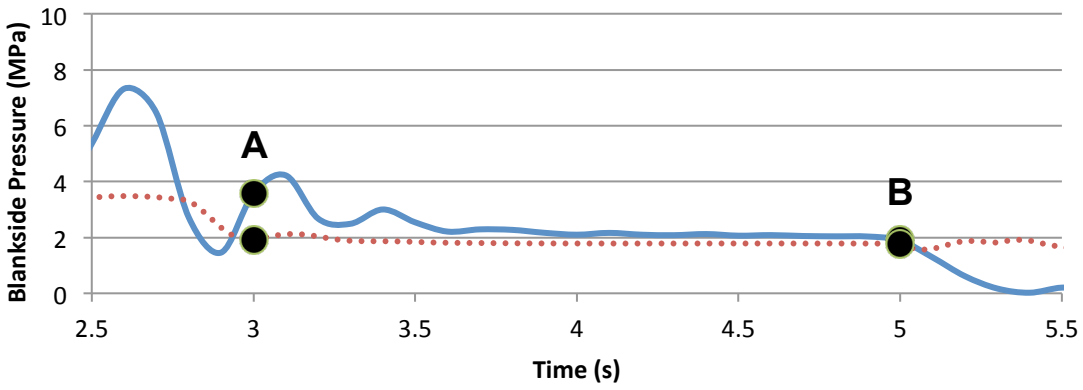

Figure 6.13 Boom Cylinder Extension Blankside Pressure for Data Set 1
(Solid line: experimental, dotted line: simulation)

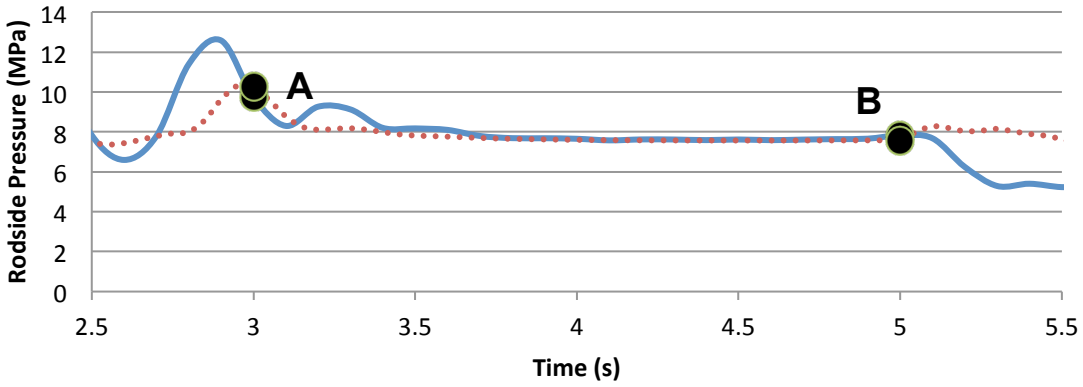

Figure 6.14 Boom Cylinder Extension Rodside Pressure for Data Set 1
(Solid line: experimental, dotted line: simulation)

When the cylinder is travelling in the opposite direction, towards the home position, the blankside and rodside pressures do not appear to follow the exact trend of the measured data, as shown in Figure 6.15 and Figure 6.16. Between 'C' and 'D,' the measured pressures both decrease slightly, while the simulated data increases during steady state operation. This is

expected to be caused by the order of calculations performed to determine the blankside and rodside pressures for this direction of motion, as discussed in Chapter 5.

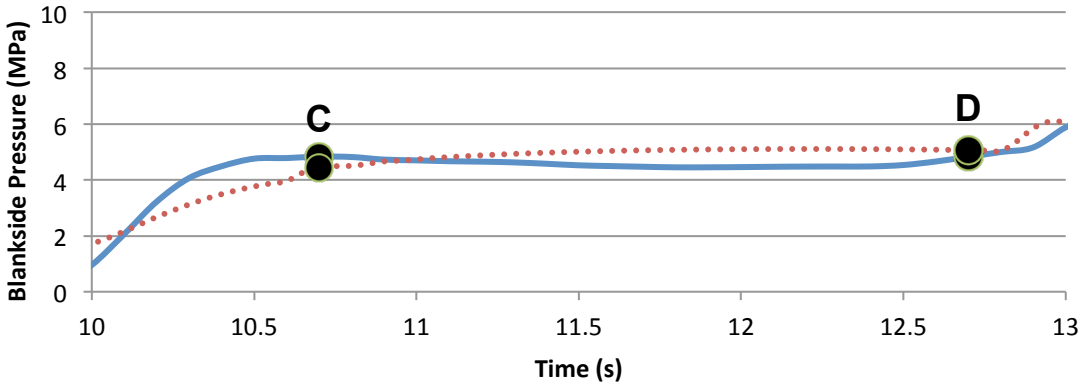

Figure 6.15 Boom Cylinder Blankside Pressure for the Retraction Motion of Data Set 1 (Solid line: experimental, dotted line: simulation)

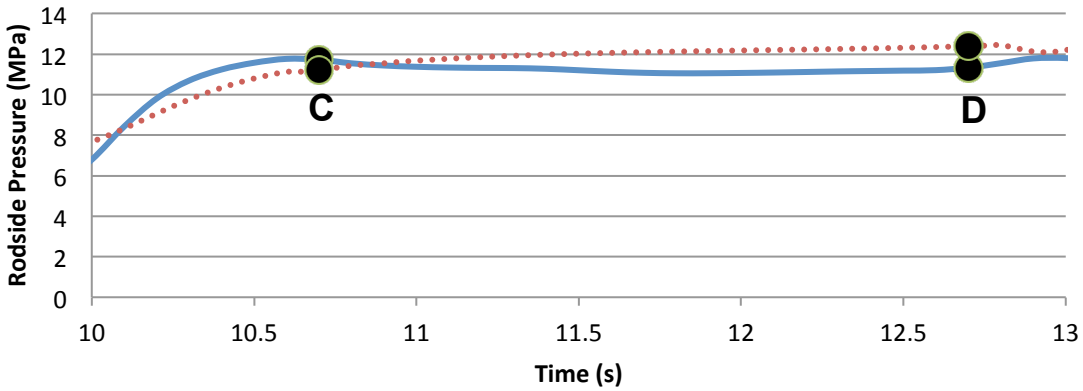

Figure 6.16 Boom Cylinder Rodside Pressure for the Retraction Motion of Data Set 1 (Solid line: experimental, dotted line: simulation)

Using the same tuning factors determined by running several simulations of data set 1, a second set of data was examined at a different operating point. Figure 6.17 shows the control valve inputs for data set 2.

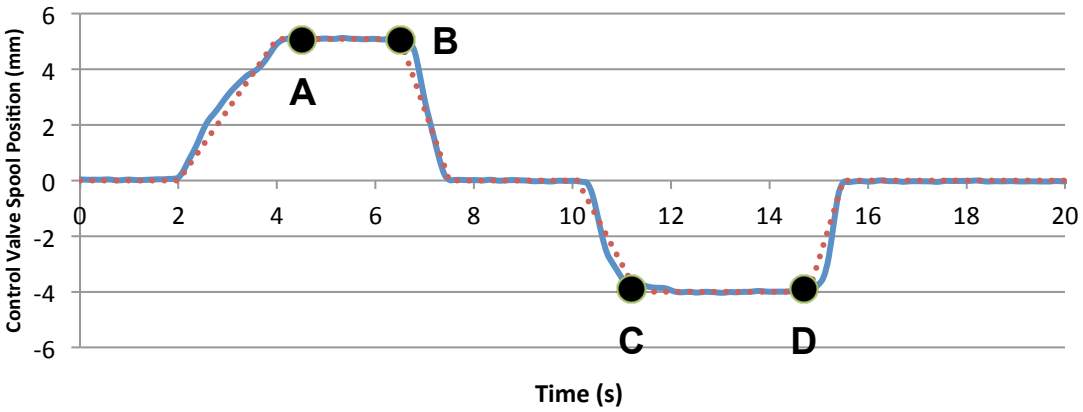

Figure 6.17 Boom Function Control Valve Spool Displacement Inputs for Data Set 2
(Solid line: experimental, dotted line: simulation)

The boom cylinder length is presented in Figure 6.18, and it can be seen that the simulated data, the results from set 1 correlate better to the measured data. This suggests that the polynomial curves fitted to the lumped hydraulic resistance may need further adjustment to achieve simulation results closer to the real system over a full range of operating points.

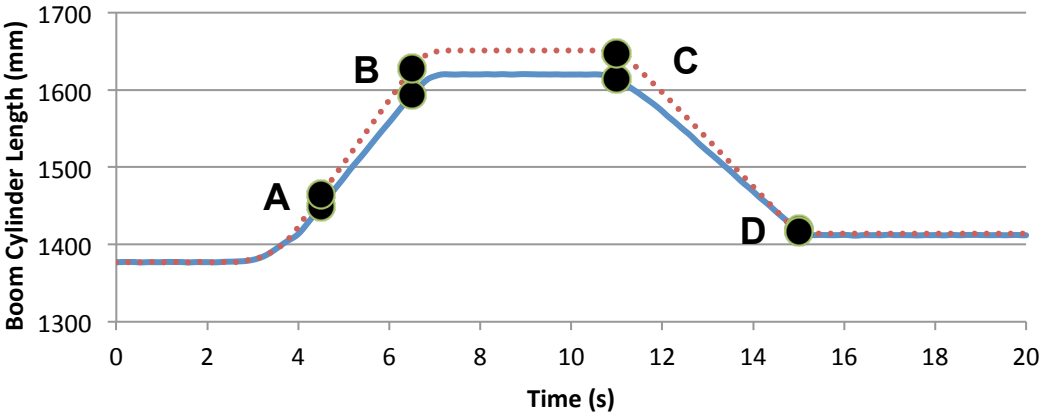

Figure 6.18 Boom Cylinder Length for Data Set 2
(Solid line: experimental, dotted line: simulation)

The velocity of the boom cylinder in Figure 6.19 confirms that the simulated velocity of the system is higher than the measured results for this operating point.

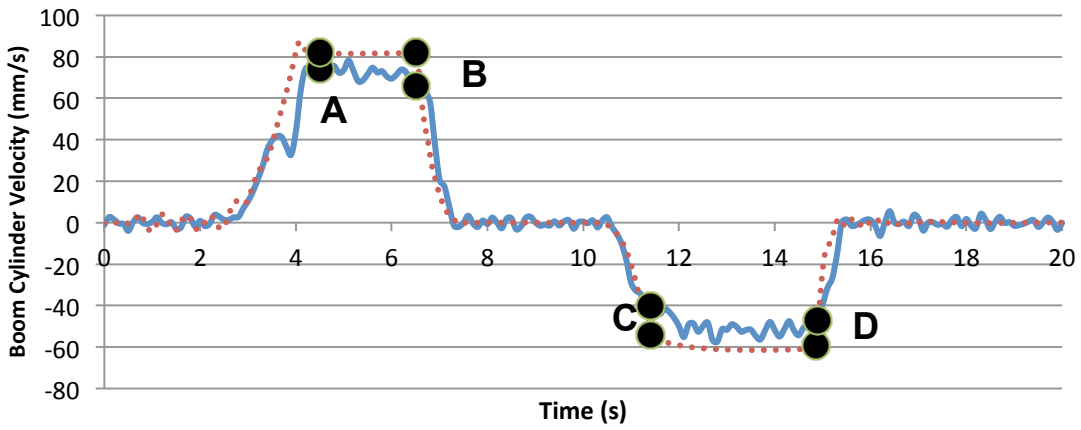

Figure 6.19 Boom Cylinder Velocity for Data Set 2
(Solid line: experimental, dotted line: simulation)

The results for the boom cylinder pressures during the extension motion are shown in Figure 6.20 and Figure 6.21. The blankside pressure in Figure 6.20 is very close to the measured results, in both magnitude and trend of data. The rodside pressure in Figure 6.21, during the steady state, is consistently higher than the measured results, but demonstrates a similar trend. This is due to the higher velocity of the simulated system.

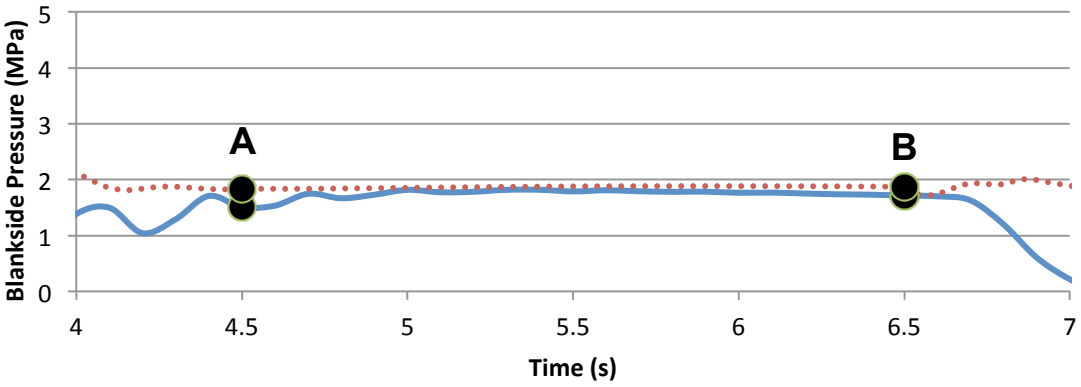

Figure 6.20 Boom Cylinder Blankside Pressure for the Extension Motion of Data Set 2
(Solid line: experimental, dotted line: simulation)

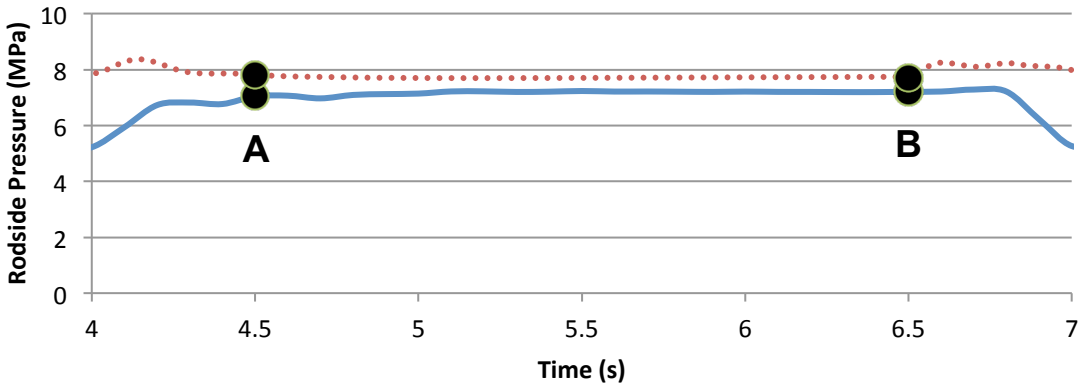

Figure 6.21 Boom Cylinder Rodside Pressure for the Extension Motion of Data Set 2
(Solid line: experimental, dotted line: simulation)

The cylinder pressures for the retraction motion of data set 2 are shown in Figure 6.22 and Figure 6.23. A similar comparison can be seen between the data for set 2 and set 1, shown in Figure 6.15 and Figure 6.16. These figures do not demonstrate the same magnitude of pressure decrease that was measured in data set 1, but the simulated results still have the increasing trend that is expected to be caused by the order of calculations for the this direction of travel.

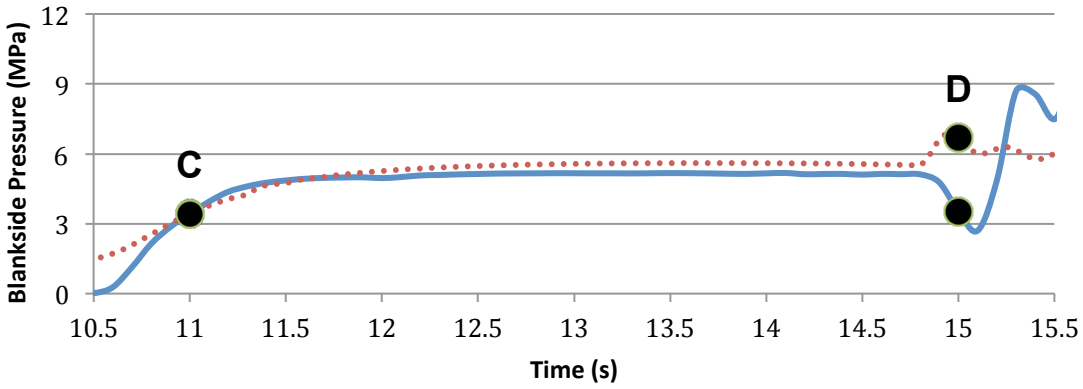

Figure 6.22 Boom Cylinder Blankside Pressure for the Retraction Motion of Data Set 2
(Solid line: experimental, dotted line: simulation)

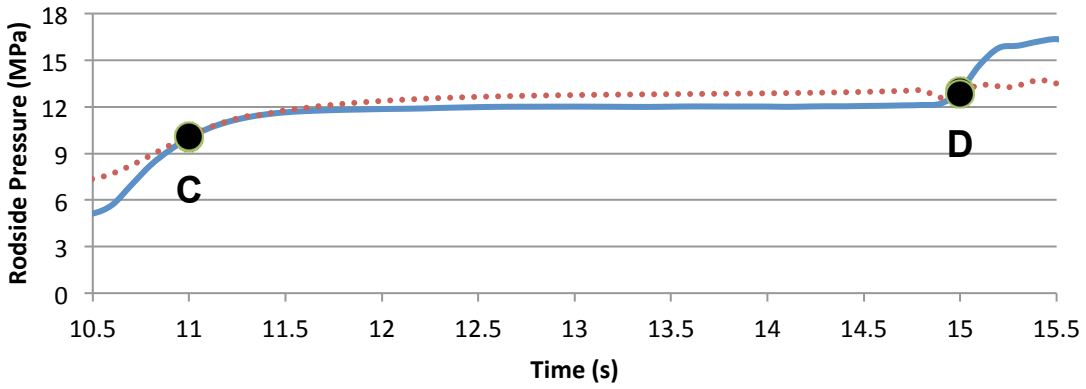

Figure 6.23 Boom Cylinder Rodside Pressure for the Retraction Motion of Data Set 2
(Solid line: experimental, dotted line: simulation)

The results presented for the boom function of the JD 410G workgroup show that the trends of the simulated data are similar to the measured data. The order of calculations during the retraction motion of the actuator causes the trends between the two sets of the data to be different, although the magnitude of the cylinder pressures are relatively close to each other.

6.3.2 Stick Function Results

Similar to the boom function, the following results are for two sets of data collected for the stick function, with the results for data set 1 being tuned, and the results for data set 2 using the final tuning factors from data set 1. Figure 6.24 shows the stick control valve spool position used at the inputs for data set 1.

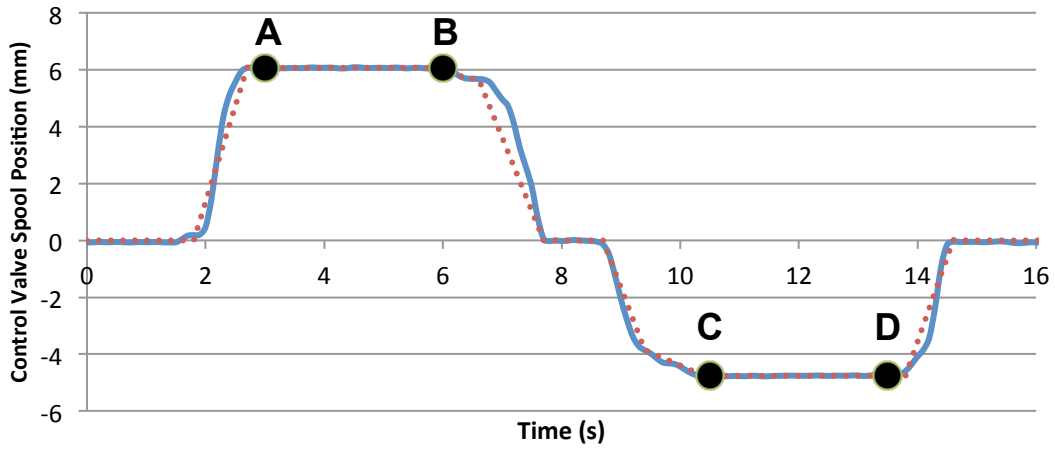

Figure 6.24 Stick Function Control Valve Displacement Inputs for Data Set 1
(Solid line: experimental, dotted line: simulation)

The position of the stick cylinder is presented in Figure 6.25, and it can be seen that the simulated cylinder travels slightly further during retraction, and less during extension than the measured data.

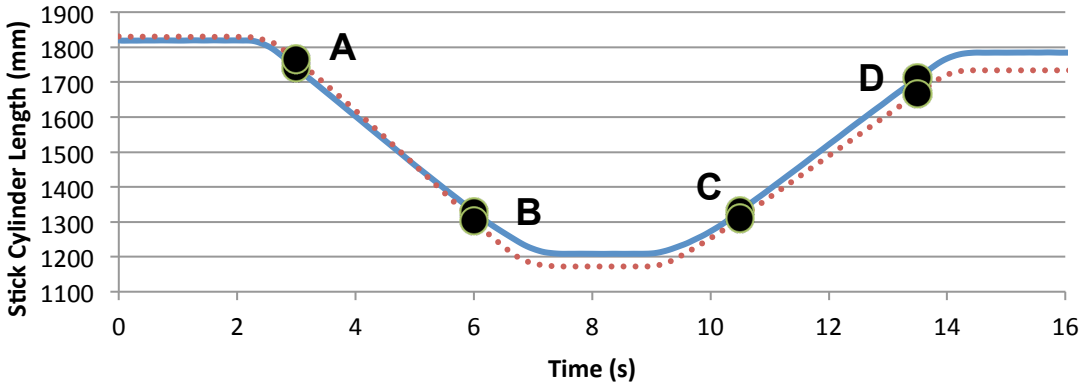

Figure 6.25 Stick Cylinder Length for Data Set 1
(Solid line: experimental, dotted line: simulation)

Similar to the cylinder length, Figure 6.26 shows that the simulated cylinder velocity is greater than the measured data between 'A' and 'B,' and then is slower during the extension between 'C' and 'D.' Note that the trend of the simulated data does not follow the measured data between points 'A' and 'B.' Similar to the boom discussion, the order of calculations during cylinder retraction is responsible for this behavior.

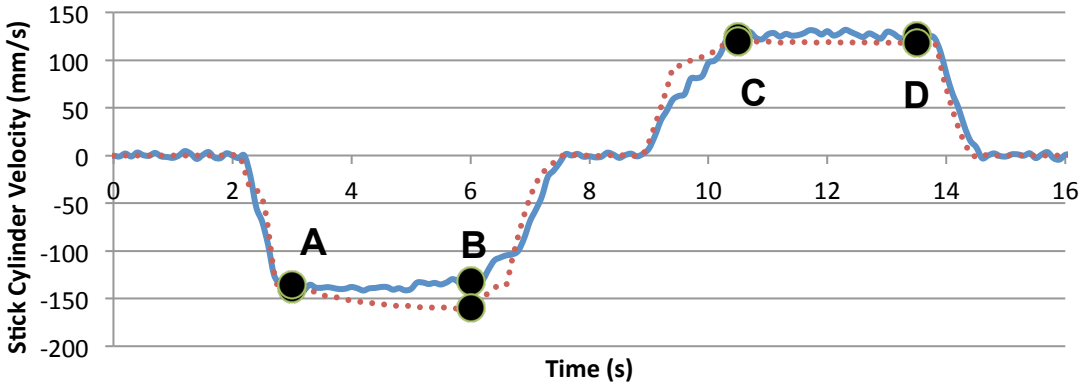

Figure 6.26 Stick Cylinder Velocity for Data Set 1
(Solid line: experimental, dotted line: simulation)

The results for pressure follow the same trends encountered with the boom cylinder; during retraction, there is a separation between the measured and simulated results, while the extension direction of cylinder travel yields close pressures and trends of data. Figure 6.27 and Figure 6.28 show the blankside and rodside pressures for the retraction motion of the stick cylinder. In both figures, the simulation pressure at 'A' is lower than the measured values, and at 'B,' the pressures appear to be converging over time.

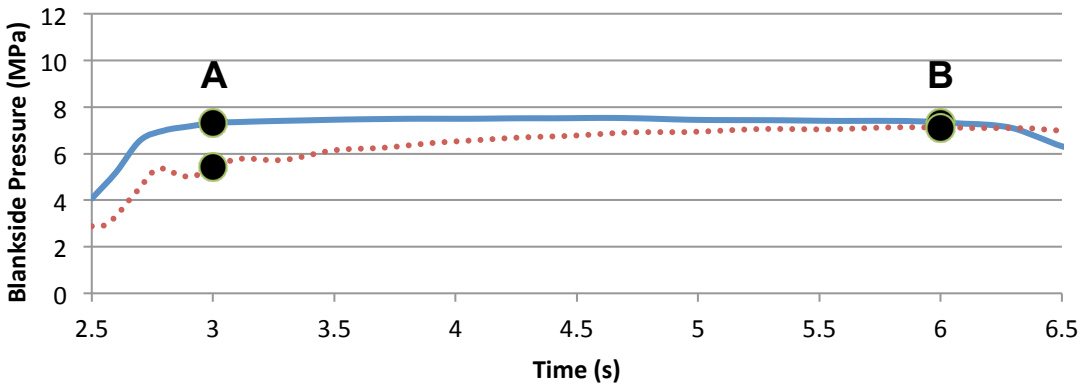

Figure 6.27 Stick Cylinder Blankside Pressure for the Retraction Motion of Data Set 1 (Solid line: experimental, dotted line: simulation)

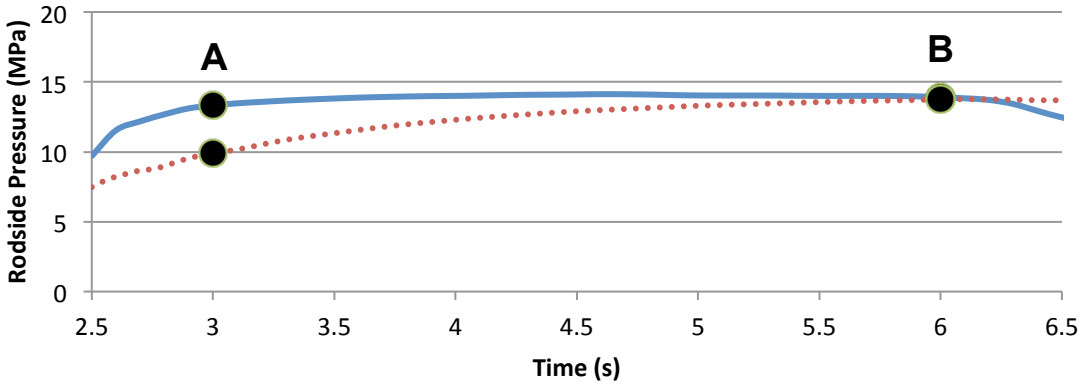

Figure 6.28 Stick Cylinder Rodside Pressure for the Retraction Motion of Data Set 1 (Solid line: experimental, dotted line: simulation)

The results for the chamber pressures during cylinder extension between 'C' and 'D' yield much closer results, as shown in Figure 6.29 and Figure 6.30. As can be seen in the figures, there is very little separation between the pressures during the steady-state extension of the stick cylinder.

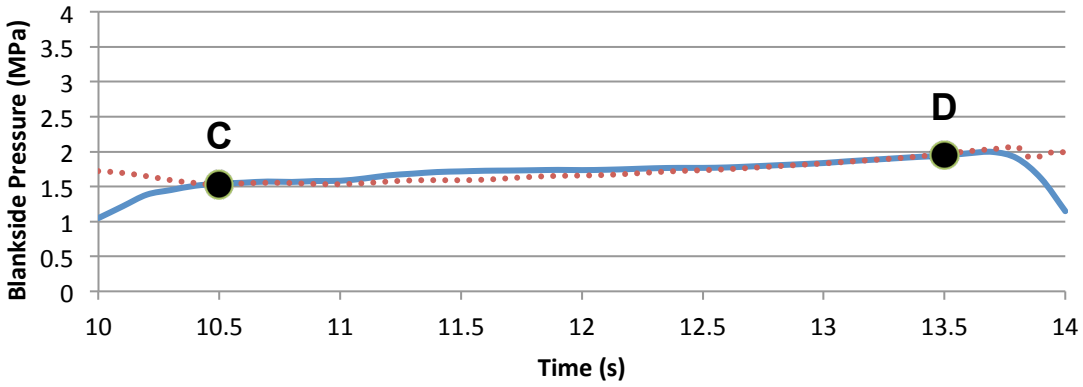

Figure 6.29 Stick Cylinder Blankside Pressure for the Extension Motion of Data Set 1 (Solid line: experimental, dotted line: simulation)

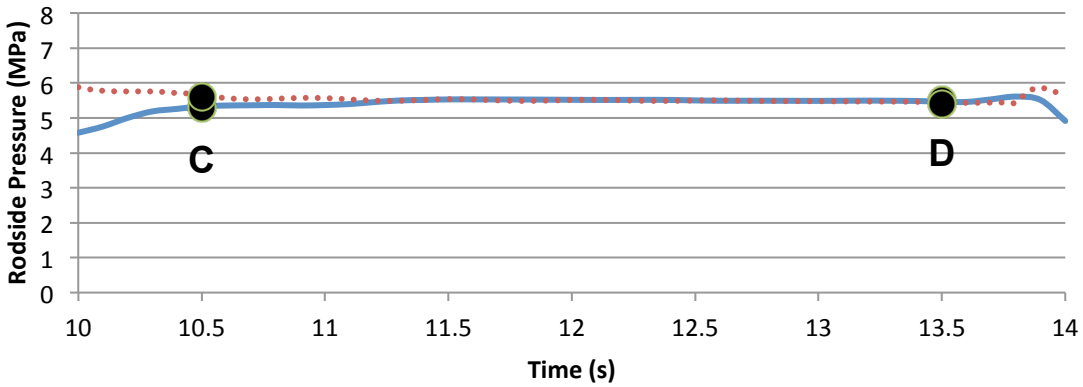

Figure 6.30 Stick Cylinder Rodside Pressure for the Extension Motion of Data Set 1 (Solid line: experimental, dotted line: simulation)

Figure 6.31 shows the control valve spool position inputs for data set 2 of the stick cylinder. As previously mentioned, the simulated results for data set 2 are generated using the same tuning factors as data set 1.

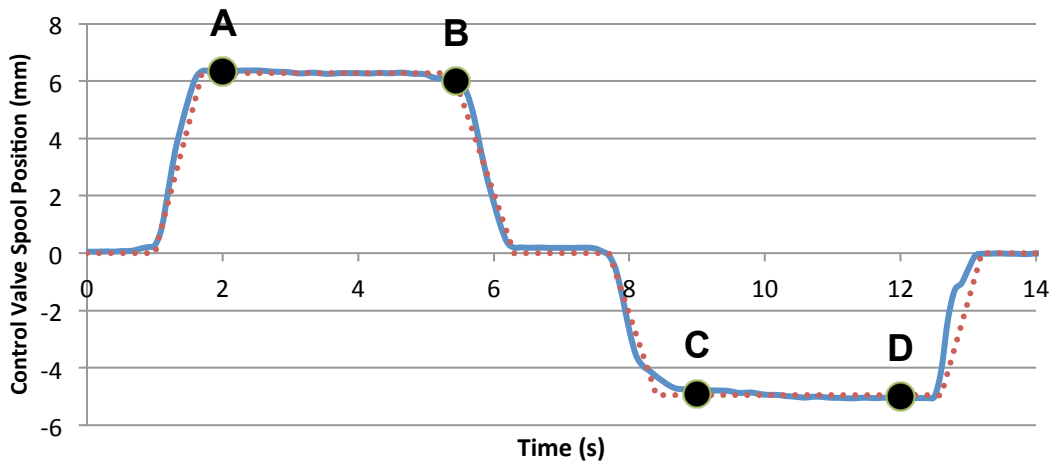

Figure 6.31 Stick Function Control Valve Displacement Inputs for Data Set 2
(Solid line: experimental, dotted line: simulation)

The stick cylinder length plots for data set 2 are shown in Figure 6.32, and a similar trend to data set 1 is observed.

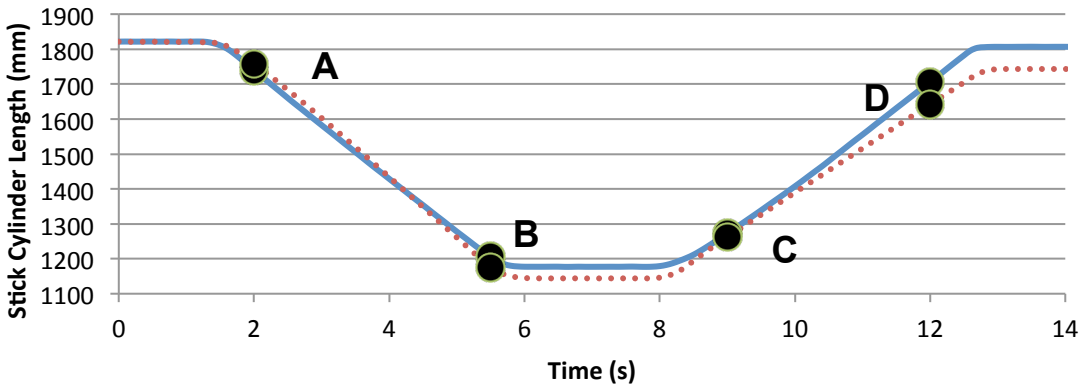

Figure 6.32 Stick Cylinder Length for Data Set 2
(Solid line: experimental, dotted line: simulation)

The stick cylinder velocities are shown in Figure 6.33, and for the steady-state retraction (between 'A' and 'B'), a similar trend to data set 1 is observed. For the steady-state extension (between 'C' and 'D'), it can be seen that the simulated velocity is lower than the measured value. The measured velocity between 'C' and 'D' also appears to increase with time; this is due to the control valve spool displacement slightly increasing with time, as can be seen in Figure 6.31.

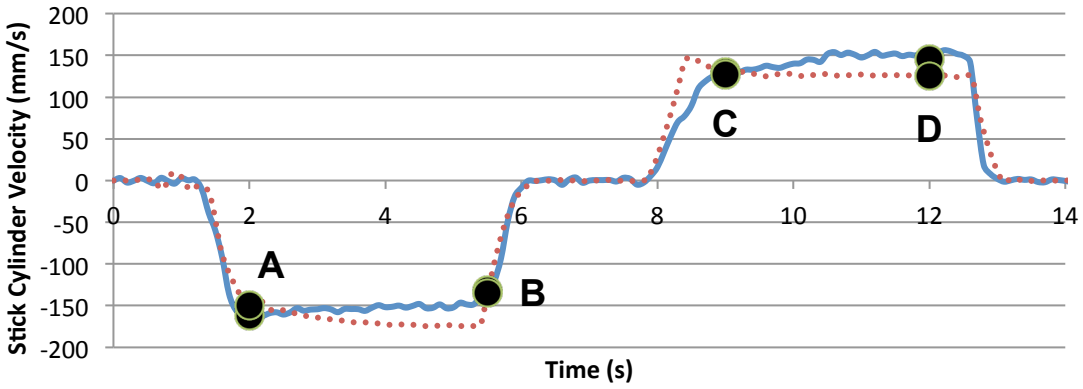

Figure 6.33 Stick Cylinder Velocity for Data Set 2
(Solid line: experimental, dotted line: simulation)

The stick cylinder chamber pressures during retraction are shown in Figure 6.34 and Figure 6.35. For the steady-state retraction, the trend of data is similar between data set 1 and 2 for the simulated results. At 'A,' there is a relatively large separation between the measured and simulated pressures, while at 'B' the results are closer together.

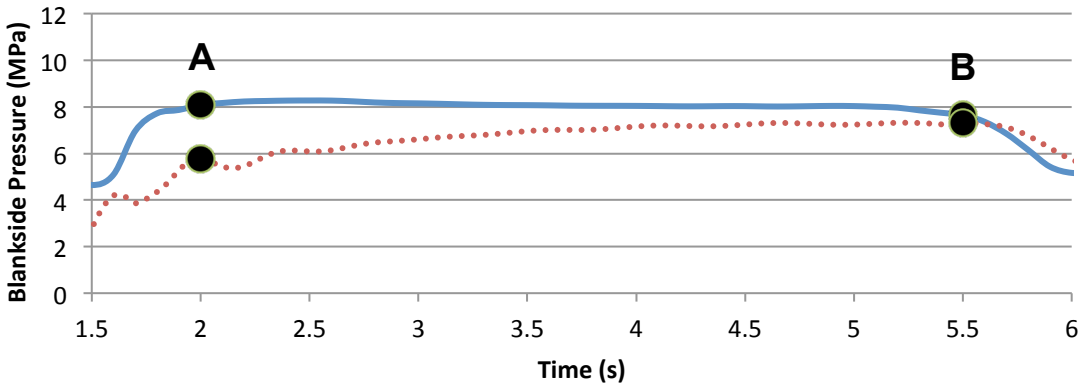

Figure 6.34 Stick Cylinder Blankside Pressure for the Retraction Motion of Data Set 2
(Solid line: experimental, dotted line: simulation)

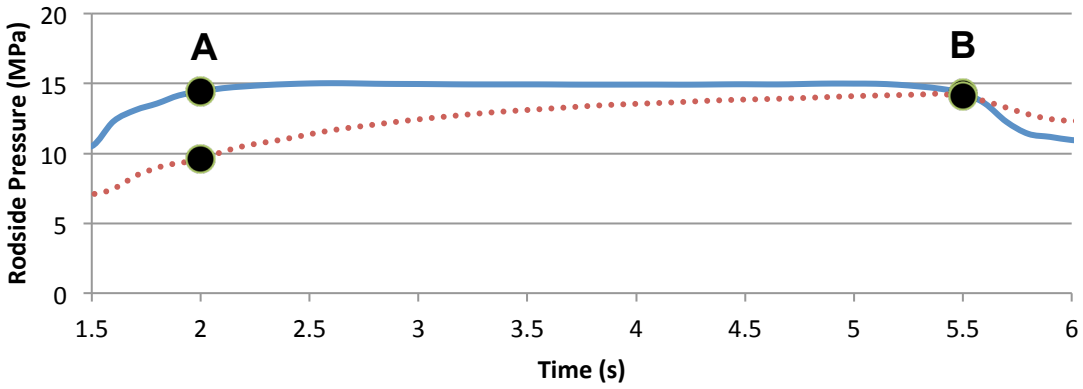

Figure 6.35 Stick Cylinder Rodside Pressure for the Retraction Motion of Data Set 2
(Solid line: experimental, dotted line: simulation)

The stick cylinder pressures for the extension direction of travel are shown in Figure 6.36 and Figure 6.37. For both figures, the apparent trend of the data is common to the measured and simulated results. The magnitude of the rodside pressures in Figure 6.37 are similar, while that of the blankside pressures in Figure 6.36 have some separation. This separation is due to the slower speed of the actuator predicted by the simulation results.

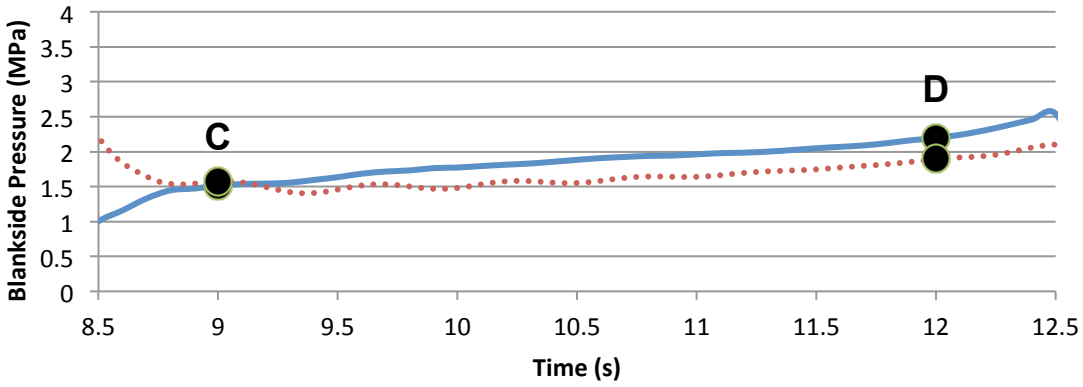

Figure 6.36 Stick Cylinder Blankside Pressure for the Extension Motion of Data Set 2
(Solid line: experimental, dotted line: simulation)

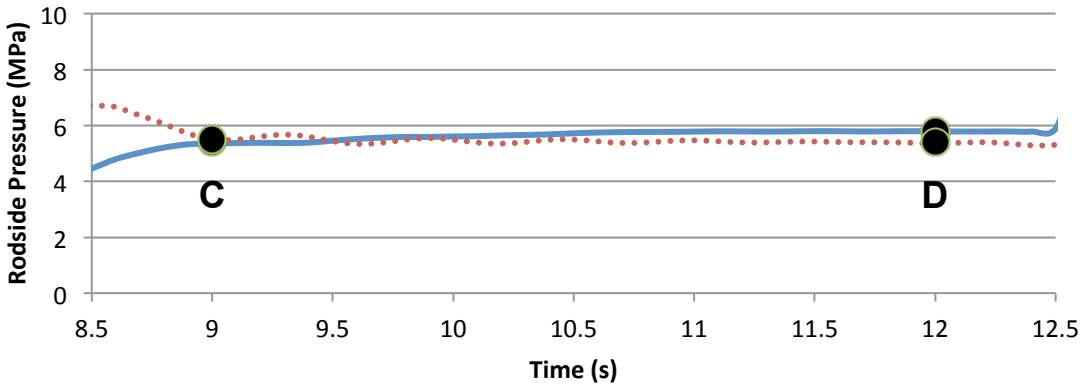

Figure 6.37 Stick Cylinder Rodside Pressure for the Extension Motion of Data Set 2 (Solid line: experimental, dotted line: simulation)

The results for the stick function are very similar to those of the boom, in that it can be seen that under steady-state operating conditions, the model can predict the approximate magnitudes and trends of the measured values, especially for cylinder extension.

6.3.3 Bucket Results

In Chapter 5, the polynomial curve representing the lumped hydraulic resistance of the bucket control valve orifice was identified as containing a significant amount of uncertainty, due to the operation of the bucket function during data collection. Without means of measuring the internal phenomena of the control valve, the bucket simulation model was *tuned* using the same procedure as the boom and stick functions; however, it is acknowledged that this method of tuning will only apply to a specific set of inputs, and that moving away from these inputs will produce poor results without further tuning of the model, as discussed in Chapter 5. For this reason, only one set of tuned data will be presented in this section; if the model can be tuned for one operating point, it can be tuned to produce similar results for any other operating point.

Figure 6.38 shows the control valve spool position inputs used to compare the simulated system to the measured parameters.

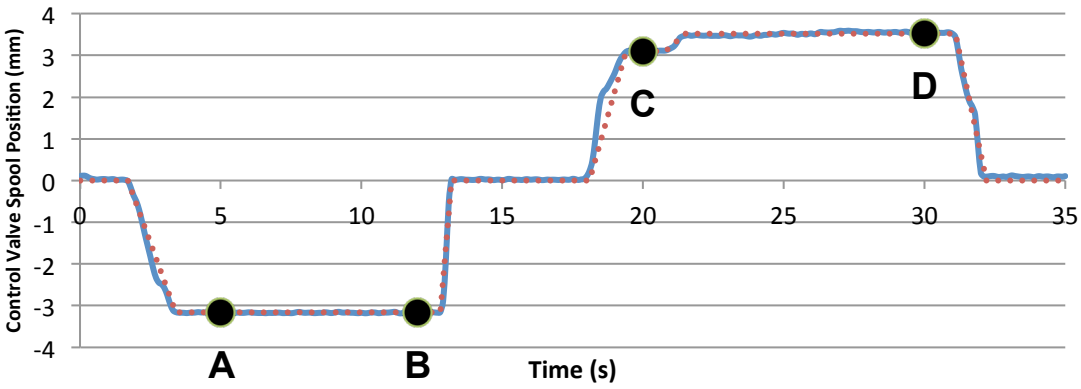

Figure 6.38 Bucket Function Control Valve Displacement Inputs
(Solid line: experimental, dotted line: simulation)

The bucket cylinder length is presented in Figure 6.39, and it can be seen that the simulated motion is very close to that of the measured values, especially at the beginning and end points of the plots.

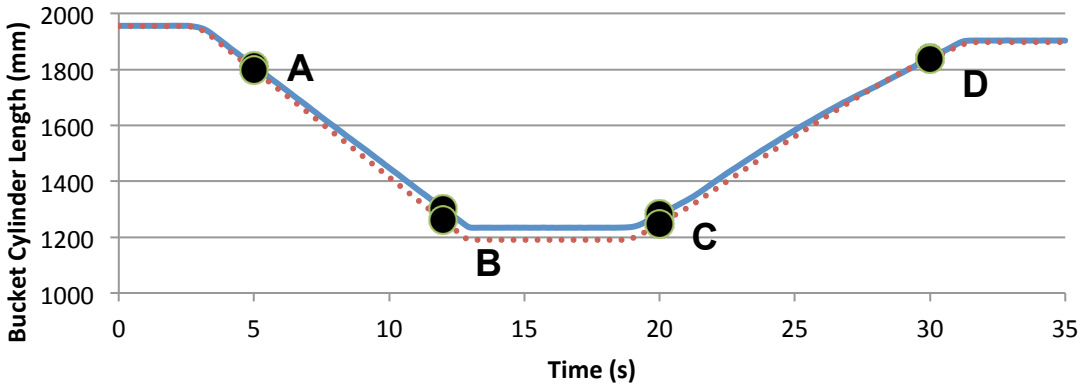

Figure 6.39 Bucket Cylinder Length Comparison
(Solid line: experimental, dotted line: simulation)

The bucket cylinder velocity is shown in Figure 6.40, and it can be seen that there is a high degree of agreement between the two curves, with a slight exception between about 25 and 30 seconds, where the simulated velocity is somewhat higher than the measured value. This can be explained by looking at the pressure profiles during the steady state extension of the bucket cylinder to follow.

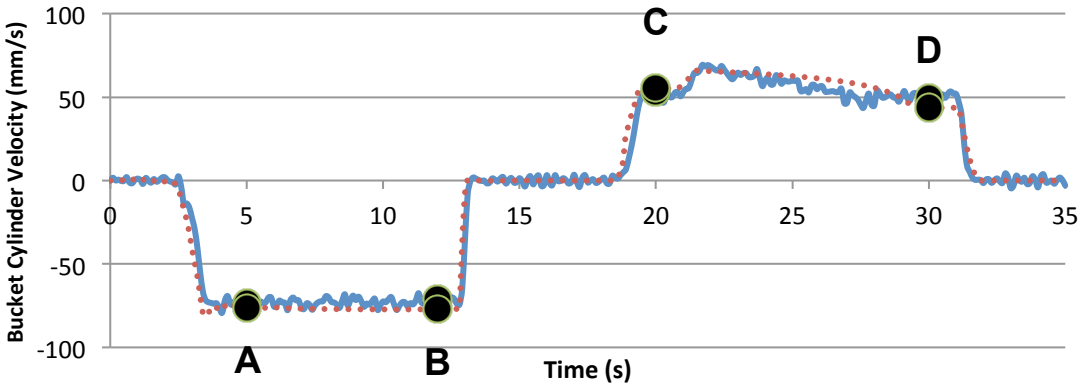

Figure 6.40 Bucket Cylinder Velocity for Comparison
(Solid line: experimental, dotted line: simulation)

First considering the steady-state retraction of the bucket cylinder, the blankside and rodside pressures are shown in Figure 6.41 and Figure 6.42. Both plots show a strong agreement between the simulation results and the measured data. In contrast to the boom and stick functions, the simulated data for the retraction of the bucket cylinder does not have a large deviation from the measured results; this is thought to be caused by the relatively low loads placed on the bucket cylinder during operation. Rather than the loading due to the mass of the bucket being the prime cause of pressure in the system, the pressures due to the metering valves dominating the results for the bucket circuit. While the order of calculations for the retraction is still causing error in the results, the reduced kinetic influence allows for the agreement of the results.

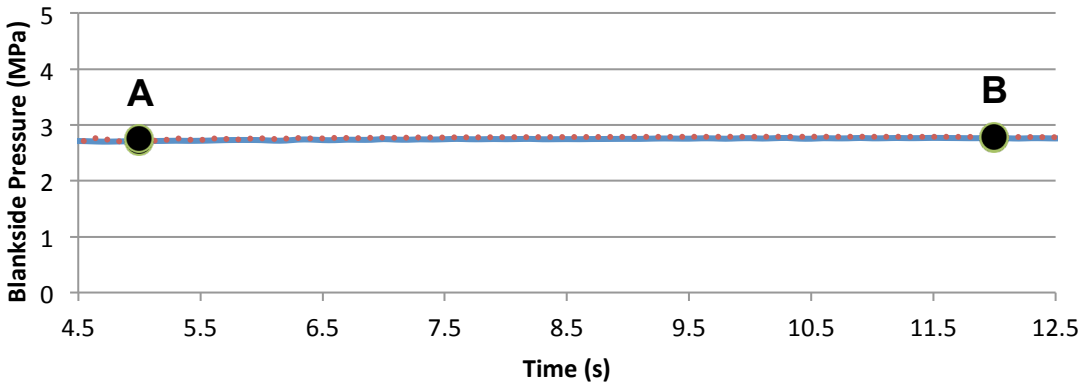

Figure 6.41 Bucket Cylinder Blankside Pressure during Retraction
(Solid line: experimental, dotted line: simulation)

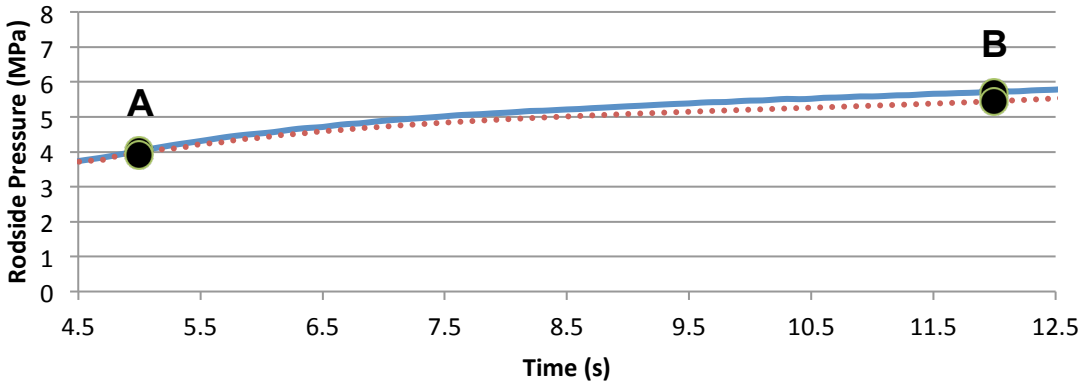

Figure 6.42 Bucket Cylinder Rodside Pressure during Retraction
(Solid line: experimental, dotted line: simulation)

The steady-state pressure results for the bucket cylinder during the extension motion are shown in Figure 6.43 and Figure 6.44. Both the blankside and rodside pressures have a considerable amount of separation between the measured and simulated data; this is caused by the difference between the real system's return line pressure and the simulated system's return line pressure. The extension of the bucket cylinder has relatively low pressures encountered on the blankside chamber of the actuator, resulting in flow being introduced to the system by an anti-cavitation check valve (which is internally contained by the control valve body). The difference between the return line pressures between the real and simulated systems will effectively raise the pressure of the simulated system by a fixed amount.

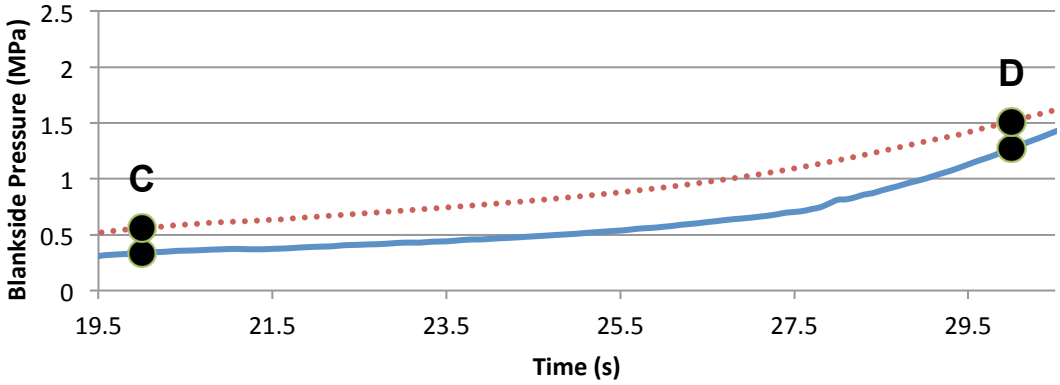

Figure 6.43 Bucket Cylinder Blankside Pressure during Extension
(Solid line: experimental, dotted line: simulation)

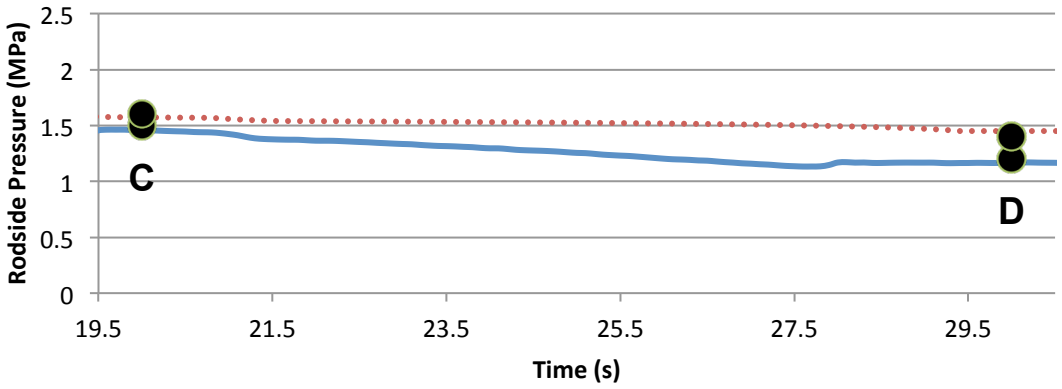

Figure 6.44 Bucket Cylinder Rodside Pressure during Extension
(Solid line: experimental, dotted line: simulation)

To demonstrate this, Figure 6.45 and Figure 6.46 show the previous two figures, with the simulated pressure reduced by 0.24 MPa, and now it can be seen that the adjusted results are closer than before. The blankside pressures agree very similar to the tuned results from the boom and stick functions. There is some separation between the rodside results, although the difference in the trend of the data is likely due to the separation experienced in the kinetic forces along the bucket cylinder, as seen in Figure 6.4.

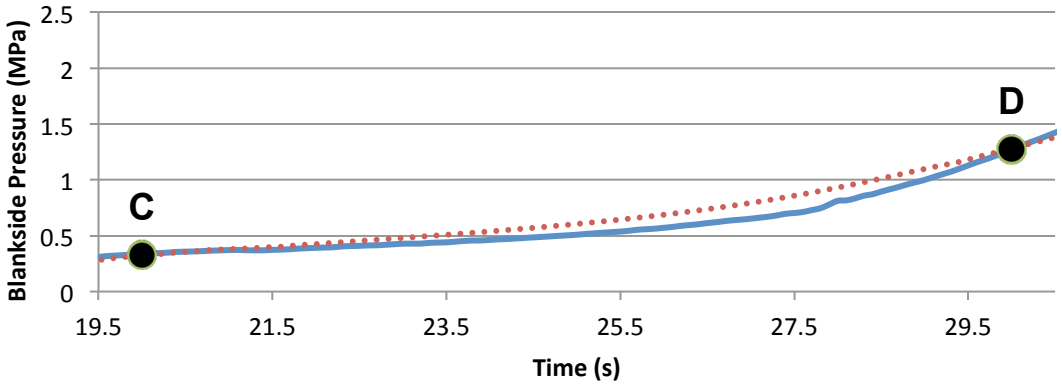

Figure 6.45 Adjusted Bucket Cylinder Blankside Pressure during Extension
(Solid line: experimental, dotted line: simulation)

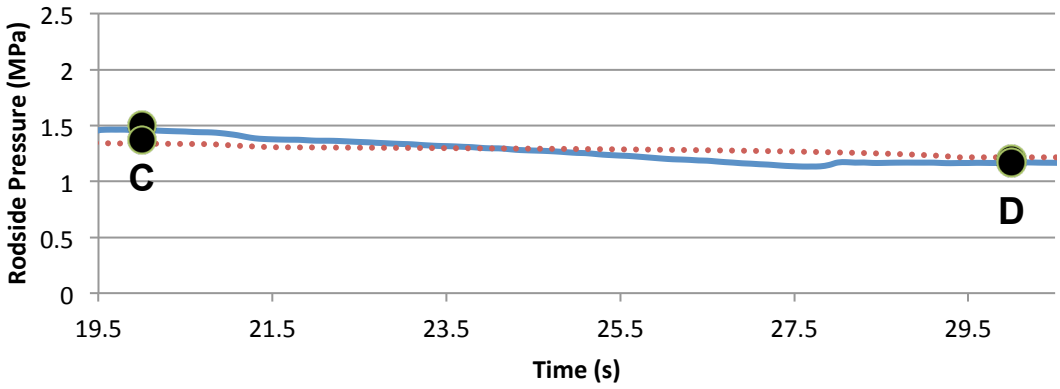

Figure 6.46 Adjusted Bucket Cylinder Rodside Pressure during Extension
(Solid line: experimental, dotted line: simulation)

6.4 Summary

The model developed in this thesis has been compared to direct measurements taken from the physical system, for steady-state cylinder motion. During the extension motion of the three hydraulic actuators, the results were similar between the two systems. During the retraction motion of the actuators, however, it was observed that the simulation results do converge to the physical data, although the convergence takes longer to attain than for the extension direction. Future work will investigate this trend.

Chapter 7: Conclusions and Recommendations

7.1 Summary and Conclusions

The research goal stated in Section 1.3 was to develop a computer model capable of simulating the backhoe section of the John Deere 410G workgroup. The modeling has been separated into three sections, each having its own objectives, which were to:

1. Develop a set of equations to fully describe the motion of the backhoe workgroup. The motion of the backhoe workgroup must consider the position, velocity, and acceleration of all the modeling points.
2. To use a kinetic analysis to predict the forces acting at each modeling point for any motion of the backhoe workgroup. The main goal is to predict the forces acting along each of the boom, stick, and bucket actuators.
3. Develop a set of equations to predict the pressures and flows in the hydraulic system of the JD 410G for a given set of operator inputs, in the form of control valve spool displacements.
4. Compare the results of the developed model with experimental data to evaluate the functionality of the fully assembled backhoe simulation model.

The remainder of this section will discuss the above objectives and if they were satisfactorily achieved in this thesis.

7.1.1 Kinematic Relationships

The kinematic equations developed in Chapter 3, and presented in detail in Appendix B are capable of predicting the motion of the backhoe workgroup for a given set of actuator inputs. The comparison presented between the simulated motion and measured motion shows a high degree of correlation between the two sets of data; therefore, it is concluded that the objective stated in Chapter 3 has been met.

7.1.2 Kinetic Relationships

The kinetic equations presented in Chapter 4, and in full detail in Appendix D could not be quantitatively compared to experimental results for a dynamic motion of the backhoe workgroup. Rather, a static model validation revealed that the assumption of negligible actuator mass lead to the kinetic equations under-predicting the forces along the boom and stick cylinders. To address this, these forces were increased by a linear scaling factor and it was shown that the adjusted forces are very close to the measured values. A qualitative assessment ensured that the trends of the data for a given set of dynamic inputs could be explained logically. The objectives stated in Chapter 4 have been partially met, as future work is required to accommodate the masses of the hydraulic actuators.

7.1.3 Hydraulic Modeling

The hydraulic model was developed using a power bond graph approach, which ensured that the equations used to represent the system all had the appropriate causality. The development of the hydraulic model involved first considering the extension direction of actuator motion and then adding additional equations to the PBG to permit travel in the opposite direction. This approach is expected to be problematic for the retraction direction of motion, as the order in which the calculations are carried out do not appear to be in a logical manner, as discussed in Chapter 5. The equations developed in Chapter 5 partially fulfill the objectives of the hydraulic modeling, as future studies are required to properly include the retraction direction of motion.

7.1.4 Experimental and Simulated Results Comparison

Chapter 6 compared measured data with simulated results for a number of data sets. The general trends show that the simulation results correlate well to the experimental data for the extension motion of the hydraulic actuator. For the retraction motion, the results are not as good, which is expected from the discussion provided in Chapter 5. While the results for retraction do not correlation as well as those for extension, it was observed that the magnitude of the compared data was comparable, while the trends predicted from the simulation model did not exactly match the measured data. As mentioned, this is expected to stem from the order of calculations

used in the hydraulic modeling, and addressing this issue should yield better results for cylinder retraction.

7.1.5 Concluding Comments

The research presented in this thesis has provided the framework for development of a computer simulation model of a JD 410G backhoe workgroup. The causality of the equations developed in the kinematic and kinetic modeling created issues when developing the hydraulic model, as including the equations for both directions of travel proved problematic and is an area of future study. The overall objective of this thesis was to develop a computer model capable of simulating the JD 410G backhoe workgroup. While future studies are required to further increase the accuracy of the model, especially for the retraction direction of motion, this objective has been met in this thesis.

The completion of these objectives allow the research to focus on the global project objectives, namely quantifying the effect an operator has on a given machine. This effect would likely be introduced into the simulation model by means of the control valve input; for a given set of inputs, it is desired to simulate the control strategies that would be exhibited by operators of various skill levels. This would then allow the fuel consumption and productivity of a given machine to be investigated across various operator skill levels.

7.2 Future Work

Some future considerations identified throughout this thesis are:

1. Inclusion of the actuator masses in the kinetic modeling of the backhoe workgroup to increase the accuracy of the predicted cylinder forces.
2. Development of a load sensing pump model, allowing for the dynamics of the system to be modeled.
3. Additional development of the control valve model, including more accurate lumped hydraulic resistances and inclusion of a compensator model to allow for the LS functionality to be included.

4. Development of a method to include both extension and retraction actuator motion in a way that allows the equations for each direction to accurately predict the pressures and flows in the system. This could involve alterations of the hydraulic model, or changes to the kinematic and kinetic relationships to accommodate a more traditional hydraulic modeling approach.
5. Inclusion of a method of stopping the hydraulic actuators when the limits of their stroke is reached.

References

[1] Zimmerman, J.; Pelosi, M.; Williamson, C.; Ivantysynova, M. *Energy Consumption of an LS Excavator Hydraulic System*, Proceedings of 2007 ASME International Mechanical Engineering Congress & Exposition, IMECE2007, Seattle, USA. 2007.

[2] Andruch, J. and Lumkes, J., *A Hydraulic System Topography with Integrated Energy Recovery and Reconfigurable Flow Paths Using High Speed Valves*. Proceedings of the 51st National Conference on Fluid Power (NCFP), Las Vegas, USA. 2008.

[3] Engja, H. and Pederson, E., *Modelling and Simulation of Hydraulic Systems using Bond Graphs and Model Libraries.* Proceedings of the 31st Annual Summer Computer Simulation Conference, SCSC1999, Chicago, USA. 1999.

[4] Herman, T.; Bonicelli, B.; Selvila, F.; Monison, M.; Bergeon, B. *Bond-graph Modelling and Identification of a High Power Hydraulic System.* Eleventh IASTED International Conference on Modelling, Identification, and Control, Innsbruck, Austria. 1992.

[5] Novak, A. and Larson, C. *A Computer Simulation of Backhoe Type Excavators.* SAE Technical Paper Series 911838(1991): 41-48.

[6] Koivo, A. Kinematics of Excavators (Backhoes) for Transferring Surface Material. Journal of Aerospace Engineering 7.1(1994): 17-32.

[7] Lance, G. and Prescott, C. *Modeling and Dynamic Simulation of a Hydraulically Driven Backhoe.* SAE Technical Paper Series 901640(1990).

[8] Dransfield, P. *Hydraulic Control Systems – Their Design and Analysis of their Dynamics.* Springer-Verlag, New York, USA. 1981.

[9] Merritt, H. *Hydraulic Control Systems*. John Wiley & Sons, Inc., New York, USA. 1967.

Appendix A: Fluid Power Energy Saving Survey Paper

Contents

A.1 Introduction

Hydraulic systems are used in many applications around the world. They are commonly selected for their reliability, controllability, and most important – very high power density. Unfortunately, these systems can have low overall efficiencies when compared to electric or mechanical alternatives. With the current push towards reducing emissions and optimizing fuel consumption, a large body of research and development is working to improve the efficiency of fluid power systems. The purpose of this paper is to provide a condensed summary of the research that has been done to improve the low efficiency reputation of fluid power systems over the past two decades.

The organization of this paper has been divided into three main sections, and further into numerous subsections. The three main sections present component improvements and innovations, circuit design considerations, and the final section has been devoted to hydraulic hybrid vehicles. The authors recognize that not all studies pertaining to improving energy efficiency in hydraulic systems are considered and apologize in advance for any omissions.

A.2 Component Improvements and Innovations

It is well known that any improvements to the efficiency of the individual hydraulic components of a system will also improve the system's efficiency. There is a large amount of research and industry design devoted to improving the efficiency of components used in circuits. While it would be impossible to discuss all areas of research and design, the following are considered important and relevant to future system performance.

A.2.1 Pumps and Motors

Future hydraulic systems will continue to rely heavily on axial piston pumps and motors, which have the disadvantage of low efficiencies at low pressure, low speed operating regions. The increasing popularity of displacement controlled systems requires pumps to have increased efficiency at low pressures to realize advantages over traditional systems. Ivantysynova and

Baker have introduced the shaped valve plate, having ripples of amplitude 1-2 micrometers into current pumps, while reporting power loss decreases of about 60% in the low pressure operating region. Work is being completed to optimize the valve plate design for minimal energy losses over the entire operating range of the pump [A1][A2].

The Danish company Innas BV has developed a new style of axial piston pump, called the *floating cup pump.* Initial design of this component contains 24 pistons arranged in two rings of 12 pistons, mounted around a central shaft. The floating cup pump is designed with the intention of mass production, resulting in lower costs to the consumer. Simulations of the floating cup principle have shown this pump to be a promising new idea with benefits over other axial piston designs, including reduced pressure pulsations, independence between pump pressure and torque losses, quiet operation and increased efficiency [A3].

A.2.2 Accumulators

Traditionally, hydraulic accumulators have been made of steel, making them heavy and therefore not favorable for mobile applications. Recent designs are seeing accumulators constructed with carbon fiber bodies, greatly reducing weight [A4]. Accumulators themselves have efficiencies in excess of 95%, which is in part due to the presence of elastomeric foam contained in the gas side [A5]. In addition to damping pressure fluctuations, accumulators are finding uses as 'hydraulic batteries,' storing excess energy from gravity or decelerating loads [A6]. This stored energy can then be reused by the system, decreasing the power input requirements from the pump.

Li and Van de Ven have proposed a new addition to the hydraulic accumulator family: the open accumulator. The open accumulator does not contain a fixed volume of gas, but rather introduces a pneumatic compressor/motor to control the pressure and volume of gas present. The open accumulator can theoretically increase the energy density by an order of magnitude over traditional closed accumulators. In addition to increased storage capacity, small component size could result in more uses for accumulators, improving circuit efficiencies [A7].

A.2.3 Control Valves

The use of metering valves represents one of the largest sources of low system efficiency in hydraulic systems [A1]. One solution to reduce the losses would be to use independent metering valves. For example, typical four way metering valves use a spool to meter in and meter out flows at the same time. If the load requirements necessitate a meter-in configuration then having a meter-out presence at the same time creates unnecessary pressure losses across the meter-out part of the valve. By decoupling these flows, it is possible to achieve either meter-in, meter-out, or cross port flow with fewer sources of losses caused by throttling. Independent metering valves employ computer control, allowing for advanced control options [A8][A9]. Further, it is possible to control the actuator pressures; maintaining lower operating pressures will reduce energy consumption. A third advantage of a computer controlled valve is the ability to implement working mode selection to minimize energy consumption. Working mode selection ensures that pump flow is only supplied to the system when it is required [A8].

Another alternative would be to eliminate with throttling altogether. Tu et al. have proposed a three-way, self-spinning rotary on-off valve. This valve is used to essentially apply a digital approach to controlling the flow. The large orifice of the valve is either in the *on* or *off* position, allowing for flow control using pulse width modulation [A10].

A.2.4 The Hydraulic Transformer

The transformation from a given pressure and flow to another value having the same power content is not a new idea; this has been achieved using a rather inefficient system using two pumps joined together. The low efficiency of this concept has kept it from becoming popular in fluid power systems. Innas BV has taken another approach to the hydraulic transformer, introducing the Innas Hydraulic Transformer (IHT). The initial design of the IHT was simply a modified axial piston pump, containing an innovative three-port valve plate which is used to control the transformation. It was discovered that manipulation of the valve plate requires very low torques, favoring simple digital control [A11].

Recent advances in the design of the IHT have seen a shift to using the floating cup principle, which is expected to reduce noise, pressure and flow pulsations, and have favorable start-up behavior [A12]. The IHT has been found to deliver efficient transformations at higher operating pressures, with efficiencies in excess of 90% expected. At lower pressures, the IHT and typical throttling valves have similar efficiencies [A13]. Two additional benefits of the IHT include the ability to amplify pressures, and the option of returning gravity or deceleration energy into the circuit to reduce power inputs [A11][A13].

A.2.5 Alternative Power Sources

Many systems use an internal combustion engine in combination with a pump to deliver energy to a hydraulic system. Using two machines to deliver pressurized fluid to a circuit is inherently complex, and inefficient under part-load conditions. Work is being done to develop power supplies that do not rely on the crankshaft-driven hydraulic pump; two such examples found in literature are the free piston engine and the liquid piston Stirling engine pump.

Innas BV has developed the Chiron free piston engine; a two-stroke, single cylinder diesel engine having the combustion cylinder and hydraulic plunger cylinder connected. The Chiron is designed to be used with common pressure rail systems (to be discussed later) and the IHT. Flow is controlled by changing the frequency of combustion, and can range from 0-35 lpm. The Chiron has been demonstrated by use in a small lift truck [A14].

Hibi has built and tested another free piston engine, using two opposed pistons. Operation is similar to the Chiron, using a pause between combustion events to control the outputs. Testing has shown that operation in the low power range, between 0.0124-4.88 kW per cycle, has a thermal efficiency of a constant at 31%. This is an advantage over conventional power sources, which have decreased efficiencies under low load conditions [A15].

The second alternative hydraulic power source is a liquid piston Stirling engine pump, presented by Van de Ven. This could theoretically do away with mechanical linkages found in the internal combustion engine and pump combination, and has good sealing characteristics. This unit can also run in reverse mode, storing energy in the circuit and could use a variety of energy sources

such as hydrogen. This technology is presented a promising alternative, but large amounts of work are still to be done [A16].

A.3 Circuit Design Considerations

It is not just using more efficient components that will reduce the energy consumption of hydraulic systems, but also how these components are used. Using the best selection of components, properly sized for a given application can be an effective method to improve the overall efficiency of a hydraulic system by reducing avoidable losses.

A.3.1 Reduce Avoidable Losses

Zimmerman et al. has simulated a LS excavator system and determined that one-third of the machine's total energy consumption is made up of metering losses [A17]. One solution to elimination of metering losses is to design systems to use the displacement of the pump to control actuator motion [A18][A19][A20][A21][A22]. The application of displacement controlled systems is the subject of much research, and the complete energy saving benefits are still being understood. Rahmfeld and Ivantysynova have presented a system pairing each actuator with a dedicated four quadrant pump, allowing for energy recovery under assistive loads [A20].

Circuit designers often oversize hydraulic equipment by 10-50% to overcome unaccounted losses. This results in pumps operating away from peak operating conditions, and therefore low efficiencies. Excessive throttling also results, increasing component wear, decreasing controllability, and wasting energy. Simple efficiency gains can result by good design practise [A23].

Andruch and Lumkes have described a system design that employs a neural network to control the path of pressurized fluid from power source to load, with the ability to send fluid from the exit of one load to another. The goal is to increase system efficiency by preventing pressurized

fluid from being sent to tank over a throttling valve. Early simulations indicate 33% improvements over common spool valve topography for an excavator [A18].

The electro-hydraulic actuator system is composed of a fixed displacement pump and variable speed electric motor being directly coupled to an actuator. As fixed displacement components are more efficient than variable units, and metering valves are removed, this system has improved efficiency - especially under part-load conditions [A24][A25]. Implementation will require further work to deal with low-speed leakage and overheating of the system [A25].

A.3.2 Common Pressure Rail

Pending on the success of the IHT and similar components, common pressure rails will become more popular in future circuit design. Common pressure rails employ secondary control of the loads, drawing the energy from a high pressure reservoir common to all loads in a given system. This is similar to the operation of the electrical grid. This allows loads to be decoupled from power sources and other loads. The IHT reduces metering losses associated with stepping down pressure, while accumulators allow for energy recovery and storage [A26][A27]. Innas BV has implemented the common pressure rail design, along with their IHT and Chiron free piston engine in a small fork lift to demonstrate the capability and benefits of such a system [A28].

A.3.3 Flow Regeneration

The common procedure to lower or decelerate a load is by converting the excess energy into heat, using some sort of meter-out method or friction brakes. Circuit designers are beginning to take advantage of this energy by implementing storage circuits, designed to charge an accumulator that can provide flow in the future. Less flow requirements from the power source translates to decreased energy requirements [A29][A30]. Andic has developed a simulation tool capable of optimizing the energy recovery system, and it is predicted that up to 80% of the normally wasted energy could be stored; this is in comparison to electric units that are capable of recovering about 30% of the available energy [A31].

A.3.4 Working Fluid Selection

The standards used to select fluid grades to be used in a system are based on expected operating temperatures. Herzog et al. have suggested that these standards should be appended to take into account shear stability and energy efficiency. Many fluids experience a reduction in viscosity after a shearing load, leading to decreased performance and efficiency. Shear stable fluids are resistant to shearing loads, and ensure that a system's performance and energy consumption are optimized according to the initial design. This was demonstrated by using different oils in an excavator; fuel savings of 18% and a 6% increase in work capability were observed [A32]. There is further incentive to choose synthetic working fluids, which are known to reduce friction and are rapidly biodegradable. Efficiency improvements of 2-3% are expected over natural fluids of the same grade [A33].

A.4 Hydraulic Hybrid Vehicles

The phrase *hybrid vehicle* has traditionally been associated with the electric hybrid. They are growing in popularity and acceptance in the automotive market, offering impressive fuel economy at the cost of expensive electric motors and batteries. The electric hybrid is not the only option; hydraulic hybrid vehicles have recently undergone extensive development, and are already being integrated into medium and large sized vehicles today.

A hybrid vehicle can be defined as the combination of an internal combustion engine and a second hydraulic power source that allows for energy recovery [A34]. It is only due to recent advances in hydraulic components [A35], and the improvement and integration of computer control [A26] that are allowing hydraulic hybrid vehicles (HHVs) to become competitive in the automotive market.

A.4.1 Architectures

Three common architectures are used in hybrid vehicles: Series, Parallel, and Power-split. The goal is to minimize fuel consumption by operating the engine under its most efficient conditions. The ability to decouple the engine from the load allows for this optimal engine management.

A.4.1.1 Parallel Hybrid

A parallel hybrid is based on a conventional drive train, with the addition of a pump/motor along the existing drive shaft. The pump/motor is able to convert both excess engine power and deceleration energy into pressurized fluid, which can be stored in an accumulator. This stored energy can then be used to drive the vehicle, or provide assistive power during acceleration [A36]. While it is possible to remove the engine from the load, optimal engine management is not possible as wheel speed and engine speed are coupled [A34][A36]. Simulations of a simple parallel system over an urban drive cycle predicts 7-10% energy savings; without implementing engine-off control or optimal engine management [A37].

A.4.1.2 Series Hybrid

Series hybrid vehicles do away with the conventional drive train and instead use a hydrostatic transmission [A36][A38]. The internal combustion engine is connected to a pump, which is part of a hydraulic circuit containing a storage accumulator and drive pump/motor(s) [A36]. Optimal engine management is possible, as the engine speed can be completely decoupled from the load, operating only under peak efficiency conditions [A36][A38][A39]. Engine-off control can be used at idle, and when the accumulator has stored sufficient energy, to drive the vehicle using only the hydraulic circuit [A36].

Innas BV has developed their own *Hydrid* series hydraulic system to be used in automobiles. This system will be a fully integrated design, using the Chiron free piston engine, floating cup pumps, and IHTs in conjunction with the common pressure rail concept [A38][A39]. Simulations indicate that fuel consumption can be decreased by up to 50% without compromising performance or drivability [A39].

A.4.1.3 Power-Split Hybrid

The power-split transmission is a combination of the parallel and series architectures. The driveshaft is present and used to drive the vehicle under more efficient, high load conditions, similar to a parallel hybrid. The hydraulic system drives the wheels similar to a series hybrid, and allows the mechanical transmission to be decoupled from the drive wheels to allow for optimal engine management [A36]. Advanced controls also allow for each wheel's torque to be controlled independently, introducing for dynamic control [A34].

A.4.1.4 System Optimization

To achieve the greatest fuel economy savings from a hydraulic hybrid vehicle, the component sizing must be optimized. Literature suggests simulation tools to be of great use in sizing the components to be used in the hybrid power train. Filipi et al. provide an iterative technique optimizing component sizing. The first step is to design the system with optimal components, based on minimizing fuel use and meeting the required performance limits, followed by ensuring the operation of the system is optimum [A40].

In addition to selecting the properly sized components, it is important that control of the system enables maximum fuel savings. Digital controls have served as an enabler of hydraulic hybrids; the relatively low energy density of hydraulics require advanced control of the high power flows present in the system [A37]. A number of techniques to create the most suitable controller are presented in literature, including dynamic programming to create a set of implementable rules [A36][A41], predictive controls to attempt to have the accumulator's state of charge as low as possible before a braking event [A34], and sliding mode controllers using static programming that use engine efficiency maps to minimize fuel consumption [A42].

No matter the controller present, it is always desirable to implement engine-off control; this offers huge fuel savings over conventional vehicles [A34]. Every vehicle has different performance objectives, and as such, optimization and controller programming will be different for the various classes of vehicles to be hybridized [A36].

A.4.2 Today's Hybrids

There are a number of systems currently undergoing real-world testing and operation. Past hybrid systems have mainly focussed on heavier vehicles, such as buses [A43] and delivery vehicles. With the success of electric hybrid passenger vehicles, the hydraulics industry is also shifting to passenger car systems [A44]. Jaguar is developing a parallel system to recapture braking energy and aid in vehicle acceleration. The designers are seeking to ensure the driver of the vehicle does not compromise any control or performance, compared to the traditional vehicle [A45].

The package delivery industry is also putting hybrids on the road. UPS has been testing a full series hybrid diesel urban delivery truck, and is expecting fuel savings of 60-70% over the diesel trucks. This system is rear-wheel drive, with regenerative braking, engine-off control, and is also ABS equipped [A35]. The technology used in the UPS delivery trucks is scaleable down to smaller vehicles, noting that the energy savings will not be as high as with heavier vehicles [A46].

A.5 Conclusion

A recent focus on the improvement of energy efficiency of hydraulic components and systems is paving the way for hydraulic systems to remain relevant and competitive with other technologies. It is expected that as hydraulic components and circuits become more efficient, they will be used in more applications where they are not found today.

All of the literature reviewed has presented ideas, designs, and methodologies to ultimately reduce the amount of energy inputs required to complete a given task. Little consideration, if any, is discussed about the effect of an operator on a system's efficiency. While simulations may indicate improvements, it is uncertain whether the production system will reward the customer efficiency paybacks expected when completing a task. Inclusion of the so-called 'human factor' would be helpful in explaining the benefits and improvements to a system.

A.6 References

[A1] Ivantysynova, M. *Innovations in Pump Design - What are Future Directions?*. Proceedings of the 7th JFPS International Symposium on Fluid Power, Toyama, Japan. 2008.

[A2] Baker, J. and Ivantysynova, M., *Investigation of Power Losses in the Lubricating Gap Between the Cylinder Block and Valve Plate of Axial Piston Machines*. Proceedings of the 5th FPNI PhD Symposium, Cracow, Poland. 2008.

[A3] Achten, P. Designing the impossible pump. Innas Publication CD. 2003.

[A4] Hannifin, P. "Accumulators Deliver New Payoffs." Machine Design 80.3(2008): 46-49.

[A5] Pourmovahed, A., Baum, S.A., Fronczak, F.J., and Beachley, N.H., *Experimental Evaluation of a Hydraulic Accumulator Efficiency With and Without Elastometric Foam*. Proceedings of the 22nd Intersociety Energy Conversion Engineering Conference, Philidelphia, USA. 1987.

[A6] Godin, E. "Reduce Energy Needs with Accumulators." *Hydraulics & Pneumatics* 61.10(2008): 43-47.

[A7] Li, P. Y., Van de Ven, J. D., and Sancken, C., *Open Accumulator Concept for Compact Fluid Power Energy Storage*. Proceedings of the ASME International Mechanical Engineering Congress, Seattle, USA. 2007.

[A8] Song, L. and Yao, B., "Energy-Saving Control of Single-Rod Hydraulic Cylinders with Programmable Valves and Improved Working Mode Selection." *National Fluid Power Association and Society of Automotive Engineers.* NCFP 102- 2.4/SAE OH 202-01-1343.(2002): 81-89.

[A9] Aardema, J.A., Koehler, D.W. "System and Method for Controlling an Independent Metering Valve." United States Patent 5960695. 5 October 1999.

[A10] Tu, H., Rannow, M., Van de Ven, J., Wang, M., Li, P., Chase, T., *High Speed Rotary Pulse Width Modulated on/Off Valve*. Proceedings of the ASME International Mechanical Engineering Congress, Seattle, USA: 2007.

[A11] Achten, P., Zhao, F., Vael, G. , *Transforming Future Hydraulics: A New Design of a Hydraulic Transformer*. Proceedings of the 5th Scandinavian International Conference on Fluid Power, SICFP '97, Linkoping University, Finland. 1997.

[A12] Achten, P. A. J., van den Brink, T., van den Oever, J., Potma, J., Schellekens, M., Vael, G., van Walwijk, M., *Dedicated design of the Hydraulic Transformer*. Proceedings of the 3rd IFK, IFAS/RWTH Aachen. 2002.

[A13] Achten, P.A.J., Palmberg, J.-O. , *What a Difference a Hole Makes - The Commercial Value of the Innas Hydraulic Transformer*. Proc. of the 6th Scandinavian International Conference on Fluid Power SICFP '99, Tampere University of Technology, Finland. 1999.

[A14] Achten P. A. J., Van den Oever J. P. J., Potma J., Vael G. E. M., *Horsepower with Brains: The Design of the CHIRON Free Piston Engine.* SAE 2000-01-2545.

[A15] Hibi, A., "Fundamental Test Results of a Hydraulic Free Piston Internal Combustion Engine." *Journal of Automobile Engineering* 218.10(2004): 1149-1157.

[A16] Van de Ven, James D. "Mobile Hydraulic Power Supply: Liquid Piston Stirling Engine Pump." *Renewable energy* 34.11(2009): 2317-2322.

[A17] Zimmerman, J.; Pelosi, M.; Williamson, C.; Ivantysynova, M. *Energy Consumption of an LS Excavator Hydraulic System*, Proceedings of 2007 ASME International Mechanical Engineering Congress & Exposition, IMECE2007, Seattle, USA. 2007.

[A18] Andruch, J. and Lumkes, J., *A Hydraulic System Topography with Integrated Energy Recovery and Reconfigurable Flow Paths Using High Speed Valves*. Proceedings of the 51st National Conference on Fluid Power (NCFP), Las Vegas, USA. 2008.

[A19] Zimmerman, J. and Ivantysynova, M., *The Effect of System Pressure Level on the Energy Consumption of Displacement Controlled Actuator Systems*. Proceedings of the 5th FPNI Ph.D. Symposium, Cracow, Poland. 2008.

[A20] Rahmfeld, R. and Ivantysynova, M., *Energy saving hydraulic actuators for mobile machines*. Proceedings of the 1st Bratislavian Fluid Power Symposium, Casta-Pila, Slovakia. 1998.

[A21] Rahmfeld, R. and Ivantysynova, M., *Displacement controlled linear actuator with differential cylinder- a way to save primary energy in mobile machines*. Fifth International Conference on Fluid Power Transmission and Control, Hangzhou, China. 2001.

[A22] Murrenhoff, H. "Trends and some recent developments in mobile hydraulics." *Ventil* 13.6(2007): 392-401.

[A23] Sahoo, T. "Energy Cost Savings with Centrifugal Pumps." *World Pumps* 2009.510(2009): 35-37.

[A24] Ivantysynova, M., Kunze, O., Berg, H., *Energy Saving Hydraulic Systems in Aircraft: a Way to Save Fuel*. Proceedings of the 4th Scandinavian International Conference on Fluid Power, Tampere, Finland. 1995.

[A25] Helduser, S., "Electric-hydrostatic Drive- An Innovative Energy-saving Power and Motion Control System." *Journal of Systems and Control Engineering* 213.5(1999): 427-437.

[A26] Rydberg, K.-E., *Concepts and Development Trends for Efficiency Improvement of Hydrostatics in Mobile Applications*. SAE OH 2002-01-1422.

[A27] Vael, G., Achten, P., Fu, Z., *The Innas Hydraulic Transformer: The key to the hydrostatic Common Pressure Rail.* SAE 2000-01-2561.

[A28] Vael, G.E.M., Achten, P.A.J., *The Innas Fork Lift Truck, Working Under Constant Pressure.* Proceedings of the 1st IFK, IFAS/RWTH Aachen. 1998.

[A29] Wendel, G.R., *Regenerative Hydraulic Systems for Increased Efficiency*, Southwest Research Institute. 2000.

[A30] Wendel, G.R. *Hydraulic System Configurations for Improved Efficiency.* SAE 2002-01-1433.

[A31] Andic, S. *Saving and Recovery of Braking Power*. Proceedings of the 15th IASTED International Conference, Rhodes, Greece. 2006.

[A32] Herzog, S., Marougy, T., and Michael, P. *Guidelines for Hydraulic Fluid Viscosity Selection to Improve Equipment Fuel Economy and Productivity*. Proceedings of the 51st National Conference on Fluid Power, Las Vegas, USA. 2008.

[A33] Lea, C. "Energy Savings Through Use of Advanced Biodegradable Lubricants." *Industrial Lubrication and Tribology* 59.3(2007): 132-136.

[A34] Van de Ven, J.D., Olson, M. and Li, P.Y. *Development of a Hydro-Mechanical Hydraulic Hybrid Drive Train with Independent Wheel Torque Control for an Urban Passenger Vehicle*. International Fluid Power Exposition, Las Vegas, USA. 2008.

[A35] Hall, R. "Hydraulic hybrid promises big savings for UPS." *Hydraulics & Pneumatics* 59.10(2006): 42-5.

[A36] Meyer, J. J., Stelson, K.A., Hencey, B. and Alleyne, A.G. *Optimization of the Power Management Strategy for a Hydraulic Hybrid Vehicle*. Fifth Fluid Power Net International Ph.D. Symposium Proceedings, Krakow, Poland. 2008.

[A37] Toulson, E.R. *Evaluation of a Hybrid Hydraulic Launch Assist System for use in Small Road Vehicles*. Industrial Electronics, 2008 IEEE International Symposium on Industrial Electionics, Cambridge, UK. 2008.

[A38] Achten, P. *Changing the Paradigm*. Proceedings of the Tenth Scandinavian International Conference on Fluid Power, SICFP'07, Tampere, Finland. 2007.

[A39] Achten, P., Vael, G., Hubertus, M., Kohmascher, T., Inderelst, M. "Low-emission Hydraulic Hybrid for Passenger Cars." *Automobiltechnische Zeitschrift (ATZ)* 111(2009): 378-384.

[A40] Filipi, Z.; Loucas, L.; Daran, B.; Lin, C-C.; Yildir, U.; Wu, B.; Kokkolaras, M.; Assanis, D.; Peng, H.; Papalambros, P.; Stein, J.; Szkubiel, D.; Chapp, R. "Combined Optimization of Design and Power Management of the Hydraulic Hybrid Propulsion System for the 6 x 6 Medium Truck." *International Journal of Heavy Vehicle Systems* 11(2004): 372-402.

[A41] Wu, B.; Lin, C.; Filipi, Z.; Peng, H.; Assanis, D. "Optimal Power Management for a Hydraulic Hybrid Delivery Truck." *Vehicle System Dynamics* 42(2004): 23-40.

[A42] Williams, K. and Ivantysynova, M. *Towards an Optimal Energy Management Strategy for Hybrid Hydraulic Powertrains Based on Dual Stage Power Split Principle*. Proceedings of the 5th FPNI Ph.D. Symposium, Cracow, Poland. 2008.

[A43] Fronczak, F. J., and Beachley, N. H. , *An Integrated Hydraulic Drive Train System for Automobiles*. Fluid Power 8, Proceedings of the 8th International Symposium on Fluid Power, Bimingham, England. 1988.

[A44] Ogando, J. "No Batteries Required." *Design News* 63.6(2008): 45-46.

[A45] Pierce, Julia. "Powerful Brake-through." *The Engineer* 292.7629(2003): 8.

[A46] "Eaton uses Hydraulics for Hybrid." *Automotive Engineering International* 114.10(2006): 20.

Appendix B: Detailed Kinematic Relationships

The objective of this appendix is to provide a complete set of detailed kinematic relationships used in modeling the John Deere (JD) 410G backhoe workgroup. The kinematic equations are composed of the position, velocity, and acceleration portions; each will be shown separately in this appendix.

B.1.1 Coordinate System and Modeling Points

The coordinate system used in modeling the kinematics of the JD 410G backhoe is shown in Figure B.1. The Cartesian coordinate system uses two angles, θ and ϕ, and the distance between two points (labeled 'A' and 'B' in Figure B.1) to represent the magnitude and orientation of any vector in space.

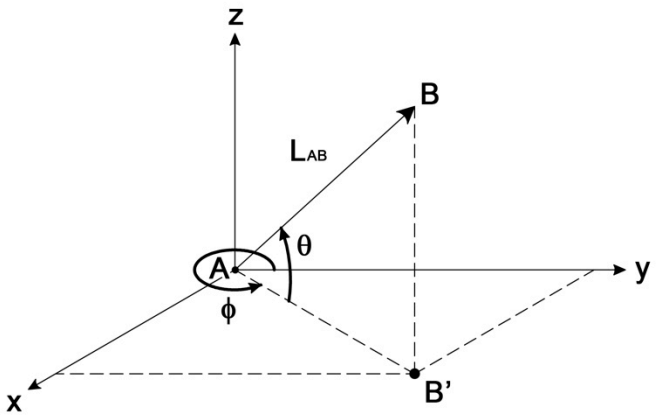

Figure B.1 Cartesian Coordinate System Selected for Modeling

The angle, ϕ, is used to describe the swing angle of the vector, measured in the counterclockwise direction from the positive y-axis. As all the components of the backhoe workgroup are contained in a single plane that is rotated by the swing function, the swing angle, ϕ, will be the same for all vectors modeled in the system. The angle θ is measured counterclockwise between the linkage and its projection on to the ground plane (the vector between point A and B' in Figure B.1). For a given linkage joining two points, for example, points A and B, the magnitude

of the vector is defined as L_{AB}, where the first subscript denotes the starting point of the vector, and the second denotes the end point.

B.1.2 Backhoe Kinematic Modeling Points and Angles

The JD 410G backhoe workgroup is composed of 11 pinned connections that have been selected as the modeling points for the system. The points are labeled using an alphabetic notation, and are shown in Figure B.2. The system orientation shown in Figure B.2 is viewed in a plane perpendicular to the swing angle, ϕ, of the system.

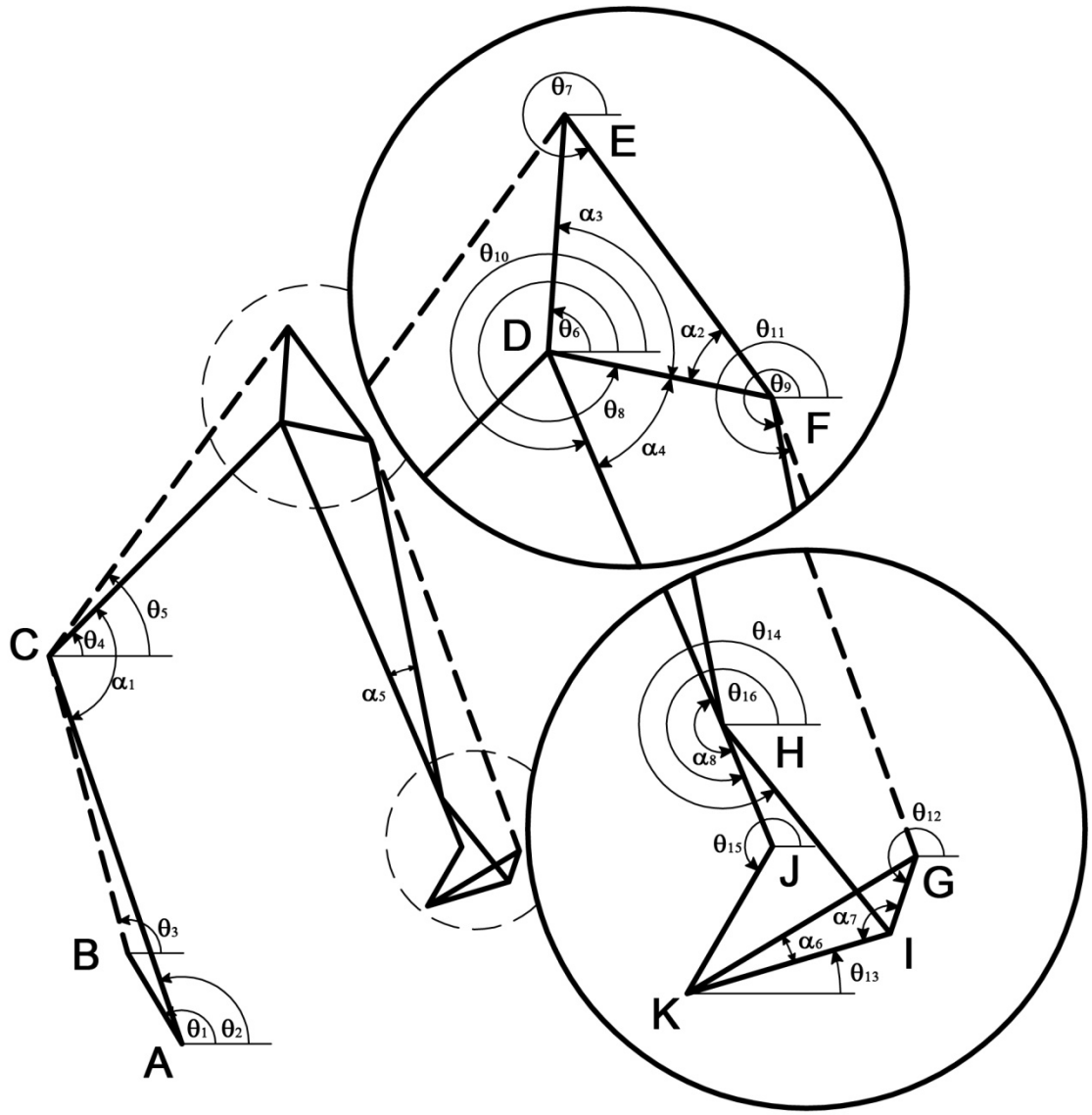

Figure B.2 CAD Representation of the Backhoe Modeling Points and Angles

B.2 Position Analysis

The position analysis is used to determine the orientation of the system for a given set of hydraulic actuator lengths. The method of position loops and Newton's method is discussed in the main body of the thesis and will not be reiterated here; rather, the three systems of equations solved will be presented.

B.2.1 Position Loop created by Points A, B, and C

The position loop created by points A, B, and C is first solved to determine the value of angles θ_2 and θ_3. The path around loop A-B-C is written in its $\hat{\imath}$ and $\hat{k}$ components as

$$\hat{\imath}: f_1 = L_{AB}cos\theta_1 + L_{BC}cos\theta_3 - L_{AC}cos\theta_2 \text{ , and} \quad [B.1]$$

$$\hat{k}: f_2 = L_{AB}sin\theta_1 + L_{BC}sin\theta_3 - L_{AC}sin\theta_2 , \quad [B.2]$$

where:

$f_1, f_2 =$ The net change in position in the $\hat{\imath}$ and $\hat{k}$ directions as a path is traced around loop A-B-C $[m]$.

Noting that the path around the loop should result in no net change in position, Equations B.1 and B.2 are satisfied when

$$F_1 = \begin{bmatrix} f_1 \\ f_2 \end{bmatrix} = \begin{bmatrix} 0 \\ 0 \end{bmatrix}. \quad [B.3]$$

Given that the only variables that are free to change are θ_2 and θ_3, Newton's method for a system of equations is used to find the exact values of θ_2 and θ_3. Defining the initial guess to be

$$\vartheta_{guess} = \begin{bmatrix} \theta_2 \\ \theta_3 \end{bmatrix}, \quad [B.4]$$

And the Jacobian as

$$J_1 = \begin{bmatrix} {\partial f_1}/{\partial \theta_2} & {\partial f_1}/{\partial \theta_3} \\ {\partial f_2}/{\partial \theta_2} & {\partial f_2}/{\partial \theta_3} \end{bmatrix} = \begin{bmatrix} L_{AC}sin\theta_2 & -L_{BC}sin\theta_3 \\ -L_{AC}cos\theta_2 & L_{BC}cos\theta_3 \end{bmatrix}, \quad [B.5]$$

allows the change in the initial guess to be calculated from

$$\Delta\vartheta = -[J_1]^{-1}F_1. \quad [B.6]$$

The quantity of $\Delta\vartheta$ can be used to adjust the initial guess to provide an improvement to Equation B.3, forcing F_1 closer to zero, such that

$$\vartheta_{next\ guess} = \vartheta_{guess} + \Delta\vartheta. \quad [B.7]$$

This process is repeated until the magnitude of $\Delta\vartheta$ is such that it no longer has a substantial effect on subsequent approximations of $\vartheta_{next\ guess}$. For this simulation, the value of $\vartheta_{next\ guess}$ is taken to be exact when both elements of $\Delta\vartheta$ are less than 0.00573° (0.0001 radians). This process provides an exact solution for θ_2 and θ_3.

Finally, the value of θ_4 is calculated using geometry, such that

$\theta_4 = \theta_2 + \alpha_1 - \pi$. [B.8]

B.2.2 Position Loop created by Points C, D, and E

The position loop created by points C, D, and E is next used to determine the value of angles θ_5 and θ_6. The path around loop C-D-E is written in its $\hat{\imath}$ and $\hat{k}$ components as

$$\hat{\imath}: f_3 = L_{CD}cos\theta_4 + L_{DE}cos\theta_6 - L_{CE}cos\theta_5 \text{ , and} \quad [B.9]$$

$$\hat{k}: f_4 = L_{CD}sin\theta_4 + L_{DE}sin\theta_6 - L_{CE}sin\theta_5 . \quad [B.10]$$

In this case, the only variables that are free to change are θ_5 and θ_6. Newton's method for a system of equations is used to find the exact values of θ_5 and θ_6. Defining the initial guess to be

$$\vartheta_{guess} = \begin{bmatrix}\theta_5 \\ \theta_6\end{bmatrix}, \quad [B.11]$$

and the Jacobian as

$$J_2 = \begin{bmatrix} L_{CE}sin\theta_5 & -L_{DE}sin\theta_6 \\ -L_{CE}cos\theta_5 & L_{DE}cos\theta_6 \end{bmatrix}, \quad [B.12]$$

allows the same process to be used to find the exact values for θ_5 and θ_6. Using the values of θ_5 and θ_6, the following geometrical relationships are used to calculate additional angles

$$\theta_7 = 2\pi - \alpha_2 - \alpha_3 + \theta_6, \quad [B.13]$$

$$\theta_8 = 2\pi - \alpha_3 + \theta_6, \quad [B.14]$$

$$\theta_9 = \theta_8 - \alpha_4 - \alpha_5, \quad [B.15]$$

$$\theta_{10} = \theta_8 - \alpha_4, \text{and} \quad [B.16]$$

$$\theta_{16} = \theta_{10} - \alpha_8. \quad \text{[B.17]}$$

B.2.3 Four-bar Linkage Position Loops

The final position loop contains two dependent sets of equations to be solved simultaneously. The first half of the equations are developed from loop H, I, K, and J, while the other half of the equations come from loop F, G, I, and H. The paths around the loops give

$$\hat{k}\text{: } f_4 = L_{HI}sin\theta_{14} - L_{IK}sin\theta_{13} - L_{JK}sin\theta_{15} - L_{HJ}sin\theta_{16}, \quad \text{[B.18]}$$

$$\hat{\imath}\text{: } f_5 = L_{HI}cos\theta_{14} - L_{IK}cos\theta_{13} - L_{JK}cos\theta_{15} - L_{HJ}cos\theta_{16}, \quad \text{[B.19]}$$

$$\hat{k}\text{: } f_6 = L_{FG}sin\theta_{11} - L_{GI}sin\theta_{GI} - L_{HI}sin\theta_{14} - L_{FH}sin\theta_9, \text{ and} \quad \text{[B.20]}$$

$$\hat{\imath}\text{: } f_7 = L_{FG}cos\theta_{11} - L_{GI}cos\theta_{GI} - L_{HI}cos\theta_{14} - L_{FH}cos\theta_9, \quad \text{[B.21]}$$

where:

$$\theta_{GI} = \pi - \alpha_7 + \theta_{13}. \quad \text{[B.22]}$$

In this case, θ_{11}, θ_{13}, θ_{14} and θ_{15} are free to change. Newton's method for a system of equations is used to find the exact values θ_{11}, θ_{13}, θ_{14} and θ_{15}. Defining the initial guess to be

$$\vartheta_{guess} = \begin{bmatrix} \theta_{11} \\ \theta_{13} \\ \theta_{14} \\ \theta_{15} \end{bmatrix}, \quad \text{[B.23]}$$

and the Jacobian as

$$J_3 = \begin{bmatrix} 0 & -L_{IK}\cos\theta_{13} & L_{HI}\cos\theta_{14} & -L_{JK}cos\theta_{15} \\ 0 & L_{IK}\sin\theta_{13} & -L_{HI}\sin\theta_{14} & L_{JK}sin\theta_{15} \\ L_{FG}\cos\theta_{11} & -L_{GI}cos\theta_{GI} & -L_{HI}\cos\theta_{14} & 0 \\ -L_{FG}\sin\theta_{11} & L_{GI}sin\theta_{GI} & L_{HI}\sin\theta_{14} & 0 \end{bmatrix}, \quad \text{[B.24]}$$

allows the exact values for θ_{11}, θ_{13}, θ_{14} and θ_{15} to be calculated. The value of θ_{12} is found using the geometrical relationship

$$\theta_{12} = \pi + \alpha_6 + \theta_{13}. \quad \text{[B.25]}$$

B.3 Relative Velocity Equations

After the orientation of the workgroup is solved, the velocity of each modeling point can be found using the following relationships:

$$V_{Cx} = V_{Bx} - V_{Boom} cos\theta_3 sin\phi + L_{BC}\left(\frac{d\theta_3}{dt}\sin\theta_3 \sin\phi - \frac{d\phi}{dt}\cos\theta_3 \cos\phi\right), \quad [B.26]$$

$$V_{Cy} = V_{By} + V_{Boom} cos\theta_3 cos\phi + L_{BC}\left(-\frac{d\theta_3}{dt}\sin\theta_3 \cos\phi - \frac{d\phi}{dt}\cos\theta_3 \sin\phi\right), \quad [B.27]$$

$$V_{Cz} = V_{Boom} sin\theta_3 + L_{BC}\left(\frac{d\theta_3}{dt}\cos\theta_3\right), \quad [B.28]$$

$$V_{Cx} = V_{Ax} + L_{AC}\left(\frac{d\theta_2}{dt}\sin\theta_2 \sin\phi - \frac{d\phi}{dt}\cos\theta_2 \cos\phi\right), \quad [B.29]$$

$$V_{Cy} = V_{Ay} + L_{AC}\left(-\frac{d\theta_2}{dt}\sin\theta_2 \cos\phi - \frac{d\phi}{dt}\cos\theta_2 \sin\phi\right), \text{ and} \quad [B.30]$$

$$V_{Cz} = L_{AC}\left(\frac{d\theta_2}{dt}\cos\theta_2\right). \quad [B.31]$$

**Equations B.26-B.31 are solved using matrix inversion to solve for $V_{Cx}, V_{Cy}, V_{Cz}, \frac{d\theta_2}{dt}$, and $\frac{d\theta_3}{dt}$.*

$$V_{Dx} = V_{Cx} + L_{CD}\left(\frac{d\theta_4}{dt}\sin\theta_4 \sin\phi - \frac{d\phi}{dt}\cos\theta_4 \cos\phi\right), \quad [B.32]$$

$$V_{Dy} = V_{Cy} + L_{CD}\left(-\frac{d\theta_4}{dt}\sin\theta_4 \cos\phi - \frac{d\phi}{dt}\cos\theta_4 \sin\phi\right), \quad [B.33]$$

$$V_{Dz} = L_{CD}\left(\frac{d\theta_4}{dt}\cos\theta_4\right), \quad [B.34]$$

$$V_{Ex} = V_{Cx} - V_{Stick} cos\theta_5 sin\phi + L_{CE}\left(\frac{d\theta_5}{dt}\sin\theta_5 \sin\phi - \frac{d\phi}{dt}\cos\theta_5 \cos\phi\right), \quad [B.35]$$

$$V_{Ey} = V_{Cy} + V_{Stick} cos\theta_5 cos\phi + L_{CE}\left(-\frac{d\theta_5}{dt}\sin\theta_5 \cos\phi - \frac{d\phi}{dt}\cos\theta_5 \sin\phi\right), \quad [B.36]$$

$$V_{Ez} = V_{Cz} + V_{Stick} sin\theta_5 + L_{CE}\left(\frac{d\theta_5}{dt}\cos\theta_5\right), \quad [B.37]$$

$$V_{Ex} = V_{Dx} + L_{DE}\left(\frac{d\theta_6}{dt}\sin\theta_6 \sin\phi - \frac{d\phi}{dt}\cos\theta_6 \cos\phi\right), \quad [B.38]$$

$$V_{Ey} = V_{Dy} + L_{DE}\left(-\frac{d\theta_6}{dt}\sin\theta_6 \cos\phi - \frac{d\phi}{dt}\cos\theta_6 \sin\phi\right), \text{ and} \quad [B.39]$$

$$V_{Ez} = V_{Dz} + L_{DE}\left(\frac{d\theta_6}{dt}\cos\theta_6\right). \quad [B.40]$$

**Equations B.35-B.40 are solved using matrix inversion to solve for $V_{Ex}, V_{Ey}, V_{Ez}, \frac{d\theta_5}{dt}$, and $\frac{d\theta_6}{dt}$.*

$$V_{Fx} = V_{Dx} + L_{DF}\left(\frac{d\theta_6}{dt}\sin\theta_8 \sin\phi - \frac{d\phi}{dt}\cos\theta_8 \cos\phi\right), \quad [B.41]$$

$$V_{Fy} = V_{Dy} + L_{DF}\left(-\frac{d\theta_6}{dt}\sin\theta_8 \cos\phi - \frac{d\phi}{dt}\cos\theta_8 \sin\phi\right), \quad [B.42]$$

$$V_{Fz} = V_{Dz} + L_{DF}\left(\frac{d\theta_6}{dt}\cos\theta_8\right), \quad [B.43]$$

$$V_{Hx} = V_{Dx} + L_{DH}\left(\frac{d\theta_6}{dt}\sin\theta_{16}\sin\phi - \frac{d\phi}{dt}\cos\theta_{16}\cos\phi\right), \quad [B.44]$$

$$V_{Hy} = V_{Dy} + L_{DH}\left(-\frac{d\theta_6}{dt}\sin\theta_{16}\cos\phi - \frac{d\phi}{dt}\cos\theta_{16}\sin\phi\right), \quad [B.45]$$

$$V_{Hz} = V_{Dz} + L_{DH}\left(\frac{d\theta_6}{dt}\cos\theta_{16}\right), \quad [B.46]$$

$$V_{Jx} = V_{Hx} + L_{HJ}\left(\frac{d\theta_6}{dt}\sin\theta_{10}\sin\phi - \frac{d\phi}{dt}\cos\theta_{10}\cos\phi\right), \quad [B.47]$$

$$V_{Jy} = V_{Hy} + L_{HJ}\left(-\frac{d\theta_6}{dt}\sin\theta_{10}\cos\phi - \frac{d\phi}{dt}\cos\theta_{10}\sin\phi\right), \quad [B.48]$$

$$V_{Jz} = V_{Hz} + L_{HJ}\left(\frac{d\theta_6}{dt}\cos\theta_{10}\right), \quad [B.49]$$

$$V_{Gx} = V_{Fx} - V_{Bucket}cos\theta_{11}sin\phi + L_{FG}\left(\frac{d\theta_{11}}{dt}\sin\theta_{11}\sin\phi - \frac{d\phi}{dt}\cos\theta_{11}\cos\phi\right), \quad [B.50]$$

$$V_{Gy} = V_{Fy} + V_{Bucket}cos\theta_{11}cos\phi + L_{FG}\left(-\frac{d\theta_{11}}{dt}\sin\theta_{11}\cos\phi - \frac{d\phi}{dt}\cos\theta_{11}\sin\phi\right), \quad [B.51]$$

$$V_{Gz} = V_{Fz} + V_{Bucket}sin\theta_{11} + L_{FG}\left(\frac{d\theta_{11}}{dt}\cos\theta_{11}\right), \quad [B.52]$$

$$V_{Kx} = V_{Gx} + L_{GK}\left(\frac{d\theta_{12}}{dt}\sin\theta_{12}\sin\phi - \frac{d\phi}{dt}\cos\theta_{12}\cos\phi\right), \quad [B.53]$$

$$V_{Ky} = V_{Gy} + L_{GK}\left(-\frac{d\theta_{12}}{dt}\sin\theta_{12}\cos\phi - \frac{d\phi}{dt}\cos\theta_{12}\sin\phi\right), \quad [B.54]$$

$$V_{Kz} = V_{Gz} + L_{GK}\left(\frac{d\theta_{12}}{dt}\cos\theta_{12}\right), \quad [B.55]$$

$$V_{Ix} = V_{Kx} + L_{IK}\left(\frac{d\theta_{13}}{dt}\sin\theta_{13}\sin\phi - \frac{d\phi}{dt}\cos\theta_{13}\cos\phi\right), \quad [B.56]$$

$$V_{Iy} = V_{Ky} + L_{IK}\left(-\frac{d\theta_{13}}{dt}\sin\theta_{13}\cos\phi - \frac{d\phi}{dt}\cos\theta_{13}\sin\phi\right), \quad [B.57]$$

$$V_{Iz} = V_{Kz} + L_{IK}\left(\frac{d\theta_{13}}{dt}\cos\theta_{13}\right), \quad [B.58]$$

$$V_{Ix} = V_{Hx} + L_{HI}\left(\frac{d\theta_{14}}{dt}\sin\theta_{14}\sin\phi - \frac{d\phi}{dt}\cos\theta_{14}\cos\phi\right), \quad [B.59]$$

$$V_{Iy} = V_{Hy} + L_{HI}\left(-\frac{d\theta_{14}}{dt}\sin\theta_{14}\cos\phi - \frac{d\phi}{dt}\cos\theta_{14}\sin\phi\right), \quad [B.60]$$

$$V_{Iz} = V_{Hz} + L_{HI}\left(\frac{d\theta_{14}}{dt}\cos\theta_{14}\right), \quad [B.61]$$

$$V_{Kx} = V_{Jx} + L_{JK}\left(\frac{d\theta_{15}}{dt}\sin\theta_{15}\sin\phi - \frac{d\phi}{dt}\cos\theta_{15}\cos\phi\right), \quad [B.62]$$

$$V_{Ky} = V_{Jy} + L_{JK}\left(-\frac{d\theta_{15}}{dt}\sin\theta_{15}\cos\phi - \frac{d\phi}{dt}\cos\theta_{15}\sin\phi\right), \text{ and} \quad [B.63]$$

$$V_{Kz} = V_{Jz} + L_{JK}\left(\frac{d\theta_{15}}{dt}\cos\theta_{15}\right). \quad [B.64]$$

**Equations B.50-B.64 are solved using matrix inversion to solve for* $V_{Gx}, V_{Gy}, V_{Gz}, V_{Kx}, V_{Ky}, V_{Kz}, V_{Ix}, V_{Iy}, V_{Iz}, \frac{d\theta_{11}}{dt}, \frac{d\theta_{12}}{dt}, \frac{d\theta_{14}}{dt}, and\ \frac{d\theta_{15}}{dt}$.

B.4 Relative Acceleration Equations

The following equations are used in the acceleration analysis for the backhoe workgroup:

$$A_{Cx} = A_{Bx} - A_{Boom}cos\theta_3 sin\phi + 2V_{Boom}\left[\frac{d\theta_3}{dt}sin\theta_3 sin\phi - \frac{d\phi}{dt}cos\theta_3 cos\phi\right] +$$

$$L_{BC}\left[\frac{d^2\theta_3}{dt^2}sin\theta_3 sin\phi - \frac{d^2\phi}{dt^2}cos\theta_3 cos\phi + \left[\left(\frac{d\theta_3}{dt}\right)^2 + \left(\frac{d\phi}{dt}\right)^2\right]cos\theta_3 sin\phi + 2\frac{d\theta_3}{dt}\frac{d\phi}{dt}sin\theta_3 cos\phi\right], \quad [B.65]$$

$$A_{Cy} = A_{By} + A_{Boom}cos\theta_3 cos\phi + 2V_{Boom}\left[-\frac{d\theta_3}{dt}sin\theta_3 cos\phi - \frac{d\phi}{dt}cos\theta_3 sin\phi\right] +$$

$$L_{BC}\left[-\frac{d^2\theta_3}{dt^2}sin\theta_3 cos\phi - \frac{d^2\phi}{dt^2}cos\theta_3 sin\phi - \left[\left(\frac{d\theta_3}{dt}\right)^2 + \left(\frac{d\phi}{dt}\right)^2\right]cos\theta_3 cos\phi +$$

$$2\frac{d\theta_3}{dt}\frac{d\phi}{dt}sin\theta_3 sin\phi\right], \quad [B.66]$$

$$A_{Cz} = A_{Boom}sin\theta_3 + 2V_{Boom}\frac{d\theta_3}{dt}cos\theta_3 + L_{BC}\frac{d^2\theta_3}{dt^2}cos\theta_3 - L_{BC}\left(\frac{d\theta_3}{dt}\right)^2 sin\theta_3, \quad [B.67]$$

$$A_{Cx} = A_{Ax} + L_{AC}\left[\frac{d^2\theta_2}{dt^2}sin\theta_2 sin\phi - \frac{d^2\phi}{dt^2}cos\theta_2 cos\phi + \left[\left(\frac{d\theta_2}{dt}\right)^2 + \left(\frac{d\phi}{dt}\right)^2\right]cos\theta_2 sin\phi +$$

$$2\frac{d\theta_2}{dt}\frac{d\phi}{dt}sin\theta_2 cos\phi\right], \quad [B.68]$$

$$A_{Cy} =$$

$$A_{Ay} +$$

$$L_{AC}\left[-\frac{d^2\theta_2}{dt^2}sin\theta_2 cos\phi - \frac{d^2\phi}{dt^2}cos\theta_2 sin\phi - \left[\left(\frac{d\theta_2}{dt}\right)^2 + \left(\frac{d\phi}{dt}\right)^2\right]cos\theta_2 cos\phi +$$

$$2\frac{d\theta_2}{dt}\frac{d\phi}{dt}sin\theta_2 sin\phi\right], \text{ and} \quad [B.69]$$

$$A_{Cz} = L_{BC}\left[\frac{d^2\theta_2}{dt^2}cos\theta_2 - \left(\frac{d\theta_2}{dt}\right)^2 sin\theta_2\right]. \quad [B.70]$$

**Equations B.65-B.70 are solved using matrix inversion to solve for* $A_{Cx}, A_{Cy}, A_{Cz}, \frac{d^2\theta_2}{dt^2}, and\ \frac{d^2\theta_3}{dt^2}$.

$$A_{Dx} = A_{Cx} + L_{CD}\left[\frac{d^2\theta_4}{dt^2}sin\theta_4 sin\phi - \frac{d^2\phi}{dt^2}cos\theta_4 cos\phi + \left[\left(\frac{d\theta_4}{dt}\right)^2 + \left(\frac{d\phi}{dt}\right)^2\right]cos\theta_4 sin\phi + 2\frac{d\theta_4}{dt}\frac{d\phi}{dt}sin\theta_4 cos\phi\right], \quad [B.71]$$

$$A_{Dy} = A_{Cy} + L_{CD}\left[-\frac{d^2\theta_4}{dt^2}sin\theta_4 cos\phi - \frac{d^2\phi}{dt^2}cos\theta_4 sin\phi - \left[\left(\frac{d\theta_4}{dt}\right)^2 + \left(\frac{d\phi}{dt}\right)^2\right]cos\theta_4 cos\phi + 2\frac{d\theta_4}{dt}\frac{d\phi}{dt}sin\theta_4 sin\phi\right], \quad [B.72]$$

$$A_{Dz} = A_{Cz} + L_{CD}\left[\frac{d^2\theta_4}{dt^2}cos\theta_4 - \left(\frac{d\theta_4}{dt}\right)^2 sin\theta_4\right], \quad [B.73]$$

$$A_{Ex} = A_{Cx} - A_{Stick}cos\theta_5 sin\phi + 2V_{Stick}\left[\frac{d\theta_5}{dt}sin\theta_5 sin\phi - \frac{d\phi}{dt}cos\theta_5 cos\phi\right] + L_{CE}\left[\frac{d^2\theta_5}{dt^2}sin\theta_5 sin\phi - \frac{d^2\phi}{dt^2}cos\theta_5 cos\phi + \left[\left(\frac{d\theta_5}{dt}\right)^2 + \left(\frac{d\phi}{dt}\right)^2\right]cos\theta_5 sin\phi + 2\frac{d\theta_5}{dt}\frac{d\phi}{dt}sin\theta_5 cos\phi\right], \quad [B.74]$$

$$A_{Ey} = A_{Cy} + A_{Stick}cos\theta_5 cos\phi + 2V_{Stick}\left[-\frac{d\theta_5}{dt}sin\theta_5 cos\phi - \frac{d\phi}{dt}cos\theta_5 sin\phi\right] + L_{CE}\left[-\frac{d^2\theta_5}{dt^2}sin\theta_5 cos\phi - \frac{d^2\phi}{dt^2}cos\theta_5 sin\phi - \left[\left(\frac{d\theta_5}{dt}\right)^2 + \left(\frac{d\phi}{dt}\right)^2\right]cos\theta_5 cos\phi + 2\frac{d\theta_5}{dt}\frac{d\phi}{dt}sin\theta_5 sin\phi\right], \quad [B.75]$$

$$A_{Ez} = A_{Cz} + A_{Stick}sin\theta_5 + 2V_{Stick}\frac{d\theta_5}{dt}cos\theta_5 + L_{CE}\frac{d^2\theta_5}{dt^2}cos\theta_5 - L_{CE}\left(\frac{d\theta_5}{dt}\right)^2 sin\theta_5, \quad [B.76]$$

$$A_{Ex} = A_{Dx} + L_{ED}\left[\frac{d^2\theta_6}{dt^2}sin\theta_6 sin\phi - \frac{d^2\phi}{dt^2}cos\theta_6 cos\phi + \left[\left(\frac{d\theta_6}{dt}\right)^2 + \left(\frac{d\phi}{dt}\right)^2\right]cos\theta_6 sin\phi + 2\frac{d\theta_6}{dt}\frac{d\phi}{dt}sin\theta_6 cos\phi\right], \quad [B.77]$$

$$A_{Ey} = A_{Dy} + L_{ED}\left[-\frac{d^2\theta_6}{dt^2}sin\theta_6 cos\phi - \frac{d^2\phi}{dt^2}cos\theta_6 sin\phi - \left[\left(\frac{d\theta_6}{dt}\right)^2 + \left(\frac{d\phi}{dt}\right)^2\right]cos\theta_6 cos\phi + 2\frac{d\theta_6}{dt}\frac{d\phi}{dt}sin\theta_6 sin\phi\right], \text{ and} \quad [B.78]$$

$$A_{Ez} = A_{Dz} + L_{ED}\left[\frac{d^2\theta_6}{dt^2}cos\theta_6 - \left(\frac{d\theta_6}{dt}\right)^2 sin\theta_6\right]. \quad [B.79]$$

**Equations B.74-B.79 are solved using matrix inversion to solve for $A_{Ex}, A_{Ey}, A_{Ez}, \frac{d^2\theta_5}{dt^2}, and\ \frac{d^2\theta_6}{dt^2}$.*

$$A_{Fx} = A_{Dx} + L_{DF}\left[\frac{d^2\theta_6}{dt^2}sin\theta_8 sin\phi - \frac{d^2\phi}{dt^2}cos\theta_8 cos\phi + \left[\left(\frac{d\theta_6}{dt}\right)^2 + \left(\frac{d\phi}{dt}\right)^2\right]cos\theta_8 sin\phi + 2\frac{d\theta_6}{dt}\frac{d\phi}{dt}sin\theta_8 cos\phi\right], \quad [B.80]$$

$$A_{Fy} = A_{Dy} + L_{DF}\left[-\frac{d^2\theta_6}{dt^2}sin\theta_8 cos\phi - \frac{d^2\phi}{dt^2}cos\theta_8 sin\phi - \left[\left(\frac{d\theta_6}{dt}\right)^2 + \left(\frac{d\phi}{dt}\right)^2\right]cos\theta_8 cos\phi + 2\frac{d\theta_6}{dt}\frac{d\phi}{dt}sin\theta_8 sin\phi\right], \quad [B.81]$$

$$A_{Fz} = A_{Dz} + L_{DF}\left[\frac{d^2\theta_6}{dt^2}cos\theta_8 - \left(\frac{d\theta_6}{dt}\right)^2 sin\theta_8\right], \quad [B.82]$$

$$A_{Hx} = A_{Dx} + L_{DH}\left[\frac{d^2\theta_6}{dt^2}sin\theta_{10} sin\phi - \frac{d^2\phi}{dt^2}cos\theta_{10} cos\phi + \left[\left(\frac{d\theta_6}{dt}\right)^2 + \left(\frac{d\phi}{dt}\right)^2\right]cos\theta_{10} sin\phi + 2\frac{d\theta_6}{dt}\frac{d\phi}{dt}sin\theta_{10} cos\phi\right], \quad [B.83]$$

$$A_{Hy} =$$

$$A_{Dy} + L_{DH}\left[-\frac{d^2\theta_6}{dt^2}sin\theta_{10}cos\phi - \frac{d^2\phi}{dt^2}cos\theta_{10}sin\phi - \left[\left(\frac{d\theta_6}{dt}\right)^2 + \left(\frac{d\phi}{dt}\right)^2\right]cos\theta_{10}cos\phi + 2\frac{d\theta_6}{dt}\frac{d\phi}{dt}sin\theta_{10}sin\phi\right], \quad [B.84]$$

$$A_{Hz} = A_{Dz} + L_{DH}\left[\frac{d^2\theta_6}{dt^2}cos\theta_{10} - \left(\frac{d\theta_6}{dt}\right)^2 sin\theta_{106}\right], \quad [B.85]$$

$$A_{Jx} =$$

$$A_{Hx} + L_{HJ}\left[\frac{d^2\theta_6}{dt^2}sin\theta_{16}sin\phi - \frac{d^2\phi}{dt^2}cos\theta_{16}cos\phi + \left[\left(\frac{d\theta_6}{dt}\right)^2 + \left(\frac{d\phi}{dt}\right)^2\right]cos\theta_{16}sin\phi + 2\frac{d\theta_6}{dt}\frac{d\phi}{dt}sin\theta_{16}cos\phi\right], \quad [B.86]$$

$$A_{Jy} =$$

$$A_{Hy} + L_{HJ}\left[-\frac{d^2\theta_6}{dt^2}sin\theta_{16}cos\phi - \frac{d^2\phi}{dt^2}cos\theta_{16}sin\phi - \left[\left(\frac{d\theta_6}{dt}\right)^2 + \left(\frac{d\phi}{dt}\right)^2\right]cos\theta_{16}cos\phi + 2\frac{d\theta_6}{dt}\frac{d\phi}{dt}sin\theta_{16}sin\phi\right], \quad [B.87]$$

$$A_{Jz} = A_{Hz} + L_{HJ}\left[\frac{d^2\theta_6}{dt^2}cos\theta_{16} - \left(\frac{d\theta_6}{dt}\right)^2 sin\theta_{16}\right], \quad [B.88]$$

$$A_{Gx} = A_{Fx} - A_{Bucket}cos\theta_{11}sin\phi + 2V_{Bucket}\left[\frac{d\theta_{11}}{dt}sin\theta_{11}sin\phi - \frac{d\phi}{dt}cos\theta_{11}cos\phi\right] + L_{FG}\left[\frac{d^2\theta_{11}}{dt^2}sin\theta_{11}sin\phi - \frac{d^2\phi}{dt^2}cos\theta_{11}cos\phi + \left[\left(\frac{d\theta_{11}}{dt}\right)^2 + \left(\frac{d\phi}{dt}\right)^2\right]cos\theta_{11}sin\phi + 2\frac{d\theta_{11}}{dt}\frac{d\phi}{dt}sin\theta_{11}cos\phi\right], \quad [B.89]$$

$$A_{Gy} = A_{Fy} + A_{Bucket}cos\theta_{11}cos\phi + 2V_{Bucket}\left[-\frac{d\theta_{11}}{dt}sin\theta_{11}cos\phi - \frac{d\phi}{dt}cos\theta_{11}sin\phi\right] + L_{FG}\left[-\frac{d^2\theta_{11}}{dt^2}sin\theta_{11}cos\phi - \frac{d^2\phi}{dt^2}cos\theta_{11}sin\phi - \left[\left(\frac{d\theta_{11}}{dt}\right)^2 + \left(\frac{d\phi}{dt}\right)^2\right]cos\theta_{11}cos\phi + 2\frac{d\theta_{11}}{dt}\frac{d\phi}{dt}sin\theta_{11}sin\phi\right], \quad [B.90]$$

$$A_{Gz} =$$

$$A_{Fz} + A_{Bucket}sin\theta_{11} + 2V_{Bucket}\frac{d\theta_{11}}{dt}cos\theta_{11} + L_{FG}\frac{d^2\theta_{11}}{dt^2}cos\theta_{11} - L_{FG}\left(\frac{d\theta_{11}}{dt}\right)^2 sin\theta_{11}, \quad [B.91]$$

$$A_{Kx} =$$

$$A_{Gx} + L_{GK}\left[\frac{d^2\theta_{12}}{dt^2}sin\theta_{12}sin\phi - \frac{d^2\phi}{dt^2}cos\theta_{12}cos\phi + \left[\left(\frac{d\theta_{12}}{dt}\right)^2 + \left(\frac{d\phi}{dt}\right)^2\right]cos\theta_{12}sin\phi + 2\frac{d\theta_{12}}{dt}\frac{d\phi}{dt}sin\theta_{12}cos\phi\right], \quad [B.92]$$

$$A_{Ky} =$$

$$A_{Gy} + L_{GK}\left[-\frac{d^2\theta_{12}}{dt^2}sin\theta_{12}cos\phi - \frac{d^2\phi}{dt^2}cos\theta_{12}sin\phi - \left[\left(\frac{d\theta_{12}}{dt}\right)^2 + \left(\frac{d\phi}{dt}\right)^2\right]cos\theta_{12}cos\phi + 2\frac{d\theta_{12}}{dt}\frac{d\phi}{dt}sin\theta_{12}sin\phi\right], \quad [B.93]$$

$$A_{Kz} = A_{Gz} + L_{GK}\left[\frac{d^2\theta_{12}}{dt^2}cos\theta_{12} - \left(\frac{d\theta_{12}}{dt}\right)^2 sin\theta_{12}\right], \quad [B.94]$$

$$A_{Ix} =$$

$$A_{Kx} + L_{IK}\left[\frac{d^2\theta_{12}}{dt^2}sin\theta_{13}sin\phi - \frac{d^2\phi}{dt^2}cos\theta_{13}cos\phi + \left[\left(\frac{d\theta_{12}}{dt}\right)^2 + \left(\frac{d\phi}{dt}\right)^2\right]cos\theta_{13}sin\phi + 2\frac{d\theta_{12}}{dt}\frac{d\phi}{dt}sin\theta_{13}cos\phi\right], \quad [B.95]$$

$$A_{Iy} =$$

$$A_{Ky} + L_{IK}\left[-\frac{d^2\theta_{12}}{dt^2}sin\theta_{13}cos\phi - \frac{d^2\phi}{dt^2}cos\theta_{13}sin\phi - \left[\left(\frac{d\theta_{12}}{dt}\right)^2 + \left(\frac{d\phi}{dt}\right)^2\right]cos\theta_{13}cos\phi + 2\frac{d\theta_{12}}{dt}\frac{d\phi}{dt}sin\theta_{13}sin\phi\right], \quad [B.96]$$

$$A_{Iz} = A_{Kz} + L_{IK}\left[\frac{d^2\theta_{12}}{dt^2}cos\theta_{13} - \left(\frac{d\theta_{12}}{dt}\right)^2 sin\theta_{13}\right], \quad [B.97]$$

$$A_{Ix} =$$

$$A_{Hx} + L_{HI}\left[\frac{d^2\theta_{14}}{dt^2}sin\theta_{14}sin\phi - \frac{d^2\phi}{dt^2}cos\theta_{14}cos\phi + \left[\left(\frac{d\theta_{14}}{dt}\right)^2 + \left(\frac{d\phi}{dt}\right)^2\right]cos\theta_{14}sin\phi + 2\frac{d\theta_{14}}{dt}\frac{d\phi}{dt}sin\theta_{14}cos\phi\right], \quad [B.98]$$

$$A_{Iy} =$$

$$A_{Hy} + L_{HI}\left[-\frac{d^2\theta_{14}}{dt^2}sin\theta_{14}cos\phi - \frac{d^2\phi}{dt^2}cos\theta_{14}sin\phi - \left[\left(\frac{d\theta_{14}}{dt}\right)^2 + \left(\frac{d\phi}{dt}\right)^2\right]cos\theta_{14}cos\phi + 2\frac{d\theta_{14}}{dt}\frac{d\phi}{dt}sin\theta_{14}sin\phi\right], \quad [B.99]$$

$$A_{Iz} = A_{Hz} + L_{HI}\left[\frac{d^2\theta_{14}}{dt^2}cos\theta_{14} - \left(\frac{d\theta_{14}}{dt}\right)^2 sin\theta_{14}\right], \quad [B.100]$$

$$A_{Kx} =$$

$$A_{Jx} + L_{JK}\left[\frac{d^2\theta_{15}}{dt^2}sin\theta_{15}sin\phi - \frac{d^2\phi}{dt^2}cos\theta_{15}cos\phi + \left[\left(\frac{d\theta_{15}}{dt}\right)^2 + \left(\frac{d\phi}{dt}\right)^2\right]cos\theta_{15}sin\phi + 2\frac{d\theta_{15}}{dt}\frac{d\phi}{dt}sin\theta_{15}cos\phi\right], \quad [B.101]$$

$$A_{Ky} =$$

$$A_{Jy} + L_{JK}\left[-\frac{d^2\theta_{15}}{dt^2}sin\theta_{15}cos\phi - \frac{d^2\phi}{dt^2}cos\theta_{15}sin\phi - \left[\left(\frac{d\theta_{15}}{dt}\right)^2 + \left(\frac{d\phi}{dt}\right)^2\right]cos\theta_{15}cos\phi + 2\frac{d\theta_{15}}{dt}\frac{d\phi}{dt}sin\theta_{15}sin\phi\right], \quad [B.102]$$

$$A_{Kz} = A_{Jz} + L_{JK}\left[\frac{d^2\theta_{15}}{dt^2}cos\theta_{15} - \left(\frac{d\theta_{15}}{dt}\right)^2 sin\theta_{15}\right], \quad [B.103]$$

**[Equations B.99-B.103] are solved using matrix inversion for* $A_{Gx}, A_{Gy}, A_{Gz}, A_{Kx}, A_{Ky}, A_{Kz}, A_{Ix}, A_{Iy}, A_{Iz}, \frac{d^2\theta_{11}}{dt^2}, \frac{d^2\theta_{12}}{dt^2}, \frac{d^2\theta_{14}}{dt^2}, and\ \frac{d^2\theta_{15}}{dt^2}$.

Appendix C: Simulation Code for the Kinematic and Kinetic Modeling

This appendix presents the computer code used in the Embedded MATLAB Function within the Simulink modeling environment to model the kinematic and kinetic equations.

C.1 Kinematic Initialization Code

This program is used to initialize the angles needed for the kinematic simulations. Given initial guesses, exact solutions are produced. This program is run prior to the kinematic and kinetic code.

```
clear all
clc
Ts = 0.0005; %Set the time step
```

Initial angle guess:

```
theta1 = 121*pi/180;
theta2 = 108.93582595*pi/180;
theta3 = 104.81818929*pi/180;
theta5 = 53.94564121*pi/180;
theta6 = 86.04851575*pi/180;
theta11 = 289.87729812*pi/180;
theta13 = 16.50217558*pi/180;
theta14 = 308.86959258*pi/180;
theta15 = 239.79972844*pi/180;

thetai = zeros(16,1);
```

Fixed Lengths and angles (home position)

```
Lab = .473;
Lac = 1.836;
Lbc = 1.377; % Boom Cylinder
Lcd = 1.478;
Lce = 1.821; % Stick Cylinder
Lde = .42545;
Ldf = .409575;
Ldh = 1.832;
Lef = .62865;
Lfg  = 1.955; % Bucket Cylinder
Lfh = 1.634;
Lgi = .14581119045;
Lgk = .479;
Lhi = .480;
Lhj = .23601078943;
```

```
Lik = .380;
Ljk = .305;


alpha1 = 116.21026476*pi/180;
alpha2 = 42.12357315*pi/180;
alpha3 = 97.65790791*pi/180;
alpha4 = 55.31338777*pi/180;
alpha5 = 11.89449863*pi/180;
alpha6 = 14.41449652*pi/180;
alpha7 = 125.13794155*pi/180;
alpha8 = (180-179.41791570)*pi/180;
```

Solve the position loops to set the starting point

Triangle ABC

```
deltaXabc = [1;1];
Xabc = [theta2; theta3];

while max(abs(deltaXabc))>0.0001
Fabc = [Lab*cos(theta1)+Lbc*cos(Xabc(2))-Lac*cos(Xabc(1));
    Lab*sin(theta1)+Lbc*sin(Xabc(2))-Lac*sin(Xabc(1))];

Jabc = [Lac*sin(Xabc(1)) -Lbc*sin(Xabc(2));
       -Lac*cos(Xabc(1)) Lbc*cos(Xabc(2))];

deltaXabc = -Jabc\Fabc;

Xabc = Xabc+deltaXabc;
end
thetai(2) = Xabc(1);
thetai(3) = Xabc(2);
theta4 = ((theta2)+alpha1-pi);
```

Triangle CDE

```
deltaXcde = [1;1];
Xcde = [theta5; theta6];

while max(abs(deltaXcde))>0.0001
Fcde = [Lcd*cos(theta4)+Lde*cos(Xcde(2))-Lce*cos(Xcde(1));
        Lcd*sin(theta4)+Lde*sin(Xcde(2))-Lce*sin(Xcde(1))];

Jcde = [Lce*sin(Xcde(1)) -Lde*sin(Xcde(2));
       -Lce*cos(Xcde(1)) Lde*cos(Xcde(2))];

deltaXcde = -Jcde\Fcde;

Xcde = Xcde+deltaXcde;
end
```

```
thetai(5) = Xcde(1);
thetai(6) = Xcde(2);
theta7 = (2*pi-(alpha2+(alpha3-theta6)));
theta8 = (2*pi-(alpha3-theta6));
theta9 = (theta8-alpha4-alpha5);
theta10 = (theta8-alpha4);
theta16 = (theta10-alpha8);
```

Four-bar linkage with secondary loops (bucket mechanism)

```
deltaX4bar = [1;1;1;1];
X4bar = [theta11; theta13; theta14; theta15];
thetagi = pi-(alpha7-X4bar(2));

while max(abs(deltaX4bar))>0.0001
    f1 = Lhi*sin(X4bar(3))-Lik*sin(X4bar(2))-Ljk*sin(X4bar(4))-Lhj*sin(theta16);
    f2 = Lhi*cos(X4bar(3))-Lik*cos(X4bar(2))-Ljk*cos(X4bar(4))-Lhj*cos(theta16);
    f3 = Lfg*sin(X4bar(1))-Lgi*sin(thetagi)-Lhi*sin(X4bar(3))-Lfh*sin(theta9);
    f4 = Lfg*cos(X4bar(1))-Lgi*cos(thetagi)-Lhi*cos(X4bar(3))-Lfh*cos(theta9);
    F4bar = [f1;f2;f3;f4];

    J4bar = [0 -Lik*cos(X4bar(2)) Lhi*cos(X4bar(3)) -Ljk*cos(X4bar(4));
            0 Lik*sin(X4bar(2)) -Lhi*sin(X4bar(3)) Ljk*sin(X4bar(4));
            Lfg*cos(X4bar(1)) -Lgi*cos(thetagi) -Lhi*cos(X4bar(3)) 0;
            -Lfg*sin(X4bar(1)) Lgi*sin(thetagi) Lhi*sin(X4bar(3)) 0;];

    deltaX4bar = -J4bar\F4bar;

     X4bar = X4bar+deltaX4bar;
    thetagi = pi-(alpha7-X4bar(2));
end

thetai(11) = X4bar(1);
theta12 = (X4bar(2)+alpha6+pi);
thetai(13) = X4bar(2);
thetai(14)= X4bar(3);
thetai(15) = X4bar(4);
```

end

C.2 Kinematic and Kinetic Code

```
function [nexttheta, actuator, output, F_out, Fric_boom, Fric_stick, Fric_bucket] = Kinematics_netics(Aboom,Vboom,Lbc,Astick,Vstick,Lce,Abucket,Vbucket,Lfg,Dboom,Dstick,Dbucket,thet
a)
```

Initialize

```
%Fixed Lengths and angles(home position)
    Lab = 0.473;
    Lac = 1.836;
    Lcd = 1.478;
    Lde = 0.42545;
    Ldf = 0.409575;
    Ldh = 1.832;
    Lef = 0.62865;
    Lfh = 1.634;
    Lgi = 0.14581119045;
    Lgk = 0.479;
    Lhi = 0.480;
    Lhj = 0.23601078943;
    Lik = 0.380;
    Ljk = 0.305;

    alpha1 = 116.21026476*pi/180;
    alpha2 = 42.12357315*pi/180;
    alpha3 = 97.65790791*pi/180;
    alpha4 = 55.31338777*pi/180;
    alpha5 = 11.89449863*pi/180;
    alpha6 = 14.41449652*pi/180;
    alpha7 = 125.13794155*pi/180;
    alpha8 = (180-179.41791570)*pi/180;

    theta1 = 121*pi/180;

%Initialize non-imported variables
    nexttheta = zeros(16,1); %Angles to Pass

    dtheta2dt = 0; %Angles
    dtheta3dt = 0;
    dtheta5dt = 0;
    dtheta6dt = 0;
    dtheta11dt = 0;
    dtheta12dt = 0;
    dtheta14dt = 0;
    dtheta15dt = 0;

    d2theta2dt2 = 0; %Rotational Velocities
    d2theta3dt2 = 0;
    d2theta5dt2 = 0;
    d2theta6dt2 = 0;
```

```
    d2theta11dt2 = 0;
    d2theta12dt2 = 0;
    d2theta14dt2 = 0;
    d2theta15dt2 = 0;

    beta1 = 0; %Beta Angles
    beta2 = 0;
    beta3 = 0;
    beta4 = 0;
    beta5 = 0;
    beta6 = 0;
    beta7 = 0;
    beta8 = 0;
    beta9 = 0;
    beta10 = 0;
    beta11 = 0;
    beta12 = 0;

%Swing-related parameters (not used due to kinetics being 2D)
    Loa = 0;
    Lob = 0;
    phi = 0*pi/180; %Neglecting swing
    Ws = 0;
    As = 0;
```

Kinematic Analysis: Position

```
%Step 1:  Determine new angular orientation based on
%         the changed cylinder lengths.


%Loop A-B-C
    deltaXabc = [1;1]; %Run at least once
    Xabc = [theta(2); theta(3)]; %Intial guess

    while max(abs(deltaXabc)) > 0.0001 %Set tolerance
        Fabc = [Lab*cos(theta1)+Lbc*cos(Xabc(2))-Lac*cos(Xabc(1));
                Lab*sin(theta1)+Lbc*sin(Xabc(2))-Lac*sin(Xabc(1))];

        Jabc = [Lac*sin(Xabc(1)) -Lbc*sin(Xabc(2));
               -Lac*cos(Xabc(1)) Lbc*cos(Xabc(2))];

        deltaXabc = -Jabc\Fabc; %Adjustment variable
        Xabc = Xabc+deltaXabc; %Next guess
    end
%Assign new angles
        theta(2) = Xabc(1);
        theta(3) = Xabc(2);
        theta4 = theta(2)+alpha1-pi; %From loop ACD

%Loop C-D-E
    deltaXcde = [1;1]; %Run at least once
    Xcde = [theta(5); theta(6)]; %Intial guess
```

```
    while max(abs(deltaXcde)) > 0.0001 %Set tolerance
        Fcde = [Lcd*cos(theta4)+Lde*cos(Xcde(2))-Lce*cos(Xcde(1));
                Lcd*sin(theta4)+Lde*sin(Xcde(2))-Lce*sin(Xcde(1))];

        Jcde = [Lce*sin(Xcde(1)) -Lde*sin(Xcde(2));
               -Lce*cos(Xcde(1)) Lde*cos(Xcde(2))];

        deltaXcde = -Jcde\Fcde; %Adjustment variable
        Xcde = Xcde+deltaXcde; %Next guess
    end
%Assign new angles
        theta(5) = Xcde(1);
        theta(6) = Xcde(2);
        theta7 = 2*pi-(alpha2+(alpha3-theta(6))); %From loop D-E-F
        theta8 = 2*pi-(alpha3-theta(6)); %From loop D-E-F
        theta9 = theta8-alpha4-alpha5; %Froom loop D-F-H
        theta10 = theta8 - alpha4; %From loop D-F-H
        theta16 = theta10 - alpha8;

%Four-bar Linkage (Bucket Mechanism)

    deltaX4bar = [1;1;1;1]; %Run at least once
    X4bar = [theta(11); theta(13); theta(14); theta(15)]; %Initial guess
    thetagi = pi - (alpha7-theta(13)); %Intial guess

    while max(abs(deltaX4bar))>0.0001
        f1 = Lhi*sin(X4bar(3))-Lik*sin(X4bar(2))-Ljk*sin(X4bar(4))-Lhj*sin(theta16);
        f2 = Lhi*cos(X4bar(3))-Lik*cos(X4bar(2))-Ljk*cos(X4bar(4))-Lhj*cos(theta16);
        f3 = Lfg*sin(X4bar(1))-Lgi*sin(thetagi)-Lhi*sin(X4bar(3))-Lfh*sin(theta9);
        f4 = Lfg*cos(X4bar(1))-Lgi*cos(thetagi)-Lhi*cos(X4bar(3))-Lfh*cos(theta9);
        F4bar = [f1;f2;f3;f4];

        J4bar = [0 -Lik*cos(X4bar(2)) Lhi*cos(X4bar(3)) -Ljk*cos(X4bar(4));
                 0 Lik*sin(X4bar(2)) -Lhi*sin(X4bar(3)) Ljk*sin(X4bar(4));
                 Lfg*cos(X4bar(1)) -Lgi*cos(thetagi) -Lhi*cos(X4bar(3)) 0;
                 -Lfg*sin(X4bar(1)) Lgi*sin(thetagi) Lhi*sin(X4bar(3)) 0;];

        deltaX4bar = -J4bar\F4bar; %Adjustment varible
        X4bar = X4bar+deltaX4bar; %Next guess
        thetagi = pi-(alpha7-X4bar(2)); %Update this angle
    end

%Assign new angles
    theta(11) = X4bar(1);
    theta(13) = X4bar(2);
    theta12 = (theta(13)+alpha6+pi);
    theta(14) = X4bar(3);
    theta(15) = X4bar(4);


%Store thetas and positions
nexttheta = [theta1; theta(2); theta(3); theta4;
             theta(5); theta(6); theta7; theta8;
```

```
            theta9; theta10; theta(11); theta12;
            theta(13); theta(14); theta(15); theta16];
actuator = [Lbc;Lce;Lfg]; %To be passed out for storage
%END POSITION
```

Kinematic Analysis: Velocity

```
%Step 2: Find angular and linear velocities of all points and angles

%Loop A-B-C A1=[Vcx Vcy Vcz dtheta1dt dtheta2dt], B1=Knowns

    Vax = -Loa*Ws*cos(phi);
    Vay = -Loa*Ws*sin(phi);
    Vbx = -Lob*Ws*cos(phi);
    Vby = -Lob*Ws*sin(phi);

%Matrix inversion using relative velocity equations
    A1 = [1 0 0 -Lbc*sin(theta(3))*sin(phi) 0;
        0 1 0 Lbc*sin(theta(3))*cos(phi) 0;
        0 0 1 -Lbc*cos(theta(3)) 0;
        1 0 0 0 -Lac*sin(theta(2))*sin(phi);
        0 1 0 0 Lac*sin(theta(2))*cos(phi);
        0 0 1 0 -Lac*cos(theta(2))];

    B1 = [Vbx-Vboom*cos(theta(3))*sin(phi)-Lbc*Ws*cos(theta(3))*cos(phi);
        Vby+Vboom*cos(theta(3))*cos(phi)-Lbc*Ws*cos(theta(3))*sin(phi);
        Vboom*sin(theta(3));
        Vax-Lac*Ws*cos(theta(2))*cos(phi);
        Vay-Lac*Ws*cos(theta(2))*sin(phi);
        0];

    X1 = A1\B1; %where: x = [Vcx; Vcy; Vcz; dtheta1dt; dtheta2dt]

%Assign the variables
    Vcx = X1(1);
    Vcy = X1(2);
    Vcz = X1(3);
    dtheta3dt = X1(4);
    dtheta2dt = X1(5);

%Run equations for point D
    Vdx = Vcx + dtheta2dt*Lcd*sin(theta4)*sin(phi) - Ws*Lcd*cos(theta4)*cos(phi);
    Vdy = Vcy - dtheta2dt*Lcd*sin(theta4)*cos(phi) - Ws*Lcd*cos(theta4)*sin(phi);
    Vdz = Vcz + dtheta2dt*Lcd*cos(theta4);

%End Loop ABC

%Loop C-D-E
    A2 = [1 0 0 -Lce*sin(theta(5))*sin(phi) 0;
        0 1 0 Lce*sin(theta(5))*cos(phi) 0;
        0 0 1 -Lce*cos(theta(5)) 0;
        1 0 0 0 -Lde*sin(theta(6))*sin(phi);
        0 1 0 0 Lde*sin(theta(6))*cos(phi);
```

```
        0 0 1 0 -Lde*cos(theta(6))];

    B2 = [Vcx - Vstick*cos(theta(5))*sin(phi) - Ws*Lce*cos(theta(5))*cos(phi);
        Vcy + Vstick*cos(theta(5))*cos(phi) - Ws*Lce*cos(theta(5))*sin(phi);
        Vcz + Vstick*sin(theta(5));
        Vdx - Ws*Lde*cos(theta(6))*cos(phi);
        Vdy - Ws*Lde*cos(theta(6))*sin(phi);
        Vdz];

    X2 = A2\B2; %where: X = [Vex; Vey; Vez; dtheta2dt; dtheta6dt]

%Assign the variables
    Vex = X2(1);
    Vey = X2(2);
    Vez = X2(3);
    dtheta5dt = X2(4);
    dtheta6dt = X2(5);

%End Loop C-D-E

%Loop D-F-H
%Run equations for point F
    Vfx = Vdx + Ldf*(dtheta6dt*sin(theta8)*sin(phi)-Ws*cos(theta8)*cos(phi));
    Vfy = Vdy + Ldf*(-dtheta6dt*sin(theta8)*cos(phi)-Ws*cos(theta8)*sin(phi));
    Vfz = Vdz + Ldf*dtheta6dt*cos(theta8);

%Run equations for point H
    Vhx = Vdx + Ldh*(dtheta6dt*sin(theta10)*sin(phi)-Ws*cos(theta10)*cos(phi));
    Vhy = Vdy + Ldh*(-dtheta6dt*sin(theta10)*cos(phi)-Ws*cos(theta10)*sin(phi));
    Vhz = Vdz + Ldh*dtheta6dt*cos(theta10);

%Run equations for point J
    Vjx = Vhx + Lhj*(dtheta6dt*sin(theta16)*sin(phi)-Ws*cos(theta16)*cos(phi));
    Vjy = Vhy + Lhj*(-dtheta6dt*sin(theta16)*cos(phi)-Ws*cos(theta16)*sin(phi));
    Vjz = Vhz + Lhj*dtheta6dt*cos(theta16);

%End loop D-F-H

%Four-bar Linkage

    A3 = [1 0 0 0 0 0 0 0 0 -Lfg*sin(theta(11))*sin(phi) 0 0 0;
        0 1 0 0 0 0 0 0 0 Lfg*sin(theta(11))*cos(phi) 0 0 0;
        0 0 1 0 0 0 0 0 0 -Lfg*cos(theta(11)) 0 0 0;
        -1 0 0 1 0 0 0 0 0 0 -Lgk*sin(theta12)*sin(phi) 0 0;
        0 -1 0 0 1 0 0 0 0 0 Lgk*sin(theta12)*cos(phi) 0 0;
        0 0 -1 0 0 1 0 0 0 0 -Lgk*cos(theta12) 0 0;
        0 0 0 -1 0 0 1 0 0 0 -Lik*sin(theta(13))*sin(phi) 0 0;
        0 0 0 0 -1 0 0 1 0 0 Lik*sin(theta(13))*cos(phi) 0 0;
        0 0 0 0 0 -1 0 0 1 0 -Lik*cos(theta(13)) 0 0;
        0 0 0 0 0 0 1 0 0 0 0 -Lhi*sin(theta(14))*sin(phi) 0;
        0 0 0 0 0 0 0 1 0 0 0 Lhi*sin(theta(14))*cos(phi) 0;
        0 0 0 0 0 0 0 0 1 0 0 -Lhi*cos(theta(14)) 0;
        0 0 0 1 0 0 0 0 0 0 0 0 -Ljk*sin(theta(15))*sin(phi);
        0 0 0 0 1 0 0 0 0 0 0 0 Ljk*sin(theta(15))*cos(phi);
```

```
        0 0 0 0 0 1 0 0 0 0 0 0 -Ljk*cos(theta(15))];

    B3 = [Vfx - Vbucket*cos(theta(11))*sin(phi) - Ws*Lfg*cos(theta(11))*cos(phi);
        Vfy + Vbucket*cos(theta(11))*cos(phi) + Ws*Lfg*cos(theta(11))*sin(phi);
        Vfz + Vbucket*sin(theta(11));
        -Ws*Lgk*cos(theta12)*cos(phi);
        -Ws*Lgk*cos(theta12)*sin(phi);
        0;
        -Ws*Lik*cos(theta(13))*cos(phi);
        -Ws*Lik*cos(theta(13))*sin(phi);
        0;
        Vhx - Ws*Lhi*cos(theta(14))*cos(phi);
        Vhy - Ws*Lhi*cos(theta(14))*sin(phi);
        Vhz;
        Vjx - Ws*Ljk*cos(theta(15))*cos(phi);
        Vjy - Ws*Ljk*cos(theta(15))*sin(phi);
        Vjz];

    X3 = A3\B3;

%Assign variables
    Vgx = X3(1);
    Vgy = X3(2);
    Vgz = X3(3);
    Vkx = X3(4);
    Vky = X3(5);
    Vkz = X3(6);
    Vix = X3(7);
    Viy = X3(8);
    Viz = X3(9);
    dtheta11dt = X3(10);
    dtheta12dt = X3(11);
    dtheta14dt = X3(12);
    dtheta15dt = X3(13);

%End Four-bar Linkage
```

Kinematic Analysis: Acceleration

```
%Step 3: Get accelerations of all points and angles

%%Boom
    Aax = -Loa*(As*cos(phi)+(Ws^2)*sin(phi));
    Aay = Loa*(-As*sin(phi)+(Ws^2)*cos(phi));
    Abx = -Lob*(As*cos(phi)+(Ws^2)*sin(phi));
    Aby = Lob*(-As*sin(phi)+(Ws^2)*cos(phi));

    A4 = [1 0 0 -Lbc*sin(theta(3))*sin(phi) 0;
        0 1 0 Lbc*sin(theta(3))*cos(phi) 0;
        0 0 1 -Lbc*cos(theta(3)) 0;
        1 0 0 0 -Lac*sin(theta(2))*sin(phi);
        0 1 0 0 Lac*sin(theta(2))*cos(phi);
        0 0 1 0 -Lac*cos(theta(2))];
```

```
    B4   =   [Abx-Aboom*(cos(theta(3))*sin(phi))+2*Vboom*(dtheta3dt*sin(theta(3))*sin(phi)-
Ws*cos(theta(3))*cos(phi))+Lbc*(-
As*cos(theta(3))*cos(phi)+((dtheta3dt^2)+(Ws^2))*cos(theta(3))*sin(phi)+2*dtheta3dt*Ws*sin
(theta(3))*cos(phi));
        Aby+Aboom*(cos(theta(3))*cos(phi))+2*Vboom*(-dtheta3dt*sin(theta(3))*cos(phi)-
Ws*cos(theta(3))*sin(phi))+Lbc*(-As*cos(theta(3))*sin(phi)-
((dtheta3dt^2)+(Ws^2))*cos(theta(3))*cos(phi)+2*dtheta3dt*Ws*sin(theta(3))*sin(phi));
        Aboom*sin(theta(3))+2*Vboom*dtheta3dt*cos(theta(3))-
Lbc*sin(theta(3))*(dtheta3dt^2);
        Aax+Lac*(-
As*cos(theta(2))*cos(phi)+((dtheta2dt^2)+(Ws^2))*cos(theta(2))*sin(phi)+2*dtheta2dt*Ws*sin
(theta(2))*cos(phi));
        Aay+Lac*(-As*cos(theta(2))*sin(phi)-
((dtheta2dt^2)+(Ws^2))*cos(theta(2))*cos(phi)+2*dtheta2dt*Ws*sin(theta(2))*sin(phi));
        -Lac*(dtheta2dt^2)*sin(theta(2))];

    X4 = A4\B4;

%Assign Variables
    Acx = X4(1);
    Acy = X4(2);
    Acz = X4(3);
    d2theta3dt2 = X4(4);
    d2theta2dt2 = X4(5);

%Relationships for point D (only using 2D to speed up)
%                        Adx     =     Acx     +     Lcd*(d2theta2dt2*sin(theta4)*sin(phi)-
As*cos(theta4)*cos(phi)+((Ws^2)+(dtheta2dt^2))*cos(theta4)*sin(phi)+2*Ws*dtheta2dt*sin(the
ta4)*cos(phi));
%          Ady  =  Acy  +  Lcd*(-d2theta2dt2*sin(theta4)*cos(phi)-As*cos(theta4)*sin(phi)-
((Ws^2)+(dtheta2dt^2))*cos(theta4)*cos(phi)+2*Ws*dtheta2dt*sin(theta4)*sin(phi));
%     Adz = Acz + Lcd*(d2theta2dt2*cos(theta4)-(dtheta2dt^2)*sin(theta4));
    Adx = 0;
    Ady = Acy-d2theta2dt2*Lcd*sin(theta4)-Lcd*(dtheta2dt^2)*cos(theta4);
    Adz = Acz+d2theta2dt2*Lcd*cos(theta4)-Lcd*(dtheta2dt^2)*sin(theta4);

%End Boom

%%Stick
    A5 = [1 0 0 -Lce*sin(theta(5))*sin(phi) 0;
        0 1 0 Lce*sin(theta(5))*cos(phi) 0;
        0 0 1 -Lce*cos(theta(5)) 0;
        1 0 0 0 -Lde*sin(theta(6))*sin(phi);
        0 1 0 0 Lde*sin(theta(6))*cos(phi);
        0 0 1 0 -Lde*cos(theta(6))];

    B5   =   [Acx-Astick*cos(theta(5))*sin(phi)+2*Vstick*(dtheta5dt*sin(theta(5))*sin(phi)-
Ws*cos(theta(5))*cos(phi))+Lce*(-
As*cos(theta(5))*cos(phi)+((dtheta5dt^2)+(Ws^2))*cos(theta(5))*sin(phi)+2*dtheta5dt*Ws*sin
(theta(5))*cos(phi));
        Acy+Astick*cos(theta(5))*cos(phi)+2*Vstick*(-dtheta5dt*sin(theta(5))*cos(phi)-
Ws*cos(theta(5))*sin(phi))+Lce*(-As*cos(theta(5))*sin(phi)-
((dtheta5dt^2)+(Ws^2))*cos(theta(5))*cos(phi)+2*dtheta5dt*Ws*sin(theta(5))*sin(phi));
```

```
        Acz+Astick*sin(theta(5))+2*Vstick*dtheta5dt*cos(theta(5))-
Lce*(dtheta5dt^2)*sin(theta(5));
        Adx+Lde*(-
As*cos(theta(6))*cos(phi)+((dtheta6dt^2)+(Ws^2))*cos(theta(6))*sin(phi)+2*dtheta6dt*Ws*sin
(theta(6))*cos(phi));
        Ady+Lde*(-As*cos(theta(6))*sin(phi)-
((dtheta6dt^2)+(Ws^2))*cos(theta(6))*cos(phi)+2*dtheta6dt*Ws*sin(theta(6))*sin(phi));
        Adz+Lde*(-(dtheta6dt^2)*sin(theta(6)))];

    X5 = A5\B5;
        Aex = X5(1);
        Aey = X5(2);
        Aez = X5(3);
        d2theta5dt2 = X5(4);
        d2theta6dt2 = X5(5);

%Relationships for point F (only using 2D to speed up)
%                                Afx      =      Adx+Ldf*(d2theta6dt2*sin(theta8)*sin(phi)-
As*cos(theta8)*cos(phi)+((dtheta6dt^2)+(Ws^2))*cos(theta8)*sin(phi)+2*dtheta6dt*Ws*sin(the
ta8)*cos(phi));
%             Afy   =   Ady+Ldf*(-d2theta6dt2*sin(theta8)*cos(phi)-As*cos(theta8)*sin(phi)-
((dtheta6dt^2)+(Ws^2))*cos(theta8)*cos(phi)+2*dtheta6dt*Ws*sin(theta8)*sin(phi));
%     Afz = Adz+Ldf*(d2theta6dt2*cos(theta8)-(dtheta6dt^2)*sin(theta8));
    Afy = Ady-d2theta6dt2*Ldf*sin(theta8)-Ldf*(dtheta6dt^2)*cos(theta8);
    Afz = Adz+d2theta6dt2*Ldf*cos(theta8)-Ldf*(dtheta6dt^2)*sin(theta8);

%Relationships for point H (only using 2D to speed up)
%                                Ahx      =      Adx+Ldh*(d2theta6dt2*sin(theta10)*sin(phi)-
As*cos(theta10)*cos(phi)+((dtheta6dt^2)+(Ws^2))*cos(theta10)*sin(phi)+2*dtheta6dt*Ws*sin(t
heta10)*cos(phi));
%            Ahy   =   Ady+Ldh*(-d2theta6dt2*sin(theta10)*cos(phi)-As*cos(theta10)*sin(phi)-
((dtheta6dt^2)+(Ws^2))*cos(theta10)*cos(phi)+2*dtheta6dt*Ws*sin(theta10)*sin(phi));
%     Ahz = Adz+Ldh*(d2theta6dt2*cos(theta10)-(dtheta6dt^2)*sin(theta10));
    Ahy = Ady-d2theta6dt2*Ldh*sin(theta10)-Ldh*(dtheta6dt^2)*cos(theta10);
    Ahz = Adz+d2theta6dt2*Ldh*cos(theta10)-Ldh*(dtheta6dt^2)*sin(theta10);

%Relationships for point J (only using 2D to speed up)
%                              Ajx      =      Ahx+Lhj*(d2theta6dt2*sin(theta(16))*sin(phi)-
As*cos(theta(16))*cos(phi)+((dtheta6dt^2)+(Ws^2))*cos(theta(16))*sin(phi)+2*dtheta6dt*Ws*s
in(theta(16))*cos(phi));
%         Ajy  =  Ahy+Lhj*(-d2theta6dt2*sin(theta(16))*cos(phi)-As*cos(theta(16))*sin(phi)-
((dtheta6dt^2)+(Ws^2))*cos(theta(16))*cos(phi)+2*dtheta6dt*Ws*sin(theta(16))*sin(phi));
%     Ajz = Ahz+Lhj*(d2theta6dt2*cos(theta(16))-(dtheta6dt^2)*sin(theta(16)));
    Ajy = Ahy-d2theta6dt2*Lhj*sin(theta16)-Lhj*(dtheta6dt^2)*cos(theta16);
    Ajz = Ahz+d2theta6dt2*Lhj*cos(theta16)-Lhj*(dtheta6dt^2)*sin(theta16);

%End Stick

%Bucket - four bar linkage equations in 3D - Not used
% A6 = [1 0 0 0 0 0 0 0 0 -Lfg*sin(theta(11))*sin(phi) 0 0 0;
%      0 1 0 0 0 0 0 0 0  Lfg*sin(theta(11))*cos(phi) 0 0 0;
%      0 0 1 0 0 0 0 0 0 -Lfg*cos(theta(11)) 0 0 0;
%      -1 0 0 1 0 0 0 0 0 -Lgk*sin(theta12)*sin(phi) 0 0;
%      0 -1 0 0 1 0 0 0 0  Lgk*sin(theta12)*cos(phi) 0 0;
```

```
%      0 0 -1 0 0 1 0 0 0 0 -Lgk*cos(theta12) 0 0;
%      0 0 0 -1 0 0 1 0 0 0 -Lik*sin(theta(13))*sin(phi) 0 0;
%      0 0 0 0 -1 0 0 1 0 0  Lik*sin(theta(13))*cos(phi) 0 0;
%      0 0 0 0 0 -1 0 0 1 0 -Lik*cos(theta(13)) 0 0;
%      0 0 0 0 0 0 1 0 0 0 0 -Lhi*sin(theta(14))*sin(phi) 0;
%      0 0 0 0 0 0 0 1 0 0 0  Lhi*sin(theta(14))*cos(phi) 0;
%      0 0 0 0 0 0 0 0 1 0 0 -Lhi*cos(theta(14)) 0;
%      0 0 0 1 0 0 0 0 0 0 0 0 -Ljk*sin(theta(15))*sin(phi);
%      0 0 0 0 1 0 0 0 0 0 0 0  Ljk*sin(theta(15))*cos(phi);
%      0 0 0 0 0 1 0 0 0 0 0 0 -Ljk*cos(theta(15))];
%
% B6 = [Afx-Abucket*cos(theta(11))*sin(phi)+2*Vbucket*(dtheta11dt*sin(theta(11))*sin(phi)-
Ws*cos(theta(11))*cos(phi))+Lfg*(-
As*cos(theta(11))*cos(phi)+((dtheta11dt^2)+(Ws^2))*cos(theta(11))*sin(phi)+2*dtheta11dt*Ws
*sin(theta(11))*cos(phi));
%       Afy+Abucket*cos(theta(11))*cos(phi)+2*Vbucket*(-dtheta11dt*sin(theta(11))*cos(phi)-
Ws*cos(theta(11))*sin(phi))+Lfg*(-As*cos(theta(11))*sin(phi)-
((dtheta11dt^2)+(Ws^2))*cos(theta(11))*sin(phi)+2*dtheta11dt*Ws*sin(theta(11))*sin(phi));
%                            Afz+Abucket*sin(theta(11))+2*Vbucket*dtheta11dt*cos(theta(11))-
Lfg*(dtheta11dt^2)*sin(theta(11));
%                                                                                    Lgk*(-
As*cos(theta12)*cos(phi)+((dtheta12dt^2)+(Ws^2))*cos(theta12)*sin(phi)+2*dtheta12dt*Ws*sin
(theta12)*cos(phi));
%                                                          Lgk*(-As*cos(theta12)*sin(phi)-
((dtheta12dt^2)+(Ws^2))*cos(theta12)*cos(phi)+2*dtheta12dt*Ws*sin(theta12)*sin(phi));
%      Lgk*(-(dtheta12dt^2)*sin(theta12));
%                                                                                    Lik*(-
As*cos(theta(13))*cos(phi)+((dtheta12dt^2)+(Ws^2))*cos(theta(13))*sin(phi)+2*dtheta12dt*Ws
*sin(theta(13))*cos(phi));
%                                                        Lik*(-As*cos(theta(13))*sin(phi)-
((dtheta12dt^2)+(Ws^2))*cos(theta(13))*cos(phi)+2*dtheta12dt*Ws*sin(theta(13))*sin(phi));
%      Lik*(-(dtheta12dt^2)*sin(theta(13)));
%                                                                                  Ahx+Lhi*(-
As*cos(theta(14))*cos(phi)+((dtheta14dt^2)+(Ws^2))*cos(theta(14))*sin(phi)+2*dtheta14dt*Ws
*sin(theta(14))*cos(phi));
%                                                       Ahy+Lhi*(-As*cos(theta(14))*sin(phi)-
((dtheta14dt^2)+(Ws^2))*cos(theta(14))*cos(phi)+2*dtheta14dt*Ws*sin(theta(14))*sin(phi));
%      Ahz+Lhi*(-(dtheta14dt^2)*sin(theta(14)));
%                                                                                  Ajx+Ljk*(-
As*cos(theta(15))*cos(phi)+((dtheta15dt^2)+(Ws^2))*cos(theta(15))*sin(phi)+2*dtheta15dt*Ws
*sin(theta(15))*cos(phi));
%                                                       Ajy+Ljk*(-As*cos(theta(15))*sin(phi)-
((dtheta15dt^2)+(Ws^2))*cos(theta(15))*cos(phi)+2*dtheta15dt*Ws*sin(theta(15))*sin(phi));
%      Ajz+Ljk*(-(dtheta15dt^2)*sin(theta(15)))];
%
% X6 = A6\B6;
%Assign Variables
%     Agx = X6(1);
%     Agy = X6(2);
%     Agz = X6(3);
%     Akx = X6(4);
%     Aky = X6(5);
%     Akz = X6(6);
%     Aix = X6(7);
```

```
%     Aiy = X6(8);
%     Aiz = X6(9);
%     d2theta11dt2 = X6(10);
%     d2theta13dt2 = X6(11);
%     d2theta14dt2 = X6(12);
%     d2theta15dt2 = X6(13);

% 2D Equations for four-bar linkage
    A7 = [1 0 0 0 0 0 Lfg*sin(theta(11)) 0 0 0;
          0 1 0 0 0 0 -Lfg*cos(theta(11)) 0 0 0;
          -1 0 1 0 0 0 0 Lgk*sin(theta12) 0 0;
          0 -1 0 1 0 0 0 -Lgk*cos(theta12) 0 0;
          0 0 -1 0 1 0 0 Lik*sin(theta(13)) 0 0;
          0 0 0 -1 0 1 0 -Lik*cos(theta(13)) 0 0;
          0 0 0 0 1 0 0 0 Lhi*sin(theta(14)) 0;
          0 0 0 0 0 1 0 0 -Lhi*cos(theta(14)) 0;
          0 0 1 0 0 0 0 0 0 Ljk*sin(theta(15));
          0 0 0 1 0 0 0 0 0 -Ljk*cos(theta(15))];

    B7          =          [Afy+Abucket*cos(theta(11))-2*dtheta11dt*Vbucket*sin(theta(11))-
(dtheta11dt^2)*Lfg*cos(theta(11));
          Afz+Abucket*sin(theta(11))+2*dtheta11dt*Vbucket*cos(theta(11))-
(dtheta11dt^2)*Lfg*sin(theta(11));
          -(dtheta12dt^2)*Lgk*cos(theta12);
          -(dtheta12dt^2)*Lgk*sin(theta12);
          -(dtheta12dt^2)*Lik*cos(theta(13));
          -(dtheta12dt^2)*Lik*sin(theta(13));
          Ahy-(dtheta14dt^2)*Lhi*cos(theta(14));
          Ahz-(dtheta14dt^2)*Lhi*sin(theta(14));
          Ajy-(dtheta15dt^2)*Ljk*cos(theta(15));
          Ajz-(dtheta15dt^2)*Ljk*sin(theta(15))];

    X7 = A7\B7;

%Assign Variables
    Agy = X7(1);
    Agz = X7(2);
    Aky = X7(3);
    Akz = X7(4);
    Aiy = X7(5);
    Aiz = X7(6);
    d2theta11dt2 = X7(7);
    d2theta12dt2 = X7(8);
    d2theta14dt2 = X7(9);
    d2theta15dt2 = X7(10);

% acceleration = [Acy; Acz;
%                 Ady; Adz;
%                 Aey; Aez;
%                 Afy; Afz;
%                 Agy; Agz;
%                 Ahy; Ahz;
%                 Aiy; Aiz;
%                 Ajy; Ajz;
```

```
%                 Aky; Akz];

%End Acceleration
```

Kinetic Analysis: COG Kinematics

```
%Step 4: Get velocity and acceleration of cg points for boom,
%           stick and bucket linkages


%Center of Gravity Calculations
%Parameters
%Estimated using AutoCAD massprop command

    Lar = 1.465;
    Lcr = .622;
    Ldr = 1.416;

    Lds = .822;
    Les = 1.176;
    Lfs = .620;
    Lhs = 1.049;
    Ljs = 1.285;

    Ljt1 = .539;
    Lkt1 = .465;
    Ljt2 = .662;
    Lkt2 = .597;
    Lt1t2 = 0; %distance between bucket cg and load cg

%Beta Angles based on existing angles and above lengths
    beta1 = theta(2)-acos(((Lac^2)+(Lar^2)-(Lcr^2))/(2*Lac*Lar));
    beta2 = 2*pi+(theta4-acos(((Lcd^2)+(Lcr^2)-(Ldr^2))/(2*Lcd*Lcr)));
    beta3 = pi+theta4+acos(((Lcd^2)+(Ldr^2)-(Lcr^2))/(2*Lcd*Ldr));
    beta4 = theta8-acos(((Lds^2)+(Ldf^2)-(Lfs^2))/(2*Lds*Ldf));
    beta5 = theta7-acos(((Les^2)+(Lef^2)-(Lfs^2))/(2*Les*Lef));
    beta6 = theta9-acos(((Lfs^2)+(Lfh^2)-(Lhs^2))/(2*Lfs*Lfh));
    beta7 = theta10-pi-acos(((Ldh^2)+(Lhs^2)-(Lds^2))/(2*Ldh*Lhs));
    beta8 = (theta16)-pi-acos(((Lhj^2)+(Ljs^2)-(Lhs^2))/(2*Lhj*Ljs));
    beta9 = theta(15)-acos(((Ljt1^2)+(Ljk^2)-(Lkt1^2))/(2*Ljt1*Ljk));
    beta10 = (theta(15)-pi)+acos(((Lkt1^2)+(Ljk^2)-(Ljt1^2))/(2*Lkt1*Ljk));
    beta11 = theta(15)-acos(((Ljt2^2)+(Ljk^2)-(Lkt2^2))/(2*Ljt2*Ljk));
    beta12 = (theta(15)-pi)+acos(((Lkt2^2)+(Ljk^2)-(Ljt2^2))/(2*Lkt2*Ljk));

%Velocities/Accelerations at CG points (in 2D, 3D not shown)
%Boom
    Vry = Lar*(-dtheta2dt)*sin(beta1);
    Vrz = Lar*dtheta2dt*cos(beta1);

    Ary = -Lar*d2theta2dt2*sin(beta1)-Lar*(dtheta2dt^2)*cos(beta1);
    Arz = Lar*d2theta2dt2*cos(beta1)-Lar*(dtheta2dt^2)*sin(beta1);

%Stick
```

```
    Vsy = Vdy+Lds*(-dtheta6dt*sin(beta4));
    Vsz = Vdz+Lds*dtheta6dt*cos(beta4);

    Asy = Ady+Lds*(-d2theta6dt2*sin(beta4)-((dtheta6dt^2))*cos(beta4));
    Asz = Adz+Lds*(d2theta6dt2*cos(beta4)-(dtheta6dt^2)*sin(beta4));

%Bucket
    Vty = Vjy+Ljt1*(-dtheta15dt*sin(beta9));
    Vtz = Vjz+Ljt1*dtheta15dt*cos(beta9);

    Aty = Ajy+Ljt1*(-d2theta15dt2*sin(beta9)-(dtheta15dt^2)*cos(beta9));
    Atz = Ajz+Ljt1*(d2theta15dt2*cos(beta9)-(dtheta15dt^2)*sin(beta9));

%End CG Kinematics
```

Kinetic Analysis

```
%Step 5: One Matrix. 26 Equations. 26 Unknowns.

%Masses used are from JD parts shipping info (kg)
    Mboom = 340.19;
    Mstick = 239.04+187.79;
    Mbucket = 205.02;

    Mload = 0; %Dynamic input in reality, just a place holder here

%Properties of steel
    steeldensity = 7800; %kg/m3
    steelthickness = 0.02; %m

%Calculate the mass MOI using Iarea from AutoCAD
    Ir = (.60739+.0576155)*(steeldensity*steelthickness);%boom
    Is = (.39056+.0474817)*(steeldensity*steelthickness);%stick
    It1 = (.02638104+.0304614)*(steeldensity*steelthickness); %bucket only
    %It2 = 0*(.0189375+.00819411)*(steeldensity*steelthickness); %load only

    Kinetics_A = [1 0 0 0 0 0 1 0 0 0 1 0 0 0 0 0 0 0 0 0 0 0 0 0 0;
                  0 1 0 0 0 0 0 1 0 0 0 1 0 0 0 0 0 0 0 0 0 0 0 0 0;
                  -Lar*sin(beta1) Lar*cos(beta1) 0 0 0 0 -Lcr*sin(beta2) Lcr*cos(beta2) 0
0 -Ldr*sin(beta3) Ldr*cos(beta3) 0 0 0 0 0 0 0 0 0 0 0 0 0;
                  0 0 1 0 1 0 0 0 0 0 0 0 0 0 0 0 0 0 0 0 0 0 0 0 0;
                  0 0 0 1 0 1 0 0 0 0 0 0 0 0 0 0 0 0 0 0 0 0 0 0 0;
                  0 0 sin(theta(3)) -cos(theta(3)) -sin(theta(3)) cos(theta(3)) 0 0 0 0 0
0 0 0 0 0 0 0 0 0 0 0 0 0 0 0;
                  0 0 0 0 0 0 0 0 0 0 -1 0 -1 0 -1 0 0 0 1 0 0 0 -1 0 0 0;
                  0 0 0 0 0 0 0 0 0 0 0 -1 0 -1 0 -1 0 0 0 1 0 0 0 -1 0 0;
                  0 0 0 0 0 0 0 0 0 0 Lds*sin(beta4) -Lds*cos(beta4) Les*sin(beta5) -
Les*cos(beta5) Lfs*sin(beta6) -Lfs*cos(beta6) 0 0 -Lhs*sin(beta7) Lhs*cos(beta7) 0 0
Ljs*sin(beta8) -Ljs*cos(beta8) 0 0;
                  0 0 0 0 0 0 0 0 1 0 0 0 1 0 0 0 0 0 0 0 0 0 0 0 0;
                  0 0 0 0 0 0 0 0 0 1 0 0 0 1 0 0 0 0 0 0 0 0 0 0 0;
                  0 0 0 0 0 0 0 0 sin(theta(5)) -cos(theta(5)) 0 0 -sin(theta(5))
cos(theta(5)) 0 0 0 0 0 0 0 0 0 0 0 0;
```

```
                0 0 0 0 0 0 0 0 0 0 0 0 0 0 0 0 0 0 0 0 0 0 1 0 1 0;
                0 0 0 0 0 0 0 0 0 0 0 0 0 0 0 0 0 0 0 0 0 0 0 1 0 1;
                0 0 0 0 0 0 0 0 0 0 0 0 0 0 0 0 0 0 0 0 0 0 0 0 Ljt1*sin(beta9) -
Ljt1*cos(beta9) Lkt1*sin(beta10) -Lkt1*cos(beta10);
                0 0 0 0 0 0 0 0 0 0 0 0 0 0 -1 0 0 0 -1 0 0 0 -1 0;
                0 0 0 0 0 0 0 0 0 0 0 0 0 0 0 -1 0 0 0 -1 0 0 0 -1;
                0 0 0 0 0 0 0 0 0 0 0 0 0 0 0 0 0 0 0 Lgk*sin(theta(13)+alpha6) -
Lgk*cos(theta(13)+alpha6) 0 0 Lik*sin(theta(13)) -Lik*cos(theta(13)) 0 0 0 0;
                0 0 0 0 0 0 0 0 0 0 0 0 0 0 0 0 0 0 -1 0 1 0 0 0 0 0;
                0 0 0 0 0 0 0 0 0 0 0 0 0 0 0 0 0 0 0 -1 0 1 0 0 0 0;
                0 0 0 0 0 0 0 0 0 0 0 0 0 0 0 0 0 0 0 -sin(theta(14)) cos(theta(14)) -
sin(theta(14)) cos(theta(14)) 0 0 0 0;
                0 0 0 0 0 0 0 0 0 0 0 0 0 0 1 0 1 0 0 0 0 0 0 0 0 0;
                0 0 0 0 0 0 0 0 0 0 0 0 0 0 0 1 0 1 0 0 0 0 0 0 0 0;
                0 0 0 0 0 0 0 0 0 0 0 0 0 0 -cos(1.5*pi-theta(11)) sin(1.5*pi-theta(11))
cos(1.5*pi-theta(11)) -sin(1.5*pi-theta(11)) 0 0 0 0 0 0 0 0;
                0 0 0 0 1 0 1 0 1 0 0 0 0 0 0 0 0 0 0 0 0 0 0 0 0 0;
                0 0 0 0 0 1 0 1 0 1 0 0 0 0 0 0 0 0 0 0 0 0 0 0 0 0];

    Kinetics_B = [Ary*Mboom;
                Arz*Mboom+Mboom*9.81;
                Ir*d2theta2dt2;
                0;
                0;
                0;
                Asy*Mstick;
                Asz*Mstick+Mstick*9.81;
                Is*d2theta6dt2;
                0;
                0;
                0;
                Aty*Mbucket;
                Atz*Mbucket+(Mbucket+Mload)*9.81;
                It1*d2theta15dt2;
                0;
                0;
                0;
                0;
                0;
                0;
                0;
                0;
                0;
                0;
                0];
    Kinetics_X = Kinetics_A\Kinetics_B;

%Logic to find forces along actuators avoiding division by zero
    if (0.25*pi<theta(3)<0.75*pi)||(1.25*pi<theta(3)<1.75*pi)
        Fboom = [Kinetics_X(5)/cos(theta(3))];
    else
        Fboom = [Kinetics_X(6)/sin(theta(3))];
    end
```

```
    if (0.25*pi<theta(5)<0.75*pi)||(1.25*pi<theta(5)<1.75*pi)
        Fstick = [Kinetics_X(13)/cos(theta(5))];
    else
        Fstick = [Kinetics_X(14)/sin(theta(5))];
    end

    if (0.25*pi<theta(11)<0.75*pi)||(1.25*pi<theta(11)<1.75*pi)
        Fbucket = [-Kinetics_X(15)/cos(theta(11))];
    else
        Fbucket = [-Kinetics_X(16)/sin(theta(11))];
    end

%Viscous Approximation at Static Friction Force
    Ffric_boom = Vboom*Dboom;
    Ffric_stick = Vstick*Dstick;
    Ffric_bucket = Vbucket*Dbucket;

%Bound the friction to get a rough stiction
    if (Ffric_boom > 450)
        Ffric_boom = 450;
    elseif (Ffric_boom < -450);
        Ffric_boom = -450;
    end

    if (Ffric_stick > 450)
        Ffric_stick = 450;
    elseif (Ffric_stick < -450);
        Ffric_stick = -450;
    end

    if (Ffric_bucket > 450)
        Ffric_bucket = 450;
    elseif (Ffric_bucket < -450);
        Ffric_bucket = -450;
    end

%Viscous Friction Approximation
    F2 = 250*Vboom;
    F3 = 250*Vstick;
    F4 = 250*Vbucket;

%Combine the Friction
    Fric_boom = -(Ffric_boom+F2);
    Fric_stick = -(Ffric_stick+F3);
    Fric_bucket = -(Ffric_bucket+F4);

%All Variables out to be used in viewer
    output = [Aboom; Vboom; Lbc; Astick; Vstick; Lce; Abucket; Vbucket; Lfg; theta(2);
dtheta2dt;  d2theta2dt2;  theta(6);  dtheta6dt;  d2theta6dt2;  theta(15);  dtheta15dt;
d2theta15dt2; Fboom; Fstick; Fbucket];

%Send out the forces
    F_out = [Fboom-Ffric_boom-F2; Fstick-Ffric_stick-F3; Fbucket-Ffric_bucket-F4];
end %End Box
```

Appendix D: Detailed Kinetic Equations

The purpose of this appendix is to present the complete set of equations developed for the kinetic model of the John Deere (JD) 410G backhoe workgroup.

D.1 System Description

The JD 410G backhoe is made up of eight bodies to be modeled, shown in Figure D.1. There are the three hydraulic cylinders, the boom, stick, and bucket bodies, as well as the two bucket guide pieces.

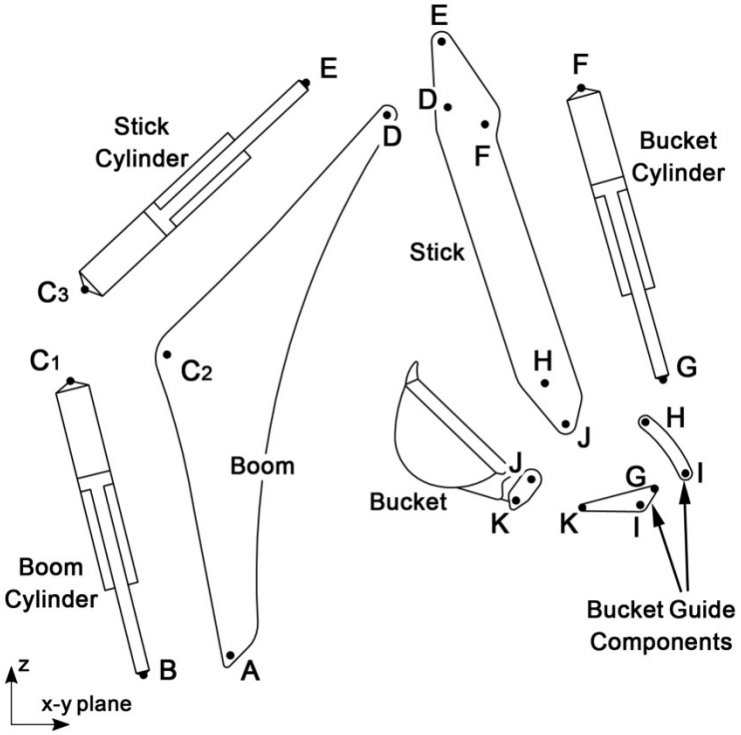

Figure D.1 Kinetic Modeling Components of the JD 410G Backhoe

The objective of the kinetic equations is to determine the forces acting at each of the modeling points in Figure D.1. Each of the eight components is considered separately, and the following simplifying assumptions have been used:

1. All eight components are rigid bodies,

2. The hydraulic actuators and two bucket guide pieces have negligible mass; only the boom, stick and bucket are assumed to have mass,
3. Mass distributions are assumed even throughout the boom, stick, and bucket bodies,
4. The hydraulic actuators supply all applied forces,
5. The hydraulic actuators are subject only to viscous friction, which will be lumped into the actuator hydraulic models, and
6. Pin friction friction is negected.

D.2 Boom, Stick, and Bucket Center of Gravity Locations

Figure D.2 shows the approximated center of gravity locations for the boom, stick, and bucket components of the JD 410G backhoe workgroup. The purpose of this section is to show the mathematical relationships used to determine the magnitude of the twelve β-labeled angles used to locate the center of gravity of each body with respect to the modeling points. The β-labeled angles are determined using the orientation of the workgroup calculated in Appendix B. To calculate the β angles, the law of cosines is used to permit adjustments to the center of gravity location by simply changing the distance between the modeling points and the center of gravity location.

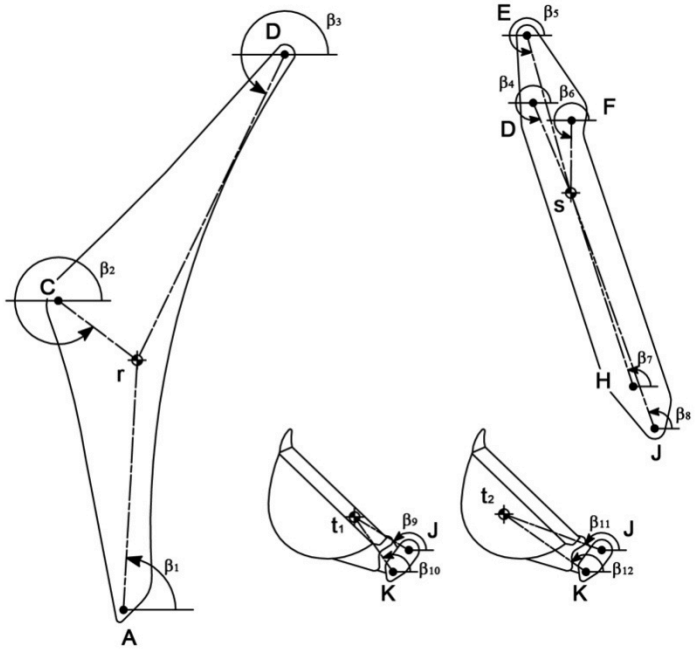

Figure D.2 Estimated Center of Gravity Locations for the Boom, Stick, and Bucket

The following set of equations are used to determine the magnitude of the β-labeled angles in Figure D.2.

$$\beta_1 = \theta_2 - cos^{-1}\left[\frac{{L_{AC}}^2+{L_{Ar}}^2-{L_{Cr}}^2}{2(L_{AC})(L_{Ar})}\right], \quad [D.1]$$

$$\beta_2 = 2\pi + \theta_4 - cos^{-1}\left[\frac{{L_{CD}}^2+{L_{Cr}}^2-{L_{Dr}}^2}{2(L_{CD})(L_{Cr})}\right], \quad [D.2]$$

$$\beta_3 = \pi + \theta_4 + cos^{-1}\left[\frac{{L_{CD}}^2+{L_{Ar}}^2-{L_{Cr}}^2}{2(L_{AC})(L_{Ar})}\right], \quad [D.3]$$

$$\beta_4 = \theta_8 - cos^{-1}\left[\frac{{L_{Ds}}^2+{L_{DF}}^2-{L_{Fs}}^2}{2(L_{Ds})(L_{DF})}\right], \quad [D.4]$$

$$\beta_5 = \theta_7 - cos^{-1}\left[\frac{{L_{Es}}^2+{L_{EF}}^2-{L_{Fs}}^2}{2(L_{Es})(L_{EF})}\right], \quad [D.5]$$

$$\beta_6 = \theta_9 - cos^{-1}\left[\frac{{L_{Fs}}^2+{L_{FH}}^2-{L_{Hs}}^2}{2(L_{Fs})(L_{FH})}\right], \quad [D.6]$$

$$\beta_7 = \theta_{10} - \pi - cos^{-1}\left[\frac{{L_{DH}}^2+{L_{Hs}}^2-{L_{Ds}}^2}{2(L_{Hs})(L_{DH})}\right], \quad [D.7]$$

$$\beta_8 = \theta_{16} - \pi - cos^{-1}\left[\frac{{L_{HJ}}^2+{L_{Js}}^2-{L_{Hs}}^2}{2(L_{HJ})(L_{Js})}\right], \quad [D.8]$$

$$\beta_9 = \theta_{15} - cos^{-1}\left[\frac{{L_{Jt_1}}^2+{L_{JK}}^2-{L_{Kt_1}}^2}{2(L_{Jt_1})(L_{JK})}\right], \quad [D.9]$$

$$\beta_{10} = \theta_{15} - \pi + cos^{-1}\left[\frac{{L_{Kt_1}}^2+{L_{JK}}^2-{L_{Jt_1}}^2}{2(L_{Kt_1})(L_{JK})}\right], \quad [D.10]$$

$$\beta_{11} = \theta_{15} - cos^{-1}\left[\frac{{L_{Jt_2}}^2+{L_{JK}}^2-{L_{Kt_2}}^2}{2(L_{Jt_2})(L_{JK})}\right], \text{ and} \quad [D.11]$$

$$\beta_{12} = \theta_{15} - \pi + cos^{-1}\left[\frac{{L_{Kt_2}}^2+{L_{JK}}^2-{L_{Jt_2}}^2}{2(L_{Kt_2})(L_{JK})}\right]. \quad [D.12]$$

D.3 Kinematic Equations for the Center of Gravity Locations

The kinematic equations that will be presented in the next section require the acceleration of the center of gravity location of the boom, stick, and bucket to be known. This section shows the velocity and acceleration equations for points 'r','s', and 't_1'. The method used is identical to the kinematic relationships presented in Appendix B. All equations will be separated into individual components in the $\hat{\imath}, \hat{\jmath}$, and $\hat{k}$ directions (the kinematic relationships are presented in three dimensions, although the kinetic relationships will only use two dimensions).

D.3.1 Kinematic Equations for the Center of Gravity of the Boom, Point 'r'

The velocity of point 'r' is expressed using

$$\hat{\imath}: \quad V_{rx} = V_{Ax} + L_{Ar}\left(\frac{d\theta_2}{dt}\sin(\beta_1)\sin(\phi) - \frac{d\phi}{dt}\cos(\beta_1)\cos(\phi)\right), \qquad [D.13]$$

$$\hat{\jmath}: \quad V_{ry} = V_{Ay} + L_{Ar}\left(-\frac{d\theta_2}{dt}\sin(\beta_1)\cos(\phi) - \frac{d\phi}{dt}\cos(\beta_1)\sin(\phi)\right), \text{ and} \qquad [D.14]$$

$$\hat{k}: \quad V_{rz} = L_{Ar}\left(\frac{d\theta_2}{dt}\cos(\beta_1)\right). \qquad [D.15]$$

Building on the results from the velocity equations, the acceleration of point 'r' is expressed using

$$\hat{\imath}: \quad A_{rx} =$$

$$A_{Ax} + L_{Ar}\left[\frac{d^2\theta_2}{dt^2}\sin(\beta_1)\sin(\phi) - \frac{d^2\phi}{dt^2}\cos(\beta_1)\cos(\phi) + \left[\left(\frac{d\theta_2}{dt}\right)^2 + \left(\frac{d\phi}{dt}\right)^2\right]\cos(\beta_1)\sin(\phi) + 2\frac{d\theta_2}{dt}\frac{d\phi}{dt}\sin(\beta_1)\cos(\phi)\right], \qquad [D.16]$$

$$\hat{\jmath}: \quad A_{ry} = A_{Ay} + L_{Ar}\left[-\frac{d^2\theta_2}{dt^2}\sin(\beta_1)\cos(\phi) - \frac{d^2\phi}{dt^2}\cos(\beta_1)\sin(\phi) - \left[\left(\frac{d\theta_2}{dt}\right)^2 + \left(\frac{d\phi}{dt}\right)^2\right]\cos(\beta_1)\cos(\phi) + 2\frac{d\theta_2}{dt}\frac{d\phi}{dt}\sin(\beta_1)\sin(\phi)\right], \text{ and} \qquad [D.17]$$

$$\hat{k}: \quad A_{rz} = L_{Ar}\left[\frac{d^2\theta_2}{dt^2}\cos(\beta_1) - \left(\frac{d\theta_2}{dt}\right)^2\sin(\beta_1)\right]. \qquad [D.18]$$

D.3.2 Kinematic Equations for the Center of Gravity of the Stick, Point 's'

The velocity of point 's' is expressed using

$$\hat{\imath}: \quad V_{sx} = V_{Dx} + L_{Ds}\left(\frac{d\theta_6}{dt}\sin(\beta_4)\sin(\phi) - \frac{d\phi}{dt}\cos(\beta_4)\cos(\phi)\right), \qquad [D.19]$$

$$\hat{\jmath}: \quad V_{sy} = V_{Dy} + L_{As}\left(-\frac{d\theta_6}{dt}\sin(\beta_4)\cos(\phi) - \frac{d\phi}{dt}\cos(\beta_4)\sin(\phi)\right), \text{ and} \qquad [D.20]$$

$$\hat{k}: \quad V_{sz} = L_{Ds}\left(\frac{d\theta_6}{dt}\cos(\beta_4)\right). \qquad [D.21]$$

Building on the results from the velocity equations, the acceleration of point 's' is expressed using

$$\hat{\imath}: \quad A_{sx} =$$

$$A_{Dx} + L_{Ds}\left[\frac{d^2\theta_6}{dt^2}\sin(\beta_4)\sin(\phi) - \frac{d^2\phi}{dt^2}\cos(\beta_4)\cos(\phi) + \left[\left(\frac{d\theta_6}{dt}\right)^2 + \left(\frac{d\phi}{dt}\right)^2\right]\cos(\beta_4)\sin(\phi) + 2\frac{d\theta_6}{dt}\frac{d\phi}{dt}\sin(\beta_4)\cos(\phi)\right], \quad [D.22]$$

$$\hat{\jmath}: \quad A_{sy} = A_{Dy} + L_{Ds}\left[-\frac{d^2\theta_6}{dt^2}\sin(\beta_4)\cos(\phi) - \frac{d^2\phi}{dt^2}\cos(\beta_4)\sin(\phi) - \left[\left(\frac{d\theta_6}{dt}\right)^2 + \left(\frac{d\phi}{dt}\right)^2\right]\cos(\beta_4)\cos(\phi) + 2\frac{d\theta_6}{dt}\frac{d\phi}{dt}\sin(\beta_4)\sin(\phi)\right], \text{ and} \quad [D.23]$$

$$\hat{k}: \quad A_{sz} = L_{Ds}\left[\frac{d^2\theta_6}{dt^2}\cos(\beta_4) - \left(\frac{d\theta_6}{dt}\right)^2\sin(\beta_4)\right]. \quad [D.24]$$

D.3.3 Kinematic Equations for the Center of Gravity of the Bucket, Point 't_1'

The velocity of point 't_1' is expressed using

$$\hat{\imath}: \quad V_{t_1x} = V_{Jx} + L_{Jt_1}\left(\frac{d\theta_{15}}{dt}\sin(\beta_9)\sin(\phi) - \frac{d\phi}{dt}\cos(\beta_9)\cos(\phi)\right), \quad [D.25]$$

$$\hat{\jmath}: \quad V_{t_1y} = V_{Jy} + L_{Jt_1}\left(-\frac{d\theta_{15}}{dt}\sin(\beta_9)\cos(\phi) - \frac{d\phi}{dt}\cos(\beta_9)\sin(\phi)\right), \text{ and} \quad [D.26]$$

$$\hat{k}: \quad V_{t_1z} = L_{Jt_1}\left(\frac{d\theta_{15}}{dt}\cos(\beta_9)\right). \quad [D.27]$$

Building on the results from the velocity equations, the acceleration of point 't_1' is expressed using

$$\hat{\imath}: \quad A_{t_1x} = A_{Jx} + L_{Jt_1}\left[\frac{d^2\theta_{15}}{dt^2}\sin(\beta_9)\sin(\phi) - \frac{d^2\phi}{dt^2}\cos(\beta_9)\cos(\phi) + \left[\left(\frac{d\theta_{15}}{dt}\right)^2 + \left(\frac{d\phi}{dt}\right)^2\right]\cos(\beta_9)\sin(\phi) + 2\frac{d\theta_{15}}{dt}\frac{d\phi}{dt}\sin(\beta_9)\cos(\phi)\right], \quad [D.28]$$

$$\hat{\jmath}: \quad A_{t_1y} = A_{Jy} + L_{Jt_1}\left[-\frac{d^2\theta_{15}}{dt^2}\sin(\beta_9)\cos(\phi) - \frac{d^2\phi}{dt^2}\cos(\beta_9)\sin(\phi) - \left[\left(\frac{d\theta_{15}}{dt}\right)^2 + \left(\frac{d\phi}{dt}\right)^2\right]\cos(\beta_9)\cos(\phi) + 2\frac{d\theta_{15}}{dt}\frac{d\phi}{dt}\sin(\beta_9)\sin(\phi)\right], \text{ and} \quad [D.29]$$

$$\hat{k}: \quad A_{t_1z} = L_{Jt_1}\left[\frac{d^2\theta_{15}}{dt^2}\cos(\beta_9) - \left(\frac{d\theta_{15}}{dt}\right)^2\sin(\beta_9)\right]. \quad [D.30]$$

D.4 Free Body Diagrams and Kinetic Equations

For each of the eight components that make up the JD 410G backhoe workgroup, a free body diagram (FBD) showing the location and assumed direction of each force will be presented, followed by the three kinetic relationships for each body. In general, the detailed equations are developed from the two general equations

$$\sum \vec{F} = m\,\overrightarrow{A_G}, \text{ and} \quad [D.31]$$

$$\sum \vec{M}_G = I_G\,\alpha. \quad [D.32]$$

The force Equation D.31 will be presented in its two separate $\hat{\jmath}$ and $\hat{k}$ components, based on the coordinate system and model orientation defined in Appendix B.

D.4.1 Boom FBD and Kinetic Relationships

Figure D.3 shows the FBD developed for the boom cylinder, noting that point 'r' denotes the approximate location of the center of gravity.

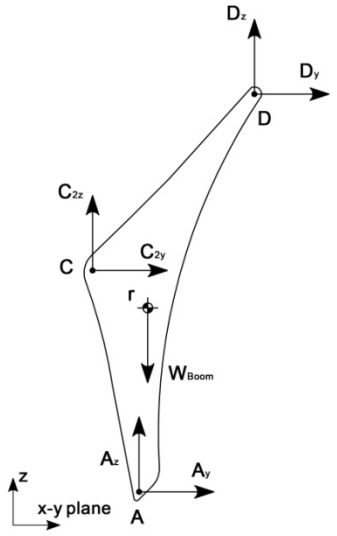

Figure D.3 Boom Free Body Diagram

The three kinetic equations developed from the FBD are

$$\hat{\jmath}: A_y + C_{2y} + D_y = m_{Boom}A_{ry}, \quad [D.33]$$

$$\hat{k}: A_z + C_{2z} + D_z - W_{Boom} = m_{Boom}A_{rz}, \text{ and} \quad [D.34]$$

$$A_y L_{Ar}\left(-\sin\left(\beta_1\right)\right) + A_z L_{Ar}\left(cos(\beta_1)\right) + C_{2y} L_{Cr}\left(-\sin\left(\beta_2\right)\right) + C_{2z} L_{Cr}\left(cos(\beta_2)\right) +$$
$$D_y L_{Dr}\left(-\sin\left(\beta_3\right)\right) + D_z L_{Dr}\left(cos(\beta_3)\right) = I_r \alpha_{Boom}. \quad [D.35]$$

D.4.2 Boom Cylinder FBD and Kinetic Relationships

The FBD developed for the boom cylinder is presented in Figure D.4.

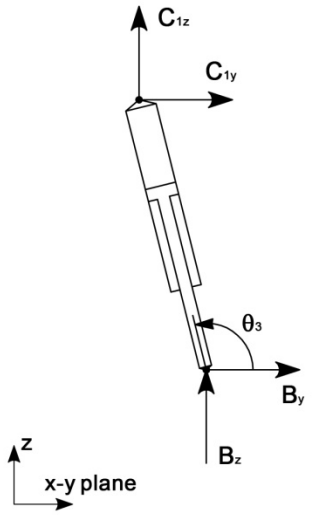

Figure D.4 Boom Cylinder Free Body Diagram

The three kinetic relationships developed from the FBD are

$$\hat{j}: C_{1y} + B_y = 0, \quad [D.36]$$

$$\hat{k}: C_{1z} + B_z = 0, \text{ and} \quad [D.37]$$

$$B_y sin(\theta_3) - B_z cos(\theta_3) - C_{1y} sin(\theta_3) + C_{1z} cos(\theta_3) = 0. \quad [D.38]$$

D.4.3 Stick FBD and Kinetic Relationships

The FBD of the stick is shown in Figure D.5. The approximated center of gravity is located at point ‘s.’

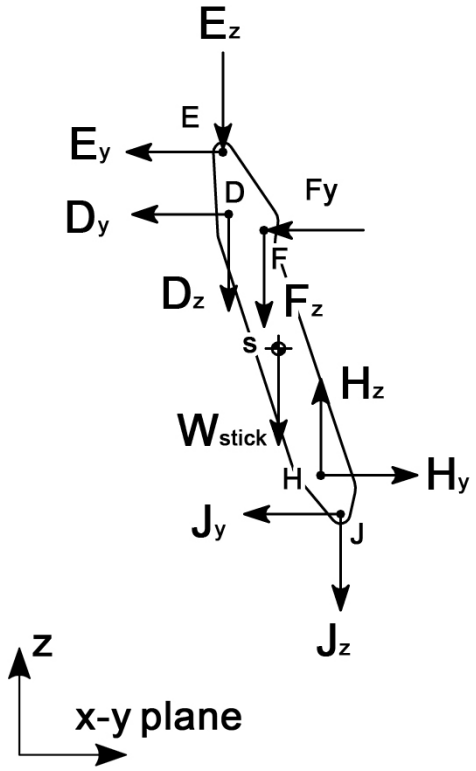

Figure D.5 Stick Free Body Diagram

The three kinetic relationships developed for the stick from the FBD are

$$\hat{j}: -D_y - E_y - F_y + H_y - J_y = m_{Stick}A_{sy}, \quad \text{[D.39]}$$

$$\hat{k}: -D_z - E_z - F_z + H_z - J_z - W_{Stick} = m_{Stick}A_{sz}, \text{ and} \quad \text{[D.40]}$$

$$D_y L_{Ds}\big(\sin(\beta_4)\big) - D_z L_{Ds}\big(cos(\beta_4)\big) + E_y L_{Es}\big(\sin(\beta_5)\big) - E_z L_{Es}\big(cos(\beta_5)\big) + F_y L_{Fs}\big(\sin(\beta_6)\big) - F_z L_{Fs}\big(cos(\beta_6)\big) - H_y L_{Hs}\big(\sin(\beta_7)\big) + H_z L_{Hs}\big(cos(\beta_7)\big) + J_y L_{Js}\big(\sin(\beta_8)\big) - J_z L_{Js}\big(cos(\beta_8)\big) = I_s \alpha_{Stick}. \quad \text{[D.41]}$$

D.4.4 Stick Cylinder FBD and Kinetic Relationships

Figure D.6 shows the FBD of the stick cylinder.

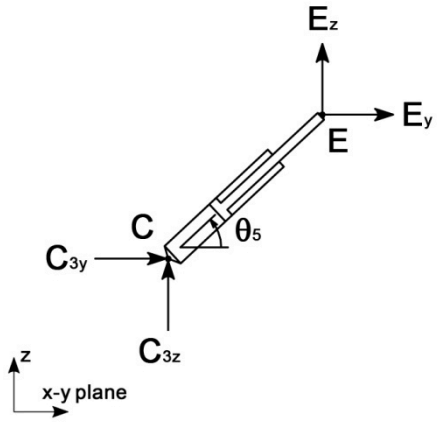

Figure D.6 Stick Cylinder Free Body Diagram

The three kinetic relationships developed for the stick cylinder are

$$\hat{j}: C_{3y} + E_y = 0, \quad \text{[D.42]}$$

$$\hat{k}: C_{3z} + E_z = 0, \text{ and} \quad \text{[D.43]}$$

$$-E_y sin(\theta_5) + E_z cos(\theta_5) + C_{3y} sin(\theta_5) - C_{3z} cos(\theta_5) = 0. \quad \text{[D.44]}$$

D.4.5 Bucket FBD and Kinetic Relationships

Figure D.7 shows the FBD of the bucket. The bucket is modeled as having two separate center of gravity locations. Point 't_1'is the approximated location of the center of gravity of only the bucket itself; point 't_2'is the approximated center of gravity of a fully loaded bucket (although bucket loads will not be considered in this thesis, such that $m_{Load} = 0$).

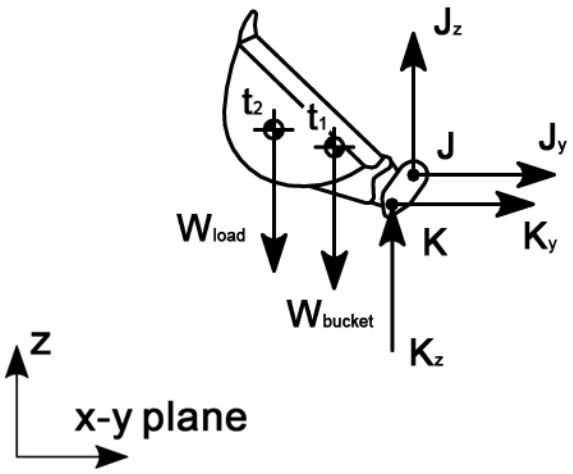

Figure D.7 Bucket Free Body Diagram

The three kinetic relationships for the bucket are

$$\hat{j}: J_y + K_y = m_{Bucket} A_{t_1 y}, \quad \text{[D.45]}$$

$$\hat{k}: J_z + K_z - W_{Bucket} = m_{Bucket} A_{t_1 z}, \text{ and} \quad \text{[D.46]}$$

$$J_y L_{Jt_1}\left(\sin(\beta_9)\right) - J_z L_{Jt_1}\left(cos(\beta_9)\right) + K_y L_{Kt_1}\left(\sin(\beta_{10})\right) - K_z L_{Kt_1}\left(cos(\beta_{10})\right) = I_{t_1}\alpha_{Bucket}. \quad \text{[D.47]}$$

D.4.6 Three-point Bucket Guide FBD and Kinetic Relationships

Figure D.8 shows the FBD of the three-point bucket guide.

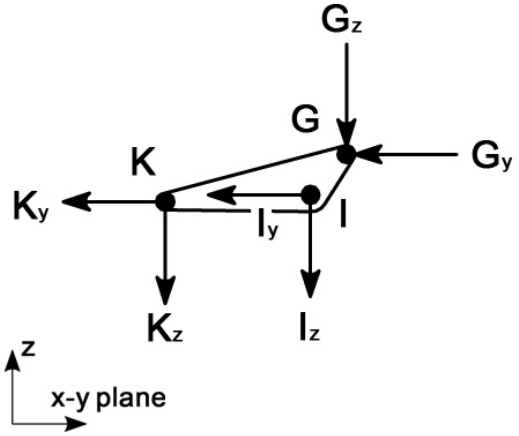

Figure D.8 Three-point Bucket Guide Free Body Diagram

The kinetic relationships for the three-point bucket guide are

$$\hat{j}: -I_y - K_y - G_y = 0, \quad \text{[D.48]}$$

$$\hat{k}: -I_z - K_z - G_z = 0, \text{ and} \quad \text{[D.49]}$$

$$I_y(\sin(\theta_{13})) - I_z\big(cos(\theta_{13})\big) + G_y(\sin(\theta_{13} + \alpha_6)) - G_z\big(cos(\theta_{13} + \alpha_6)\big) = 0. \quad \text{[D.50]}$$

D.4.7 Two-point Bucket Guide FBD and Kinetic Relationships

Figure D.9 shows the two-point bucket guide FBD.

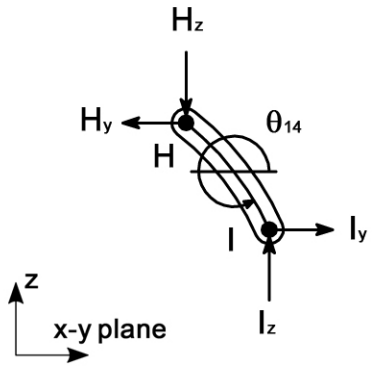

Figure D.9 Two-point Bucket Guide Free Body Diagram

The kinetic relationships for the two-point bucket guide are

$$\hat{j}: -H_y + I_y = 0, \quad \text{[D.51]}$$

$$\hat{k}: -H_z + I_z = 0, \text{ and} \quad \text{[D.52]}$$

$$-H_y(\sin(\theta_{14})) + H_z\big(cos(\theta_{14})\big) - I_y(\sin(\theta_{14})) + H_z\big(cos(\theta_{14})\big) = 0. \quad \text{[D.53]}$$

D.4.8 Bucket Cylinder FBD and Kinetic Relationships

Figure D.10 shows the bucket cylinder FBD.

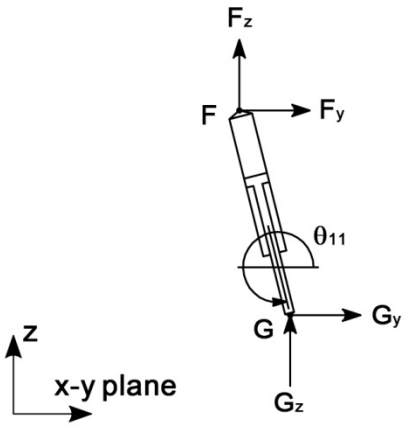

Figure D.10 Bucket Cylinder Free Body Diagram

The kinetic relationships for the bucket cylinder are

$$\hat{j}: F_y + G_y = 0, \quad \text{[D.53]}$$

$$\hat{k}: F_z + G_z = 0, \text{ and} \quad \text{[D.54]}$$

$$-F_y\left(\cos\left(\frac{3\pi}{2} - \theta_{11}\right)\right) + F_z\left(sin\left(\frac{3\pi}{2} - \theta_{11}\right)\right) + G_y\left(\cos\left(\frac{3\pi}{2} - \theta_{11}\right)\right) - G_z\left(sin\left(\frac{3\pi}{2} - \theta_{11}\right)\right) = 0. \quad \text{[D.55]}$$

D.4.9 FBD and Kinetic Relationships at Point C

The modeling point 'C,' shown in Figure D.1 connects the boom, boom cylinder, and stick cylinders to each other by means of a pinned joint. It is the only point on the system that joins three bodies together; special consideration is required to ensure the direction of the forces calculated at 'C' are correct (as all three forces have the same magnitude). Figure D.11 shows a FBD of the pin at point 'C.'

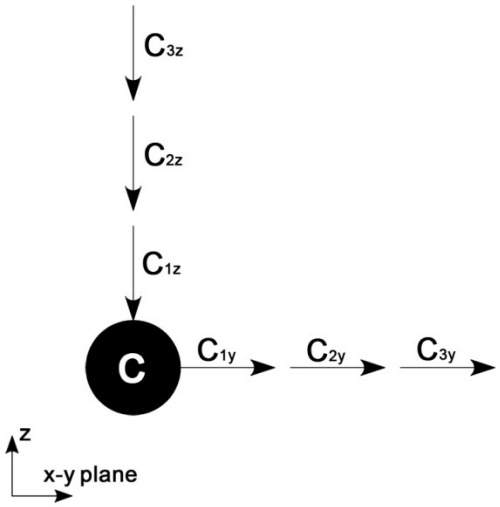

Figure D.11 Free Body Diagram at Point C

For this FBD, only the force equations are considered, as the moment equation does not apply when all forces act through a common point. The equations that relate all of the forces at C are

$\hat{j}$: $C_{1y} + C_{2y} + C_{3y} = 0$, and [D.56]

$\hat{k}$: $C_{1z} + C_{2z} + C_{3z} = 0$. [D.57]

D.5 Kinetic Solution Approach

The kinetic equations presented in the previous section are solved using a matrix inversion method. There are a total of 26 equations and 26 unknowns to be solved.

Appendix E: Instrumentation Calibration

This appendix contains the calibration curves for the instrumentation used in the experimental data collection performed in this thesis. All data were collected using a computer with a National Instruments HI-Speed USB Carrier (model: NI USB-9162, serial: 11D4091) having a National Instruments DAQ (model: NI 9201, serial: 11D97CA) mounted within the carrier.

E.1 Pressure Transducer Calibrations

To calibrate the pressure transducers, a Mansfield and Green Inc. "Twin Seal" dead weight tester (model: 5525, serial: 163-1) was used over the range of expected inputs.

1. Pressure Transducer 1: Schaevitz P723-0025 (serial: 91823, range: 0-5000 psiG)

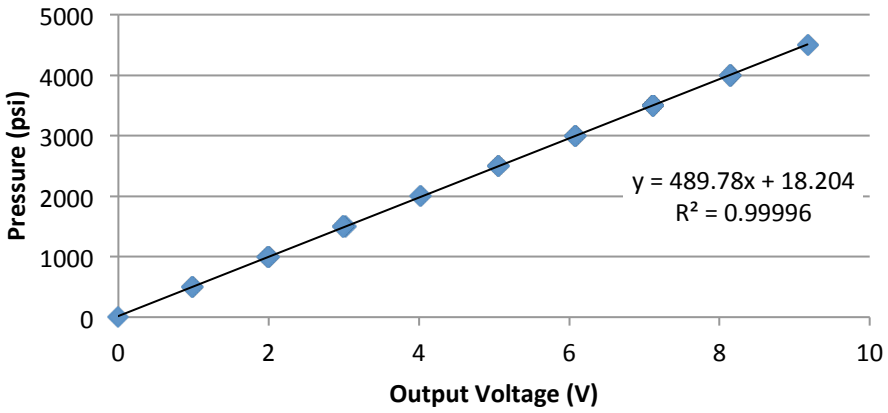

Figure E.1 Calibration Curve for Pressure Transducer 1

2. Pressure Transducer 2: Schaevitz P723-0025 (serial: 92090, range 0-5000 psiG)

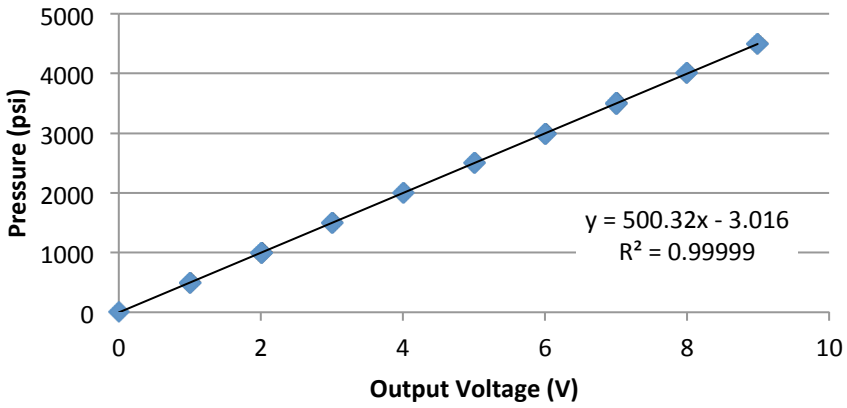

Figure E.2 Calibration Curve for Pressure Transducer 2

3. Pressure Transducer 3: Parker SensoControl Pressure-Temperature Sensor SCPT-400-0-02 (range: 0-600 BAR, measuring pump supply pressure)

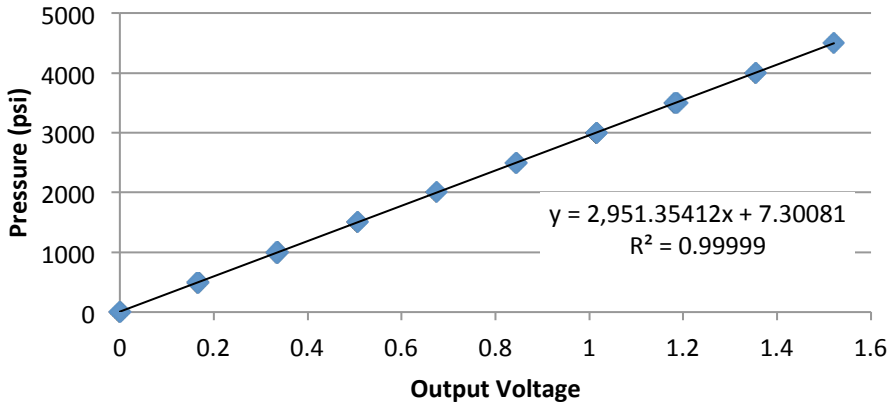

Figure E.3 Calibration Curve for Pressure Transducer 3

4. Pressure Transducer 4: Parker SensoControl Pressure-Temperature Sensor SCPT-040-0-02 (range: 0-60 BAR, measuring return flow pressure)

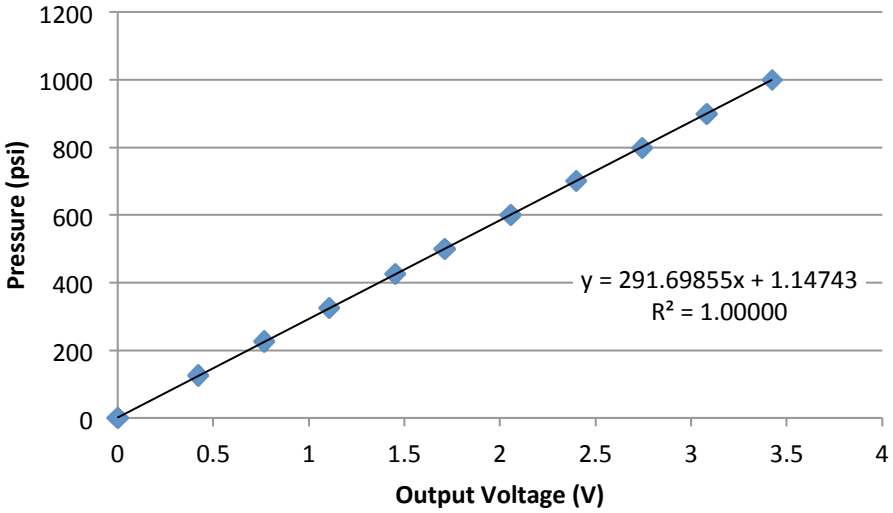

Figure E.4 Calibration Curve for Pressure Transducer 4

Pressure Transducers 1 and 2 were connected to a Measurements Group Strain Gage Amplifier (model: 2160, serial: 70287), and pressure transducers 3 and 4 were connected to a Parker SensoControl Pressure-Temperature-Measuring Amplifier (model: SCM-100-1-01, serial: 2011).

E.2 Linear Potentiometer Calibrations

The linear potentiometers were used to measure the control valve spool displacements, and were calibrated using a Mitutoyo vernier caliper.

1. Linear Potentiometer 1: Litton RVT-K52-3 (serial: 3347)

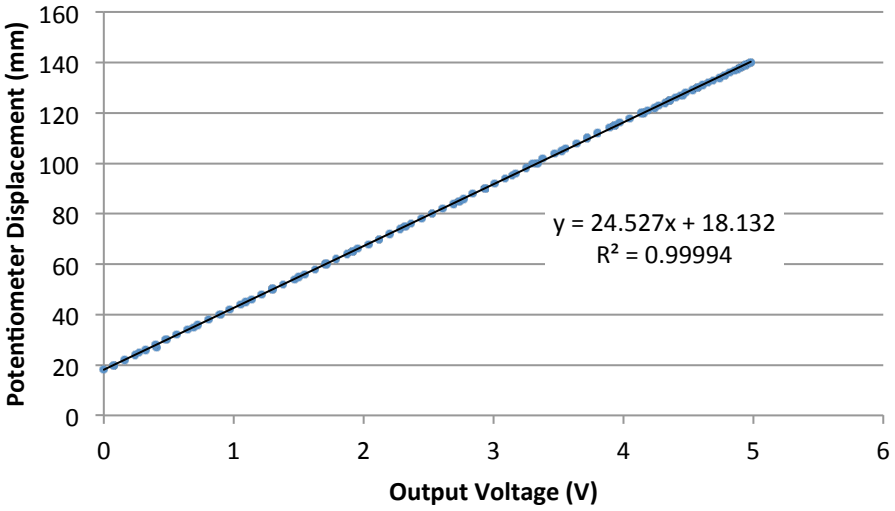

Figure E.5 Calibration Curve for Linear Potentiometer 1

2. Linear Potentiometer 2: Bourns 2001564320 (no serial number provided).

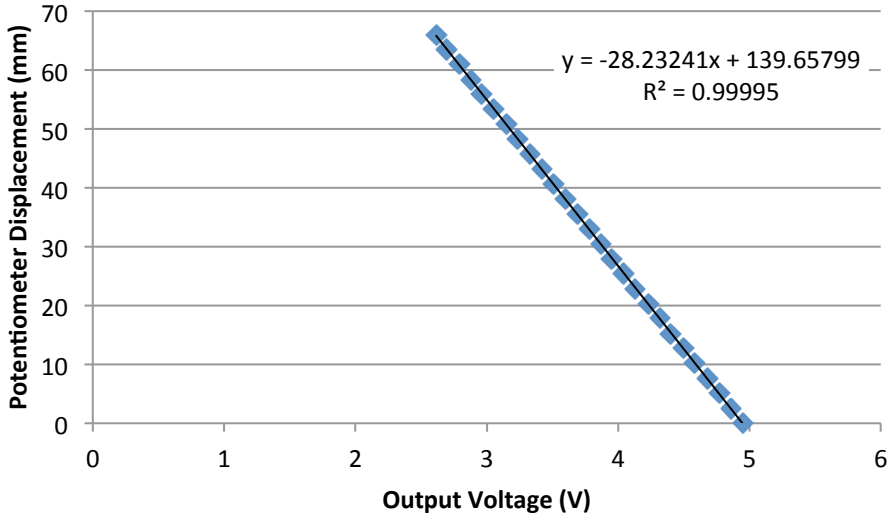

Figure E.6 Calibration Curve for Linear Potentiometer 2

The linear potentiometers were powered by a 5VDC power supply.

E.3 String Potentiometer Calibrations

Four string potentiometers were used to measure the length of various linkages on the backhoe workgroup; calibration was performed using meter sticks.

1. String Potentiometer 1: Celesco (model: PT1DC-40-FR-Z5-C25, serial: F1103558A)

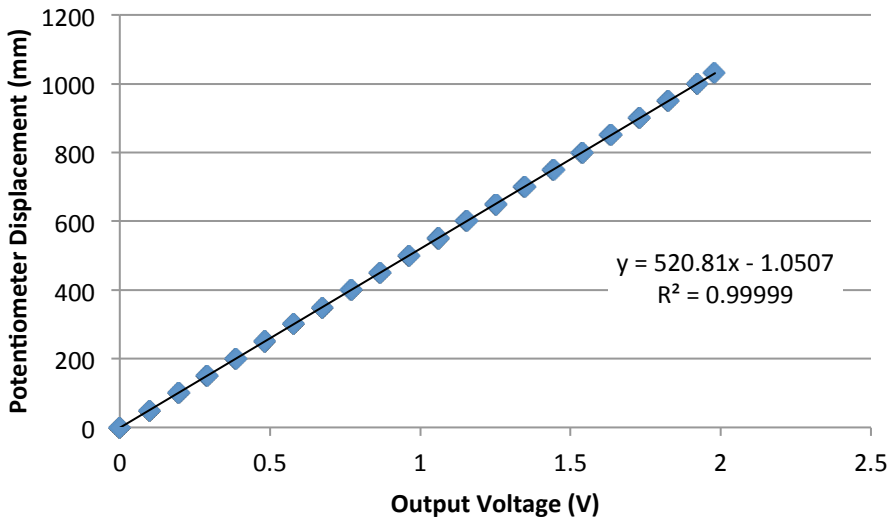

Figure E.7 Calibration Curve for String Potentiometer 1

2. String Potentiometer 2: Celesco (model: PT1DC-40-FR-Z5-C25, serial: F1103559A]

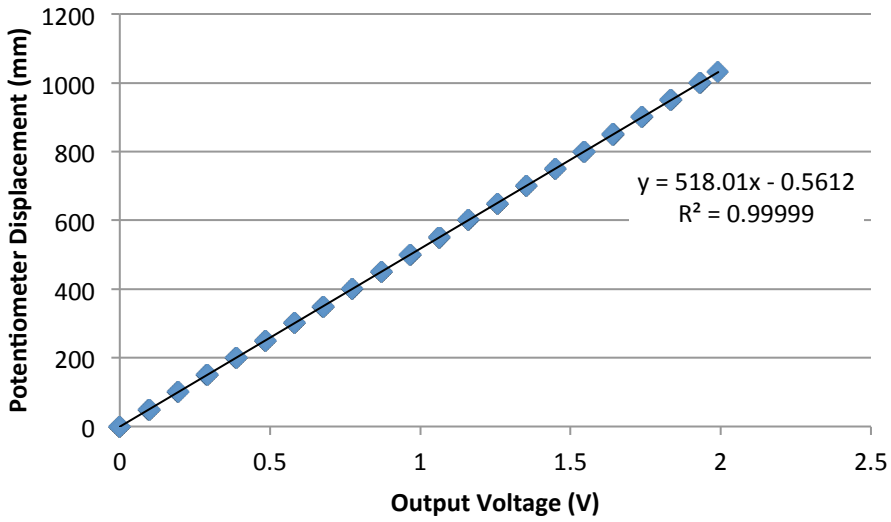

Figure E.8 Calibration Curve for String Potentiometer 2

3. String Potentiometer 3: Celesco (model: 632036 Rev. B, serial: 0805)

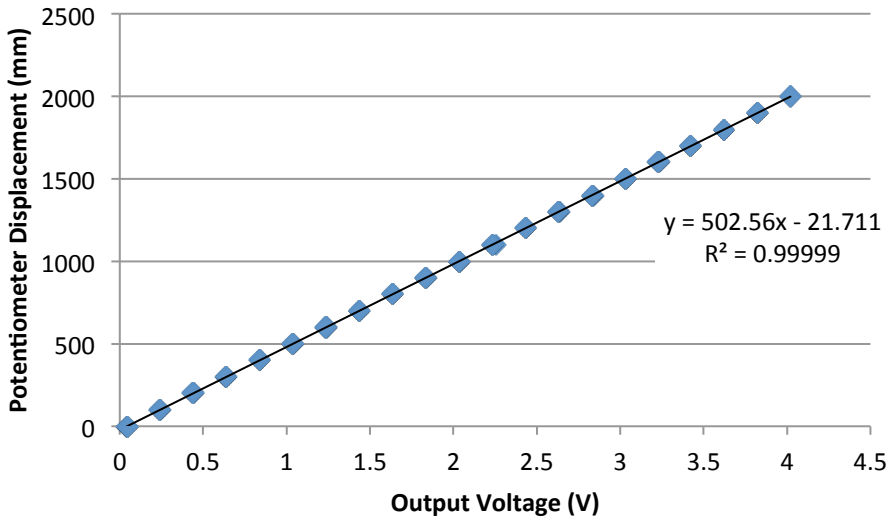

Figure E.9 Calibration Curve for String Potentiometer 3

4. String Potentiometer 4: Celesco (model: 632036 Rev. B, serial: 0805)

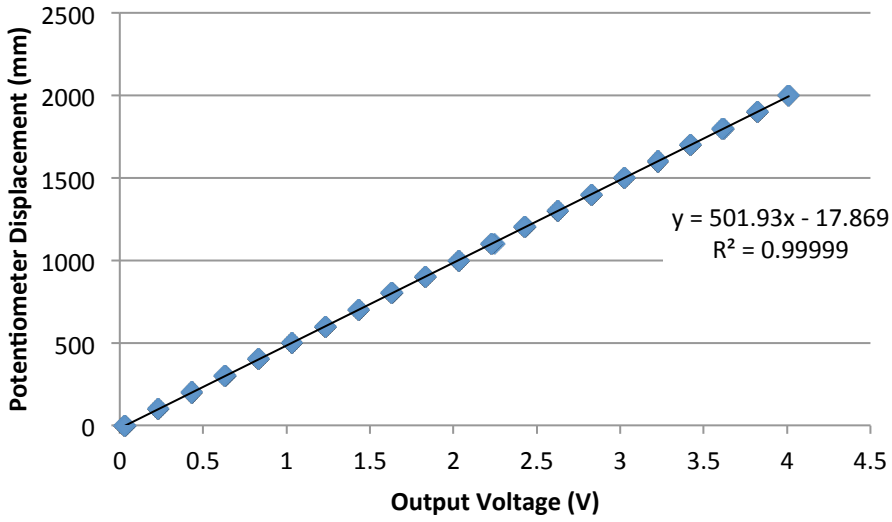

Figure E.10 Calibration Curve for String Potentiometer 4

All four string potentiometers were powered using a 5VDC supply.